TUKUR, FRANK J. Ph.D. Plasmon-Exciton Coupling for Signal Amplification and Biosensing: Fundamentals and Application. (2023)
Directed by Dr. Jianjun Wei. 140 pp.

Surface plasmon resonance (SPR) is the collective oscillation of frequency-matched free-space photons and surface electrons at a metal/dielectric interface. Their inherent sensitivity to refractive index changes and ability to couple with exciton species and enhance light-matter interaction make them ideal candidates for low-concentration analyte detection compared to conventional biosensors. The use of metal nanostructures and nanomaterials to excite SPR represents the current state-of-the-art. However, the challenges associated with repeatable synthesis of uniform nanomaterials, complex nanostructure fabrication, low SPR generation efficiency and limited understanding of the mechanism of plasmon-exciton coupling for signal amplification have motivated the search for alternative architectures and procedures. The uniform and repeatable gold nanoslit (NS) and nanoledge (NL) array architectures offers a promising route towards addressing the above issues, and hence this research attempts to take advantage of these platforms to achieve efficient SPR generation and exciton coupling for biosensing applications.

The overarching scope of this dissertation extends to the design, fabrication, and optimization of metal NS and NL structures for SPR generation and sensing applications. Emphasis is placed on investigating the mechanism of optical signal enhancement arising from plasmon-exciton coupling (PEC) with particular focus on (a) exploring the role of geometry and size of the nanostructures (b) examining the influence of SPR spectral mode overlap with exciton's absorption and/or emission energies on the overall optical signal in a NS or NL system, and (c) investigating the analytical sensitivity and signal transduction of the PEC system to biomolecular interactions.

The nanoimprinting technique based on soft lithography for NS fabrication, which is used in this work for NS array fabrication, required addressing a critical issue, namely PDMS diffusion into nanoscale patterns for high aspect ratio realization. This was mitigated by curing temperature variation and incubation time to achieve 50 nm-130 nm width NS arrays with an intense, broad spectral response that red-shifts and diminishes with increasing NS width. The 50 nm width structure exhibited ~57× optical enhancement when coupled with acridine orange, a

fluorescence dye, whose absorption and emission spectra closely overlaps with plasmonic spectra. A sensitive assay for detecting DNA hybridization was generated using the interaction of the selected SARS-CoV-2 ssDNA and dsDNA with AO to trigger the metachromatic behaviour of the dye to produce a strong optical signal amplification on the formation of AO-ssDNA complex and a quenched signal upon hybridization to the complementary target DNA along with a blue shift in the fluorescence of AO-dsDNA. The SARS-CoV-2 DNA hybridization assay, based on the PEC exhibited 0.21 nM sensitivity to complementary strand target, distinguished 1-, 2-, and 3-base mismatched DNA targets, reusability of ~6 x with 96% signal recovery, stable for up to 10 days at room temperature. Regarding the NL sensing platform, the principle of the sensing mechanism is based on plasmon-mediated extraordinary optical transmission (EOT) whose wavelength red-shifts with increase in refractive index (RI) at near-metal surface. The NL plasmonic-based biosensor fabricated using a patented E-beam writing method exhibited ~ 384.08 nm/RIU sensitivity, limit of detection to cardiac troponin I (TnI) at 0.079 ng/mL, 0.084 ng/mL and 0.097 ng/mL in PBS buffer, human serum, and human blood, respectively. The direct measurement of TnI in whole human blood without any purification or sample preparation step highlights the significance of the sensing platform for point-of-care detection.

Thus, this work innovates (a) a tunable SPR to meet the requirement for plasmon-exciton spectral overlap for optical signal amplification, (b) the mechanism of optical enhancements due to PEC in NS arrays, and (c) a new application of PEC in NS and EOT in NL for the sensitive detection of SARS-CoV-2 DNA hybridization and cardiovascular biomarker TnI in human blood, respectively. The enhanced light-matter interactions have a broader impact beyond healthcare to light harvesting for solar cells, heat generation for cancer therapy, and photocatalysis for nanoscale reactions like water splitting.

PLASMON-EXCITON COUPLING FOR SIGNAL AMPLIFICATION AND BIOSENSING: FUNDAMENTALS AND APPLICATION

by

Frank James Tukur

A Dissertation
Submitted to
the Faculty of The Graduate School at
The University of North Carolina at Greensboro
in Partial Fulfillment
of the Requirements for the Degree
Doctor of Philosophy

Greensboro

2023

Approved by

Dr. Jianjun Wei
Committee Chair

DEDICATION

I dedicate this dissertation to God Almighty who saw me through my study journey and to Whom my future is owed.

APPROVAL PAGE

This dissertation written by Frank James Tukur has been approved by the following committee of the Faculty of The Graduate School at The University of North Carolina at Greensboro.

Committee Chair	JianjunWei
Committee Members	Tetyana Ignatova
	Eric Josephs
	Dennis LaJeunesse

March 14, 2023
Date of Acceptance by Committee

March 14, 2023
Date of Final Oral Examination

ACKNOWLEDGEMENTS

Thanks to my parents for my resilience and trust in God, Dr. Emmanuel Ogbole, and the Keku’s for their moral advise, the International American Fellowship (IAF) and the Piedmont International Fellowship (PIF) for friendship and creating a home away from home, Dr. Bhawna Bagra and Dr. Taylor Mabe for my early exposure to thin film technology, Dr. Jianjun Wei for his mentorship and guidance, Evelyn Newberger for being my biggest supporter, and the Joint School of Nanoscience & Nanoengineering for giving me the training and access to numerous state-of-the-arts laboratory tools.

TABLE OF CONTENTS

LIST OF TABLES

LIST OF FIGURES

CHAPTER I: INTRODUCTION

The very nature of human existence continues to suffer numerous threats arising from bioterrorism, food toxicity, environmental pollution, and diseases. According to the Center for Disease and Control (CDC), cardiovascular disease kills one person every 37 seconds in the United States. The World Health Organization (WHO) reported ten million deaths due to cancer in 2020 alone, which is more than the entire population of Austria. Cancer mortality is projected to increase by 64% (~16.3 million) by 2040. In Africa and certain parts of Asia, there were 241 million reported cases of malaria in 2020, with 627,000 deaths, mostly women and children. The recent COVID-19 epidemic has claimed over 6.8 million lives as of February 23, 2023. Early detection of these deadly diseases is vital to the survival of their victims. Current hospital diagnostic tools have been very useful but are more effective when patients show symptoms. This is of concern because, with cases like cancer, any delay in detection makes it difficult to arrest and manage the situation resulting in untimely death. There is therefore a need for an alternative diagnostic device that possess the accuracy, sensitivity, speed, and portability for early disease diagnosis. Surface plasmon resonance (SPR)-based biosensors could be the answer to these concerns. The recent proliferation of diseases such as COVID-19 and its variants continue to push the demand for biosensors whose current global market share now stands at $29.13 billion (about $90 per person in the US) and is projected to reach $49.6 billion by 2030 (Figure 1.1).[1,2,3] The use of plasmonic nanomaterials and structures in developing home-based point-of-care devices for early disease detection represent the current state-of-the-arts in biosensor development.

Figure 1.1. Biosensor Market Size from 2021 to 2030 (USD billion)

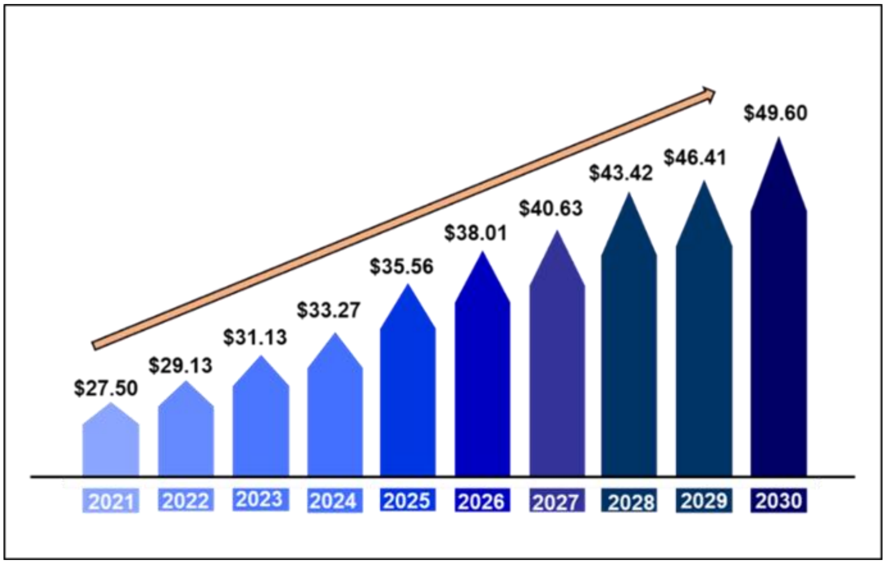

The central theme of my research is in the design, fabrication, and study of portable biosensors. My key focus within this broad area is in micro-and nanofabrication, plasmon-exciton coupling (introduced below) for optical signal amplification, and bio-detection. I present a background introduction below and at the close of this chapter I give a brief introduction of the subsequent chapters contained in this dissertation.

Surface Plasmon Resonance

Metals are generally composed of sea of mobile electrons that can be triggered into collective oscillation by an incident electromagnetic waves.[4] In other words, the coupling between photons and free electrons on a metallic surface such as gold, silver, or heavily dopped semiconductors generates an amplified field mode known as surface plasmon resonance (SPR). When these metals are chiseled down to nanometer scale, they behave as light scattering antennas. The employment of this property in structured metallic surfaces to generate nanoscale photonic circuitry has given birth to the field of plasmonics, which has unveiled a broad spectrum of opportunities for new basic research and technological evolution. Studies in this area has broadened the scope of understanding of the interaction of light with metals alongside numerous realized and potential applications.[5,6] Measurement technologies like near-field optical microscopy and plasmon-enhanced biosensors are made possible by the ability of metallic nanostructures to trap and concentrate electromagnetic waves.

The high-density electron fluid in metals, as described by the Drude's model, is composed of stationary positive ions and a gas of non-interacting electrons in motion. This electronic motion is slowed by a viscous friction due to collision with the ions or lattice. Hence, the plasma moves with a frequency given by the relation:[7]

$$\omega_p = (4\pi e^2 n_e / m^*)^{\frac{1}{2}} \qquad (1)$$

where n_e is the mean density of electrons, related to the Fermi energy of the material, e is the electric charge, and m is the mass of the electron, which depends on the band structure of the material. The plasma frequency (typically resides in the UV region) is a key parameter in dictating metals optical characteristics like SPR excitation. The relationship between the dielectric constant (ε) of the metal, the plasma (ω_p) frequency, and the frequency of the incident light (ω) is essential in providing information on the momentum-matching condition needed for an incident light to excite surface electrons. From the relation in equation (2),[8]

$$\varepsilon = 1 - \frac{\omega_p^2}{\omega^2} \qquad (2)$$

if $\omega < \omega_p$, the incident light is reflected by the metal surface without exciting surface plasmons (SPs). For $\omega > \omega_p$, the electrons cannot follow the oscillation frequency of the incident light. As a result, light can penetrate the metal without exciting SPs. To excite plasma electrons at the metal/dielectric interface, the frequency of incident light must match the frequency of the surface electrons, that is, if $\omega=\omega_p$, the incident photons can couple with the collective oscillation of electronic charge density at the metal/dielectric interface leading to a SPR.

The classification of SPs into localized surface plasmon resonance (LSPR) and surface plasmon polariton (SPP) is depicted in Figure 1.2. LSPR is a resonant mode that is spatially confined at the surface such as of a noble metal sphere of size less than the wavelength of incident light.

Figure 1.2. SPP and LSPR Excited on the Two Types of Nanostructures

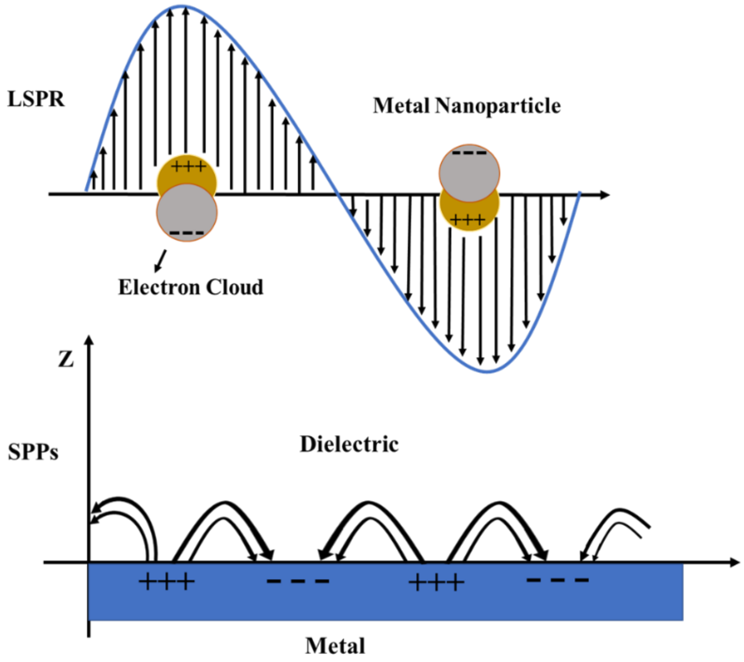

On the other hand, SPP is a form of longitudinal waves that propagate along an extended metal/dielectric interface in a one dimensional metal structure.[9] the term polariton is used to describe a hybrid state that display the properties of both light and matter.[10] Important feature of SPP include the evanescence field which propagates perpendicular to the surface with a propagation length of intensity that decays exponentially with the distance from the surface. The damping of the electric field intensity is caused by the interaction of surface charges with electromagnetic field which results in ohmic losses of the electrons participating in the SPP. The propagation length is governed by the geometry and dielectric function of the metal nanostructures and the wavelength of incident photon. The wavelength shift of the evanescent field in transmission or reflection peak, caused by small changes in the refractive index near the metal surface emphasize the relevance of SPP mode for biosensing application.

Another important feature of SPP is the dispersion relation. It expresses the relationship between the wave vector (k_x) and angular frequency (ω). For light in a vacuum, the k_x and ω are related linerarly. As shown in Figure 1.3, the SPs has a higher frequency than free space radiation. The SP frequency is given by $\omega_p = \frac{\omega}{\sqrt{1+\varepsilon_m}}$, where ε_m is the dielectric constant of the metal. In vacuum, the SPP frequency reduces to $\omega_p = \frac{\omega}{\sqrt{2}}$

The dispersion of electromagnetic surface mode for a short pitched metal gratings of various depths is described by:[11]

$$k_{SPP} = \frac{\omega}{c}\left(\frac{\varepsilon_1\,\varepsilon_2}{\varepsilon_1 + \varepsilon_2}\right)^{1/2}$$

where k_{SPP} is the wave vector of the SPP and k_o is the wave vector of the incident radiation, ε_1 and ε_2 are the frequency-dependent permittivity of the metal and dielectric. k, ω, c, express the wave number, angular frequency, and speed of light, respectively. The green line in Figure 3 describes the SPP dispersion curve on a flat surface. It starts at the light line (red) and immediately curves away as k_x is increased to approach ω_p. Because the curve is beyond the light line in the ω-k space, it is prevented from direct coupling with the incident radiation. Therefore, it is impossible to excite plasmons on a flat metal surface with a plane light wave.[12] A phase matching condition between the wave vector of the incoming light with the wave vector of the surface plasmon must be realized before SPR can be excited.

Figure 1.3. Graphical Representation of the Dispersion Relation of SPP

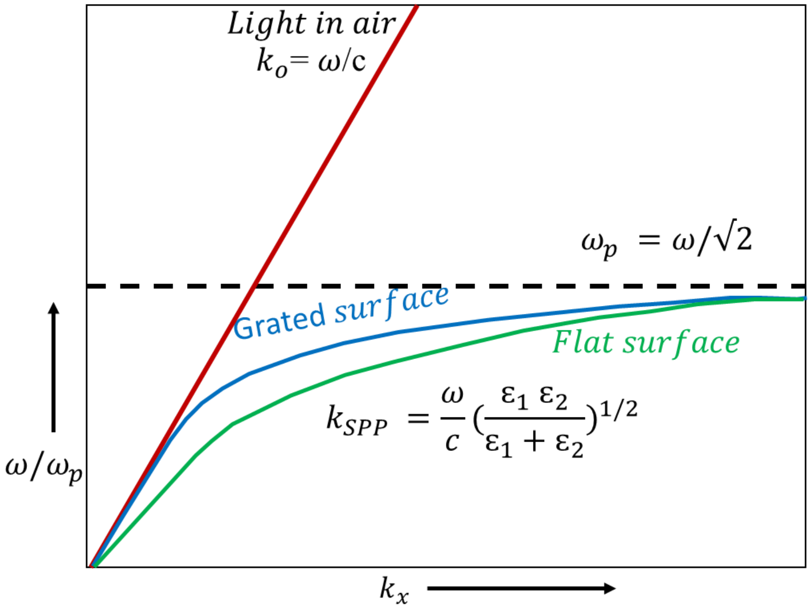

Excitation of Surface Plasmon Resonance

Common surface plasmon excitation modes include prism coupling,[13] waveguide coupling,[14] strong-focused beams,[15] near-field excitation,[16] and grating coupling.[17,18] Prism coupling could take the form of either the Kretschmann or Otto configurations. They both require a prism to achieved phase matching and SPR excitation on a smooth surface. The two configurations differ in the orientation of the prism relative to the metal film. As shown in Figure 1.4, the arrangement in Kretschmann configuration leaves no air gap between the prism and the metal surface. The evanescence field generated can directly penetrate up to 45 nm thick metal to excite SP. In contrast, the otto configuration leaves a dielectric gap between the prism and the metallic surface. The evanescence field can penetrate this gap if the angle of incident light (θ) is greater than the critical angle. These configurations enjoy the benefit of temperature independence which adds to their application merit. However, the need to precisely control the gap between the prism and metal surface makes it more complex and hence less favourable than the Kretschmann configuration. Because the excited SP in both configurations is sensitive to refractive index changes at the metal surface, they are widely employed for biosensing applications.

Figure 1.4. Methods of SPP Excitation with Photons. (A) Kretschmann Configuration, (B) Otto Configuration, (C) Grating Configuration

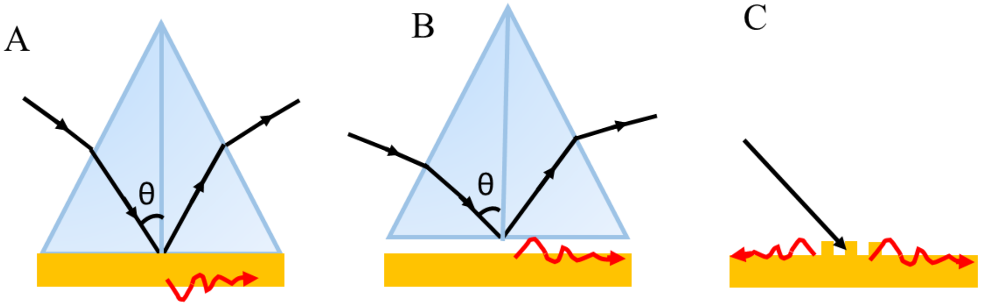

Notably, the use of prism places a size limitation on the application of these configurations for the development of modern miniaturized plasmonic devices. Attention is now focused on metal films that are structured with grooves (Figure 1.4C).[8] Due to their ability to couple external light without the need for a complex optical configuration, they are small, they provide easy geometrical modulation of optical response across the visible, near- and far-IR ranges. Most importantly, they can be designed to excite both SPP and LSPR in a single system. Grating coupling is achieved when the periodic groove structure on a metal surface causes the band of the Brillouin-zone boundary that is set to fold.[11] As a result, the SPP dispersion (blue curve) (Figure 1.3) is brought into a ω-k space where it intersects with the grating incident light.[19] What makes SPR interesting is the generation of propagating evanescent field and the localization of electromagnetic field both of which promote phenomena like extraordinary optical transmission and plasmon Fano resonances. These properties open doors to a better understanding of light-matter interaction for numerous applications in biosensing, photonic circuitry and quantum computing.[16] The main drawback of grating plasmonic system is the relatively weak resonance intensity and low spectral contrast, which limit signal-noise-ratio and thus detection resolution.

Although the enhancement of electric field in plasmonic structures is key to developing advanced and efficient devices, the realization is challenging.[20,21,22] Several attempt to dictate and enhance the magnitude of electromagnetic field in plasmonic systems include the use of both theorical and experimental approaches to investigate the impact of physical factors like size, morphology, composition, and geometric arrangement of the metallic nanostructure**.**[5,23] For example, the Mie theory is used to describe the optical properties of nanoparticles (NPs) with dimensions smaller than the wavelength of the incident light.[24] Extension of this theory to spheroidal particle case is implemented by the Gan's theory.[23] For NPs of various dimension, the optical properties, such as absorption, scattering and extinction are best calculated using the discrete-dipole approximation method.[25,26] Although the numerical finite difference time-domain (FDTD) simulation provides optical information about the electromagnetic (EM) field distribution around NPs, it is the most widely adopted tool used to design and simulate how physical parameters like size and shape affects the generation, propagation or localization of fields as well as the intensity and frequency of those fields in both simple and complex nanostructures. The FDTD is a time domain technique that solves Maxwells equations such that a single simulation can provide plasmonic modes for SPR over a wide range of frequencies and wavelengths. This is advantageous when faced with a nanostructure having numerous variables like slit width, metal film thickness, period, and material composition. The real-time movie and images of EM field distribution that it provides gives a fundamental understanding of the SPR mode generated. These information saves time and resources by providing useful insights to which device to fabricate or further investigate. These are the reasons why FDTD is chosen as the simulation tool in this research.

It is noteworthy that only few natural materials support surface plasmons excitation. These include noble metals like Au, Ag, and Al.[27,28,29] Other materials like graphene, transition metal oxides, and highly dopped semiconductors have shown promise but are difficult to engineer.[4] The scarcity of plasmon materials is exacerbated by the requirement for a material to have low optical losses at the optical bandwidth, a negative real part of the dielectric function and a small imaginary part. However, gold was utilized in this work over silver and other metals due to its desirable optical properties, stability to corrosion and resistance to chemical attack.

Plasmon-Exciton Coupling

Much like surface plasmons, the exciton state is created when a molecule absorbs light energy sufficient to form an electron-hole pair bound state. The exciton state can collapse via radiative or nonradiative electron-hole recombination or through non-radiative dissociation where the electron is connected to a circuit to generate current. The efficiency of radiative recombination or current generation relies on how efficient an incident light interacts with an emitter (exciton material).

Molecular excitons interaction with direct plane light is not efficient due to the size mismatch between the light wavelength and the exciton material. This leads to a poor energy conversion due to diffraction limit. Thankfully, metallic nanostructures can interact with incident light and break the diffraction limit to form a concentrated local field in a nanoscale volume.[30,31] Plasmon-exciton coupling (PEC) is a process that enhances nanoscale light-matter interactions.[9] As shown in Figure 1.5, it involves the use of subwavelength light confinement properties of metal nanostructures like NPs and nanocavities to excite excitons in materials like fluorescent dyes, quantum dots (QDs) carbon nanotubes, and carbon nanodots. Therefore, an exciton material placed in the vicinity of the concentrated plasmon fields can efficiently interact with the fields to give an enhanced optical behaviour.

Figure 1.5. Plasmon-Exciton Coupling for Enhanced Exciton Recombination or Dissociation

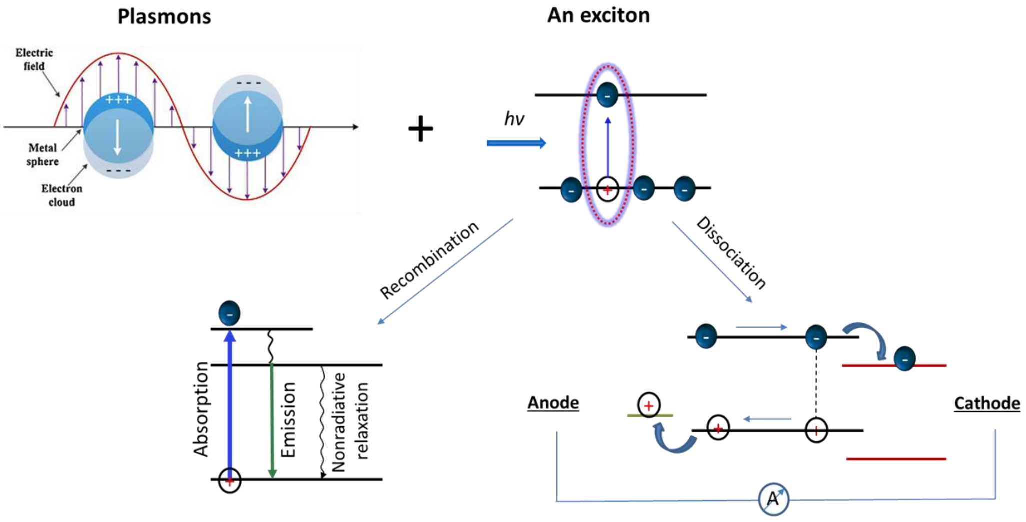

Although plasmon and excitons are both excited by light, they differ in their optical properties.[32] For example, plasmon couples strongly with external field but suffers from relatively large dissipation that leads to a broadened resonant peak. Excitons, on the other hand, couples weakly with external field and exhibit longer lifetime that causes it to have weak and sharp resonant peak.[33,34,35] However, the mutual coupling of plasmon with exciton provides a new optical property that is superior to what can be achieved using either of its component; an enhanced and tuneable near-field intensity.

PEC offers control of light at the nanoscale at an ultrafast timescale that is not achievable by the present photonic or electronic technologies.[36] This presents PEC systems as an ideal playground to search and explore exotic optical properties for novel applications such as in optical biosensors, light emitting diodes, transistors and photovoltaic cells.[33,32] It is noteworthy that PEC interaction occur in two regimes:[37,38] strong and weak coupling regimes.

Strong Plasmon-Exciton Coupling

In 1982, the first experimental demonstration of plasmon-exciton interaction in the strong coupling regime where radiative decay rates are affected, and new energy levels are formed was reported.[30] The use of Langmuir– Blodgett monolayer assemblies on a silver surface by Hertzdog led to a widespread interest in examining strong PEC using inorganic semiconductors as emitters. It was not until 1997 that Agronivich and co-workers pioneered the study of organic emitters in plasmonic systems. It was then discovered that large transition dipole moment of organic molecules provides them the ability to exhibit larger coupling strength compared to inorganic emitters. [39] Ever since, there has been an aggressive interest to investigate light-matter interaction using an array of different emitters.

To create a strong coupled system, the optical metal structure and quantum emitter must be engineered to be in resonance.[40] Whenever the frequency of an excited plasmon oscillation matches with the frequency of an emitter placed in close distance, their states hybridize to form two new levels of upper and lower energy than the initial ones. This happens due to the reversible exchange of energy between the emitter and the nanostructure plasmonic modes.[41] The split-hybridized state is called Rabi-splitting and in many cases serves as an indicator for strong coupling. An earlier study by Glass and co-workers on the luminescence of dye molecules adsorbed on Ag, Au and Cu nanoparticles revealed that strong coupling is accompanied by huge modification of the plasma resonance spectra of the metals.[40] This finding was validated when the adsorbed emitting molecules have absorption band that is in the same frequency range with plasmon frequency.

Weak Plasmon-Exciton Coupling

Weak plasmon-exciton coupling is commonly characterized by fluorescence enhancement or enhanced energy absorption observed when an emitter is in close proximity to a metal with excited SPR.[42] This phenomenon is called Purcel effect.[43,33] The Purcell effect refers to the spontaneous emission rate modification of quantum emitters coupled to an optical antenna due to the increase of the local density of states in the vicinity of the antenna.[44,45] Generalized interpretation of this effect suggest that the fluorescence intensity of an emitter depends on both its intrinsic properties and the material environment it is located.[36] By extension, florescence intensity can be modulated by altering the environments local electromagnetic density of states.

Current Approach to Plasmon-Exciton Coupling

Plasmon-exciton interaction can either enhance or suppress emitters fluorescence emission intensity.[46] A recent study involving gold nanorod and quantum dots (QDs) system reported 10.8 times fluorescence enhancement at a 2.5 QDs/rod concentration interacting at 5 nm apart.[37] The fluorescence enhancement occurred only at the hot spots (highly localized electromagnetic field) located at the edge of the rod. Conversely, they demonstrated that QDs located on the surface of the rod experienced fluorescence quenching. Their proposed mechanism suggests that Plasmon-induced local field can enhance fluorescence via manipulation of the excitation rate and the quantum yield of the emitter in the weak coupling regime.

Another recent study captured the effect of local field enhancement on plasmon–exciton coupling in Au bowtie dimer and square array nanoantennae coupled with WS_2 monolayer. The electric field distribution measurement indicated that the square array structure relatively has multiple “hot spots” which contributes to the overall field distribution leading to a strong fluorescence enhancement of WS_2 than the bowtie design.[47] The findings emphasize on the role of SPR generation on photoluminescence (PL) enhancement of nearby emitters. The proposed mechanism of optical enhancement in the plasmonic environment advocates that the extent of PEC depended on the degree of overlap of the emitter’s absorption spectrum with the metal’s surface plasmon. The more significant the extent of overlap, the greater the PL intensity enhancement of the emitting specie. Other parameters that impact the PL intensity include the emission, and energy dissipation rates in the metal-emitter complex. These parameters are influenced by the geometry and the physical and material properties of the metallic structure.[48] The effect of variable EM field on the fluorescence emission of a dye was thoroughly investigated.[5] The authors tuned the localized plasmonic field in the gap region of adjacent metallic nanoparticles by changing the particle size and the separation distance. Their focus was to see how the fluorescence intensity of Cyanine-5 placed in the gap region would respond to different magnitude of gap EM field. They found that adjacent NPs at 8.2 nm separation distance produced the optimum enhancement in local field in the gap region and which gave rise to the strongest fluorescence enhancement. Furthermore, the fluorescence intensity which had been initially pre-quenched by attaching the dye to a single Au NPs was turned-on in the plasmonic gap region with 5-fold fluorescence enhancement compared to unquenched free Cys-5 molecules. The enhanced fluorescence emission in the gap region between the two NPs is attributed to the coupling of the fluorophores with localized surface plasmons.[49] The PL quenching observed with a single NP is attributed to the transfer of electrons from the emitter into the metal's empty orbital.[50] Smaller than optimal gap distance resulted in poor SPR excitation due to generation of hot electrons that causes phonon vibration and loss of optical energy as heat. Therefore, placing an emitter in a plasmonic gap does not guarantee PL enhancement. Optimization of the gap distance is a necessary step in designing an efficient PEC system.

In a similar demonstration of fluorescence enhancement, a new type of core-shell quantum dots (QDs) in direct contact with Ag NPs was utilized.[43] In contrast to other literatures that reported that the direct contact of an emitter with a single NP would lead to photoluminescence quenching, it was rather demonstrated here that at the resonant plasmon-exciton coupling of the nanostructure, fluorescence emission is enhanced. This unique observation was attributed to the design and composition of the hybrid (core-shell) QDs which prohibit electron transfer from the QDs into the NPs empty orbital.

A pioneering work describes the excitation of excitons in QDs via a direct transfer of energy from SPP to the QDs resulting in increased emission intensity.[32] Conversely, the authors also noticed that when the frequency of excitons matches with that of the plasmons, the excited exciton decays non-radiatively. The quenching is attributed to an energy transfer from the excitons to the metal surface to induce surface plasmon generation. This undermines other findings that reported PL enhancement under similar plasmon-exciton frequency matching condition.[36] However, the bidirectional relationship (plasmons exciting excitons and vice vera) can be used to modulate the optical properties of the entire system. The modification could either mean quenching or enhancement of PL depending on the details of the configuration. The proposed mechanism of the bidirectional interaction of SPP in metallic structure with the excitons involves the launching of SPPs in the metallic structure by light, coupling of SPs with nearby emitters leading to exciton excitation via direct energy inducement, and the decay of excited excitons either radiatively or non-radiatively.

In summary, plasmon-exciton coupling effects especially in the weak coupling regime depends on the magnitude of EM-field. It also depends on whether a fluorophore is directly attached to either a single nanoparticle, planar metallic surface or placed in a cavity.[51] Although the absorption efficiency of emitters is enhanced by the near-field in planer metallic nanostructure, PL quenching occurs.[52] This mean that absorption enhancement does not necessarily translate to PL enhancement. Hence, the mechanism of optical enhancement in a PEC system remains unclear.

To minimize quenching effect, several approaches that utilizes nanoparticle dimers,[43] nanorods,[38] nanoholes,[53] nanoslits,[54] and bowtie dimers[55] have been explored. The PL enhancement when an emitter is sandwiched between two or more metal structures is due to the strong local field generated by a plasmon-plasmon coupling between adjacent metal structures.[35] Many studies have been conducted but there are enormous plasmonic nanostructure designs and emitters for which the PEC effects have not yet been fully investigated.[56,47]

Plasmonic Nanostructure Design

A major limitation of plasmonic resonators is their tendency to strong radiative damping and ohmic losses in metal which limits the SPP propagation length.[36] Proper design and optimization of the nanostructure geometry is therefore needed to reduce or prevent ohmic loses. To minimize optical loss and efficiently harness the power of SPR and LSPR in a single system, this dissertation examines two forms of designs (Figure 1.6) using simulation and experimental measurements.

The first is the nanoslit array design. Enhanced SPR mode is expected in the system due to the thin film of gold introduced at the bottom of the slit. The rational is that the extra metal/dielectric interface created at the bottom of the slit will trigger SPR which can only be excited on a continuous metal film. The point where two metal surfaces meet (top and bottom edges of the nanoslit) could behave like a NP and excite LSPR. The near-field generated within this design is expected to be sensitive to near-surface changes in refractive index, with little to no sensitivity to bulk RI changes. Relative to NPs plasmonic designs, the geometry of the nanoslit allows convenient placement and accommodation of optically active materials and creates avenues towards its widescale adoption in flow-through devices for biomolecular sensing applications.[57] The focused ion-beam (FIB) is a common technique employed to create nanostructures on thin metallic films.[57] However, this direct-writing technique is disadvantaged due to its poor scalability, time-consuming production and thus high cost. Approaches based on soft lithography offers a more scalable and time-saving fabrication methodology. Therefore, a simple nanoimprinting technique was employed in this research to make the nanoslit arrays.

The second is the nanoledge array design. It is more like a nanoslit within another nanoslit. This two-step nanoslit system is hypothesized to show sensitivity to small changes in RI changes in bulk mediums and near-surface binding events due SPP-mediated extraordinary optical transmission (EOT) through the NL gap. EOT describes the enhanced transmission of some visible and NIR light through a subwavelength aperture by orders of magnitude larger than expected from standard aperture theory.[58] According to Bethe's theory the diffraction limit of light should not allow light to pass through an orifice smaller than its wavelength. It was difficult to prove the theory in the early days due to fabrication challenges.[58,59] But years later, it was found that light can tunnel through a sub-wavelength apertures due to surface plasmons formed on each metal/dielectric interfaces.[19] The spectral characteristics of the EOT depends on the effective refractive index (n_{eff}) at the metal/dielectric interface, the hight (h), width (W) and periodicity of the NL and the resonance wavelength (λ) at the phase matching condition. The wavelength of optical transmission through the NL aperture can be approximated by the equation:[60]

$$\lambda_{SPR} = \frac{nP}{\sqrt{1 + n_{eff}^2 / \varepsilon_m}} \qquad (3)$$

Since the size, shape and geometry of the metal aperture determines the efficiency of SPP excitation, EOT is found to be dependent on the metal's geometry. The wavelength sensitivity of EOT transmission to changes in RI informed our decision to use the NL EOT-based system for biosensing application. A patented fabrication method using electron beam was used to make the NL structures. This method was chosen for its precision and capability to produce high aspect-ratio patterns.

Figure 1.6. Gold nanoslit on PDMS Substrate and Gold Nanoledge on Glass Substrate

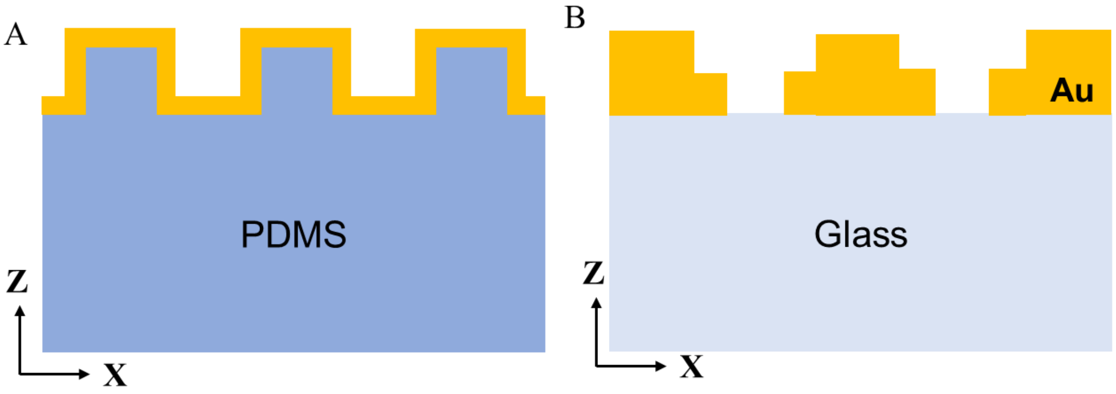

Goal Statement

The goal of this research is to advance our understanding of plasmon-exciton interaction in Au nanocavities and facilitate the development of a new biosensor technology. The overarching scope extends to the design, fabrication, and optimization of metal nanoslit and nanoledge structures for efficient SPP generation and optical signal enhancement. The hypothesis is that the geometry of the nanostructures will have an impact on SPP generation efficiency. Emphasis is placed in understanding the mechanism of communication between surface plasmon resonance and molecular emitters. The SPP spectral mode overlap with exciton's absorption and/or emission energies is expected to dictate the overall optical signal (reflectance or transmittance) in the PEC system.

Innovation

The main novelties of this research are:

1) The newly developed plasmonic nanoslit array structure fabricated with an in-slit Au base, for enhanced SPP generation.
2) The formulated mechanism of optical enhancements due to PEC.
3) The application of the PEC for the sensitive detection of SARS-Cov-2 DNA hybridization and the utilization of a NL array for Troponin I detection.

Broader Impact

Heat Generation. Plasmon-exciton enhanced photon absorption is known to excite hot electrons leading to the generation of heat because of electron phonon interaction. The generated heat can be utilized in cancer therapy and steam generation.[61]

Photocatalysis. The basic fact remains that chemical reactions can be influenced by factors such as pressure, pH and temperature. The thermal energy accumulated by plasmonic materials upon irradiation can be harnessed to accelerate the rate of chemical reactions.[62] This has direct implication in photo-catalyzing nanoscale reactions such as water splitting and purification and CO_2 reduction.

Solar Cells. The electromagnetic field generation due to plasmon-exciton coupling could be used to enhance the efficiency of photovoltaic cells by increasing the light harvesting efficiency and tunability of absorption spectra.[34]

Summary of Chapters

Chapter II gives an extensive literature review on trending PEC systems with focus on the mechanism of signal amplification for biosensing application. Research gaps were identified, and an outlook was proposed. Chapter III examined the SPR at a flexible (PDMS/Au) thin film substrate with nanoslit array of different widths, specifically 50 nm, 70 nm, 90 nm, 110 nm and 130 nm using both numerical simulation and experimental measurements. Firstly, the nanoslit structure was created on a silicon wafer using an electron beam lithography or the focused ion beam and was used as a template for multiple time. First, PDMS was cured on the silicon template to transfer a negative imprint of the nanoslit array onto the PDMS. This was followed by a physical deposition of Au whose thickness was used to vary the widths of the nanoslit. Experimental optical reflection data, FDTD simulation and semi-analytical modelling data were compared based on peak wavelength value corresponding to the nanoslit width. The mechanism of optical signal enhancement due to plasmon-exciton coupling with acridine orange, propidium iodide, and dihydroethidium dyes was investigated. To investigate the performance of the device for biosensing, SARS-Cov-2 DNA hybridization was determined based on reflectance peak intensity fluctuation in response to increasing concentration of complementary DNA target. Finally, the stability and reusability of the plasmonic biosensing device was investigated.

Chapter IV features the use of an Au nanoledge substrate design where the extraordinary optical transmission through the nanoledge array was used as the transduction signal to detect low concentration of cardiac troponin I spiked in buffer, human serum, and human blood mediums. The change in wavelength position of the transmitted optical signal was used to investigate surface binding events. Firstly, sensitivity of the device to changes in refractive index was examined. Then, the surface of the nanoledge is functionalized with a self-assembled monolayer (SAM) of cystamin/glutaraldehyde to enable the capture of troponin I aptamer. The detection performance of the transmitted SPR sensor to bound troponin I was investigated. The monolayer thickness at different concentrations of troponin was compared with the transmittance peak position. The selectivity of the sensor probe was tested in the presence of interferents like myoglobin, creatin kinase and heparin. The reproducibility of the sensor was also investigated. Chapter V gives a conclusive summery of the scientific findings of this research. Future work-interest relating to the scientific gaps that are beyond the scope of this work is also presented.

REFERENCES

1. Hou, S. *et al.* Manipulating Coherent Light-Matter Interaction : Continuous Transition between Strong Coupling and Weak Coupling in MoS2 Monolayer Coupled with Plasmonic Nanocavities To cite this version : HAL Id : hal-03091461. (2022).
2. Gutiérrez, Y., Brown, A. S., Moreno, F. & Losurdo, M. Plasmonics beyond noble metals: Exploiting phase and compositional changes for manipulating plasmonic performance. *J. Appl. Phys.* **128**, (2020).
3. Nugroho, F. A. A. *et al.* Topographically Flat Nanoplasmonic Sensor Chips for Biosensing and Materials Science. *ACS Sensors* **2**, 119–127 (2017).
4. Cao, E., Lin, W., Sun, M., Liang, W. & Song, Y. Exciton-plasmon coupling interactions: From principle to applications. *Nanophotonics* **7**, 145–167 (2018).
5. Zhu, Z. *et al.* Plasmon-Enhanced Fluorescence in Coupled Nanostructures and Applications in DNA Detection. *ACS Appl. Bio Mater.* **1**, 118–124 (2018).
6. Grasseschi, D., Lima, F. S., Nakamura, M. & Toma, H. E. Hyperspectral dark-field microscopy of gold nanodisks. *Micron* **69**, 15–20 (2015).
7. Shim, H., Kuang, Z. & Miller, O. D. Optical materials for maximal nanophotonic response [Invited]. *Opt. Mater. Express* **10**, 1561 (2020).
8. Ropers, C. *et al.* Grating-coupling of surface plasmons onto metallic tips: A nanoconfined light source. *Nano Lett.* **7**, 2784–2788 (2007).
9. He, Z. *et al.* Principle and Applications of the Coupling of Surface Plasmons and Excitons. *Appl. Sci.* **10**, (2020).
10. Sukharev, M. Topical Review : optics of exciton-plasmon nanomaterials. (2018).
11. Hooper, I. R. & Sambles, J. R. Dispersion of surface plasmon polaritons on short-pitch metal gratings. **65**, 1–9 (2002).
12. Gonçalves, M. R., Minassian, H. & Melikyan, A. Plasmonic resonators : fundamental properties and applications. *J. Phys.* **53**, (2020).
13. Singh, L. *et al.* LSPR based uric acid sensor using graphene oxide and gold nanoparticles functionalized tapered fiber. *Opt. Fiber Technol.* **53**, 102043 (2019).
14. Crego, A. *et al.* Modeling of Nonlinear Propagation in Multi-layer Biological Tissues for Strong Focused Ultrasound. *Chinese Phys. Lett.* **26**, (2009).
15. Bakker, R. M. *et al.* Near-field excitation of nanoantenna resonance. **15**, 13682–13688 (2007).
16. Zeng, B., Gao, Y. & Bartoli, F. Ultrathin plasmonic nanogratings for rapid and highly-sensitive detection. 1–11.
17. E. KRETSCHMANN and H . RAETHER. Radiative Decay of Non Radiative Surface Plasmons Excited by Light. *Z. Für Nat.* **23**, 2135–2136 (1968).
18. Physik, S. & Mfinchen, D. U. Excitation of Nonradiative Surface Plasma Waves in Silver by the Method of Frustrated Total Reflection. *Zeitschrift fur Phys.* **410**, 398–410 (1968).
19. Martín-Moreno, L. *et al.* Theory of extraordinary optical transmission through subwavelength hole arrays. *Phys. Rev. Lett.* **86**, 1114–1117 (2001).
20. Chan, H. B. *et al.* Transmission enhancement in an array of subwavelength slits in aluminum due to surface plasmon resonances. *Bell Syst. Tech. J.* **10**, 143–150 (2005).
21. Liu, C., Hu, F., Yang, W., Xu, J. & Chen, Y. A critical review of advances in surface plasmon resonance imaging sensitivity. *TrAC - Trends Anal. Chem.* **97**, 354–362 (2017).

22. Lee, K. L., Chang, C. C., You, M. L., Pan, M. Y. & Wei, P. K. Enhancing the Surface Sensitivity of Metallic Nanostructures Using Oblique-Angle-Induced Fano Resonances. *Sci. Rep.* **6**, (2016).
23. Ko, H. Particle − Film Plasmons on Periodic Silver Film over Nanosphere (AgFON): A Hybrid Plasmonic Nanoarchitecture for Surface- Enhanced Raman Spectroscopy. (2016) doi:10.1021/acsami.5b09753.
24. Kreibig, U. Interface-induced dephasing of Mie plasmon polaritons. *Appl. Phys. B Lasers Opt.* **93**, 79–89 (2008).
25. Suarasan, S., Tira, C., Rusu, M. M., Craciun, A. M. & Focsan, M. Controlled fluorescence manipulation by core-shell multilayer of spherical gold nanoparticles: Theoretical and experimental evaluation. *J. Mol. Struct.* **1244**, 130950 (2021).
26. Kumar, S., Doi, Y., Namura, K. & Suzuki, M. Plasmonic Nanoslit Arrays Fabricated by Serial Bideposition: Optical and Surface-Enhanced Raman Scattering Study. *ACS Appl. Bio Mater.* **3**, 3226–3235 (2020).
27. Liang, Z., Sun, J., Jiang, Y., Jiang, L. & Chen, X. Plasmonic Enhanced Optoelectronic Devices. *Plasmonics* **9**, 859–866 (2014).
28. Rothe, M. *et al.* Self-Assembly of Plasmonic Nanoantenna-Waveguide Structures for Subdiffractional Chiral Sensing. *ACS Nano* **15**, 351–361 (2021).
29. Mahdavi, F. & Blair, S. Nanoaperture fluorescence enhancement in the ultraviolet. *Plasmonics* **5**, 169–174 (2010).
30. Hertzog, M., Wang, M., Mony, J. & Börjesson, K. Strong light-matter interactions: A new direction within chemistry. *Chem. Soc. Rev.* **48**, 937–961 (2019).
31. Chorsi, H. T., Zhu, Y. & Zhang, J. X. J. Decorative Plasmonic Surfaces. (2017).
32. Li, X., Zhou, L., Hao, Z. & Wang, Q. Q. Plasmon–Exciton Coupling in Complex Systems. *Adv. Opt. Mater.* **6**, 1–21 (2018).
33. Tobing, L. Y. M. *et al.* Plasmon-exciton systems with high quantum yield using deterministic aluminium nanostructures with rotational symmetries. *Nanoscale* **11**, 20315–20323 (2019).
34. Yu, H., Peng, Y., Yang, Y. & Li, Z. Y. Plasmon-enhanced light–matter interactions and applications. *npj Comput. Mater.* **5**, 1–14 (2019).
35. Halas, N. J., Lal, S., Chang, W.-S., Link, S. & Nordlander, P. Plasmons in Strongly Coupled Metallic Nanostructures. *Chem. Rev.* **111**, 3913–3961 (2011).
36. Vasa, P. Exciton-surface plasmon polariton interactions. *Adv. Phys.* **5**, (2020).
37. Trotsiuk, L. *et al.* Plasmon-enhanced fl uorescence in gold nanorod-quantum dot coupled systems. *Nanotechnology* **31**, 105–201 (2020).
38. Trotsiuk, L. *et al.* Plasmon-enhanced fluorescence in gold nanorod-quantum dot coupled systems. *Nanotechnology* **31**, (2020).
39. Chaudhari, K. & Pradeep, T. Spatiotemporal mapping of three dimensional rotational dynamics of single ultrasmall gold nanorods. *Sci. Rep.* **4**, 27–29 (2014).
40. Yankovich, A. B. *et al.* Visualizing Spatial Variations of Plasmon-Exciton Polaritons at the Nanoscale Using Electron Microscopy. *Nano Lett.* **19**, 8171–8181 (2019).
41. Savasta, S. *et al.* Nanopolaritons: Vacuum rabi splitting with a single quantum dot in the center of a dimer nanoantenna. *ACS Nano* **4**, 6369–6376 (2010).
42. Okamoto, K., Funato, M., Kawakami, Y. & Tamada, K. High-efficiency light emission by means of exciton–surface-plasmon coupling. *J. Photochem. Photobiol. C Photochem. Rev.*

32, 58–77 (2017).
43. Toropov, N. A. *et al.* Direct enhancement of luminescence of CdxZn1−xSeyS1−y/ZnS nanocrystals with gradient chemical composition by plasmonic nanoantennas. *Opt. Laser Technol.* **121**, 105821 (2020).
44. Krasnok, A. E. *et al.* An antenna model for the Purcell effect. *Sci. Rep.* **5**, 1–16 (2015).
45. Morozov, K. M. *et al.* Revising of the Purcell effect in periodic metal-dielectric structures: the role of absorption. *Sci. Rep.* **9**, 1–9 (2019).
46. Vance, S. A. & Sandros, M. G. Zeptomole detection of C-reactive protein in serum by a nanoparticle amplified surface plasmon resonance imaging aptasensor. *Sci. Rep.* **4**, 1–7 (2014).
47. Liu, L. *et al.* Strong Plasmon–Exciton Interactions on Nanoantenna Array–Monolayer WS2 Hybrid System. *Adv. Opt. Mater.* **8**, 1–8 (2020).
48. Glass, A. M., Liao, P. F., Bergman, J. G. & Olson, D. H. Interaction of metal particles with adsorbed dye molecules: absorption and luminescence. *Opt. Lett.* **5**, 368 (1980).
49. Li, J. F., Li, C. Y. & Aroca, R. F. Plasmon-enhanced fluorescence spectroscopy. *Chem. Soc. Rev.* **46**, 3962–3979 (2017).
50. Mourdikoudis, S. & Pallares, R. M. Characterization techniques for nanoparticles : comparison and complementarity upon studying. 12871–12934 (2018) doi:10.1039/c8nr02278j.
51. Chen, K. *et al.* High-Q, low-mode-volume and multiresonant plasmonic nanoslit cavities fabricated by helium ion milling. *Nanoscale* **10**, 17148–17155 (2018).
52. Miao, H., Wang, L., Zhuo, Y., Zhou, Z. & Yang, X. Label-free fluorimetric detection of CEA using carbon dots derived from tomato juice. *Biosens. Bioelectron.* (2016) doi:10.1016/j.bios.2016.06.043.
53. Dovzhenko, D. S., Ryabchuk, S. V., Rakovich, Y. P. & Nabiev, I. R. Light-matter interaction in the strong coupling regime: Configurations, conditions, and applications. *Nanoscale* **10**, 3589–3605 (2018).
54. Jadidi, M. M. *et al.* Tunable Terahertz Hybrid Metal-Graphene Plasmons. *Nano Lett.* **15**, 7099–7104 (2015).
55. Pelton, M., Storm, S. D. & Leng, H. Strong coupling of emitters to single plasmonic nanoparticles: Exciton-induced transparency and Rabi splitting. *Nanoscale* **11**, 14540–14552 (2019).
56. Govorov, A. O. *et al.* Exciton-plasmon interaction and hybrid excitons in semiconductor-metal nanoparticle assemblies. *Nano Lett.* **6**, 984–994 (2006).
57. Fontaine, N., Picard-Lafond, A., Asselin, J. & Boudreau, D. Thinking outside the shell: Novel sensors designed from plasmon-enhanced fluorescent concentric nanoparticles. *Analyst* **145**, 5965–5980 (2020).
58. Bethe, H. A. Theory of Diffraction by Small Holes. *Phys. Rev.* **66**, (1944).
59. Degiron, A. *et al.* Diffraction Regimes of Single Holes. *Phys. Rev. Lett.* **023901**, 1–5 (2012).
60. Wei, J., Waldeck, D. H., Kofke, M. & Singhal, S. JSM Nanotechnology & Nanomedicine A Study of Localized Surface Plasmon Resonance Nanoslit Array and Applications for Chip-based Protein Detection. *JSM Nanotechnol Nanomed* **2**, 1–8 (2014).
61. Brongersma, M. L., Halas, N. J. & Nordlander, P. Plasmon-induced hot carrier science and technology. *Nat. Nanotechnol.* **10**, 25–34 (2015).

62. Baffou, G. & Quidant, R. Thermo-plasmonics: Using metallic nanostructures as nano-sources of heat. *Laser Photonics Rev.* **7**, 171–187 (2013).

CHAPTER II: LITERATURE REVIEW

Introduction

There is no other time in the history of mankind that the world is hit as hard by both natural and man-made disasters like bioterrorism, food poisoning, air pollution, and epidemics such as the recent COVID-19 pandemic. The first step to preventive and curative measures begins with early detection. Most often, a specialized device capable of sensing minute concentrations of harmful chemical or biological substances are used.[1] These devices are known as chemical- or biosensors. They convert chemical/biological interactions into a readable signal (optical, electrical, thermal, magnetic) that changes in direct proportion to the concentration of analyte in a sample.[2,3,4] Depending on the type of signal transductions mechanism, they can be classified as electrochemical, optical, thermometric, piezoelectric or magnetic. Modern biosensors are versatile, and compatible some of which include disposable paper based biosensing devices,[5] printable biochips,[6] wearable biosensors,[7] implantable biosensors, [8] ingestible biosensors,[9] and artificial intelligence assisted biosensors.[10]

Electrochemical sensors are low-cost, offer real-time analysis and require low power to operate. According "market research future report", 71% of the 27.5-billion-dollar revenue generated from the biosensor market in 2021 came from electrochemical sensors. With the wide adoption and success of electrochemical sensors, the focus has been slowly shifting towards low-cost multiplexed devices, which is the next step in achieving the desired individualized healthcare.[11,12,13] Electrochemical sensors lack the desirable property to achieve a simultaneous analysis of more than three analytes without signal overlap.[14]

On the other hand, modern optical sensors can perform high-quality measurements comparable to electrochemical sensors commonly used in regulated medical instruments.[15] They offer better options for multiple analysis owing to their ability to integrate optical tags like surface plasmon resonance (SPR). By integrating with microfluidic channels, multiple parameters can be monitored at low cost. They offer quick sample preparation thus saving time. Functionalities like electrical control and signal readout can be condensed on a single microchip, offering an ideal system for POC application.[16] Other advantages of optical sensors includes high sensitivity, remote sensing, isolation from electromagnetic interference, real-time, and kinetic analysis of target analytes.[10] These key characteristics promote their application for the detection of biological and chemical substances and have position them as the fastest growing biosensor segment expected to dominate the 49.6 billion biosensor market share projection by 2030. However, the path to realizing this projection is met with challenges that needs to be addressed. These include poor signal-to-noise ratio, short linear detection range, long response time, and high limit of detection.[17,18]

Classes of Optical Sensors

There are four classes of optical sensors, depending on whether they employ light emission or light-matter interaction; fluorescence-based biosensors which employs fluorescent light emission from target analyte,[19] Surface enhanced Raman scattering (SERS)-based biosensors which are based on optical diffraction due to light-device structure interactions, [20] grating and photonic biosensors,[21] and plasmon-based biosensors which employs optical resonance within an optical cavity.[22,23] The choice of any of these depends on the intended application. For example, fluorescence-based biosensors have been used to detect and manage diseases and for imaging.[24,17] SERS-based sensors have been implemented for environmental monitoring and remediation.[25] Plasmon-based, grating, and photonic biosensors have been used to detect and manage diseases and for wellness applications.[26,27] For diagnostic purposes, fluorescence-based biosensors and plasmon-based biosensors are widely used. The major drawbacks of fluorescence-based biosensors are photobleaching of fluorescent material and poor interaction between the excitation light and the molecular emitter due to diffraction limitations.[28,29] The resulting low optical signal limit the application of fluorescence-based biosensors for low concentration analysis and single molecule detection.

Unlike fluorescence-based biosensors, plasmon-based biosensors which are label free have a very stable but low optical signal.[30] They are further limited by complex fabrication or synthesis of metal nanostructures. The dependence of optical signal on many physical parameters like size, morphology and nature of material makes their optimization challenging.[31] Although plasmon-based biosensors offer relatively better resolution signal and sensitivity, they still require further improvement.

Overview of Plasmon-Based Biosensors

These are analytical devices that integrate a biorecognition element with and optical transducer.[2] The use of plasmonic materials leads to improved special resolution and low time response by enhancing surface-to-volume ratio which allows for down to a single molecule detection with high sensitivity.[39]

Plasmon-based device technologies demonstrated potential to complement conventional electronics and photonics. Semiconductors exhibit electrical properties that position their miniaturization as nanoscale elements for computation and information storage. Dielectrics on the other hand foster information travel over long distances and at a fast data rate. The limitation of semiconductor electronics is interconnect delay-time issues which limits processing speed, whereas dielectric photonics suffers from size limitation due to the fundamental laws of diffraction.[40] Plasmonics emerge as the link to bridge the size advantage of nanoelecronics with the speed advantage of dielectric photonics and provide synergy between the two technologies by interfacing with similar-speed photonic devices and with similar-size electronic components. In the last few decades, the concept of plasmons found applications in the development of high performance near-field optical microscopy and biosensing technologies.[41] More recent advances utilize plasmonics in thermally assisted magnetic recording, thermal cancer treatment, catalysis, and computer chips.[42]

Modern clinical biosensors are gradually shifting from off-site lab tests to near the patient on-site diagnosis. The shift is facilitated by the advancement in nanotechnology that allows for the integration of nanomaterials or structures with electrical devices. The implication is the development of a biosensor that is cheap, smaller in size, easy-to-use, and rapid in diagnosis.[23,43] These attributes make it fit for on-site diagnosis and point-of-care testing (POCT) like the ones already available for glucose and pregnancy testing. To achieve a POCT device, various components (such as light source, transducer, detector, and reader) must be fused together on a single chip. These are analytical devices that integrate a biorecognition element with and optical transducer.[2] The use of plasmonic materials leads to improved special resolution and low time response by enhancing surface-to-volume ratio which allows for down to a single molecule detection with high sensitivity.[32]

Plasmon-based device technologies demonstrated potential to complement conventional electronics and photonics. Semiconductors exhibit electrical properties that position their miniaturization as nanoscale elements for computation and information storage. Dielectrics on the other hand foster information travel over long distances and at a fast data rate. The limitation of semiconductor electronics is interconnect delay-time issues which limits processing speed, whereas dielectric photonics suffers from size limitation due to the fundamental laws of diffraction.[33] Plasmonics emerge as the link to bridge the size advantage of nanoelectronics with the speed advantage of dielectric photonics and provide synergy between the two technologies by interfacing with similar-speed photonic devices and with similar-size electronic components. In the last few decades, the concept of plasmons found applications in the development of high performance near-field optical microscopy and biosensing technologies.[34] More recent advances utilize plasmonics in thermally assisted magnetic recording, thermal cancer treatment, catalysis, and computer chips.[35]

Modern clinical biosensors are gradually shifting from off-site lab tests to near the patient on-site diagnosis. The shift is facilitated by the advancement in nanotechnology that allows for the integration of nanomaterials or structures with electrical devices. The implication is the development of a biosensor that is cheap, smaller in size, easy-to-use, and rapid in diagnosis.[23,36] These attributes make it fit for on-site diagnosis and point-of-care testing (POCT) like the ones already available for glucose and pregnancy testing. To achieve a POCT device, various components (such as light source, transducer, detector, and reader) must be fused together on a single chip.

Classes of SPR-Based Biosensors

Recent advances in nanotechnology such as the development of nano fabrications and visualization equipment’s has helped scale down the size of biosensors to micro or nano scale. This comes with benefits such as better signal-to-noise ratio, small sample volume requirement and lower cost.[37] Plasmonic biosensors can roughly be classified based on the configuration for exciting SPR into; Prism coupler-based and nanostructure/nanomaterial-based plasmonic biosensors. The prism coupler-based biosensors uses a continuous thin metallic films to excite a propagating plasmon waves known as surface plasmon polaritons (SPPs) whereas the nanostructure/nanomaterial-based biosensors use metal nanostructures and nanomaterials to excite localized surface plasmons (LSPRs) or both LSPR and SPP. Common characteristic of both resonances is the generation of evanescence field.

The prism coupler-based plasmonic biosensor: Free-space photon cannot directly excite SPP on a flat continuous metal surface because of its lower frequency and momentum than that of the surface free electrons. To excite SPP, the momentum of the incident photon must be increased to match that of the surface electrons. One way to achieve the matching condition is through the use of a prism coupler which can be positioned against the metal film in the Kretschmann configuration, or very close to a metal film in the otto configuration, thus creating an SPP as shown in Figure 2.1.[38] The excited plasmon produce an evanescent wave (electric field) that propagate up to ~100 nm at the interface between the metal layer and the dielectric.[16]

Figure 2.1. Title of SPR Chip Based on the (A) Kreschmann Coupling Configuration (B) Otto Coupling Configuration

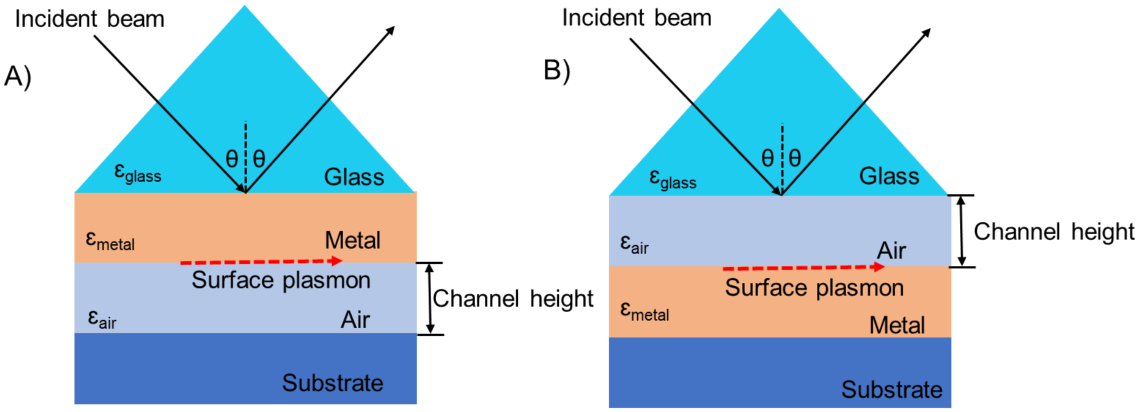

The sensitivity of the field to changes in RI at the metal/dielectric interface forms the basis upon which SPR biosensors are build.[39] By assessing the changes in the resonance condition (such as wavelength, intensity, phase or angle), the molecular interaction that occur at the sensor surface can be monitored directly in real time.[21] Although the Kretschmann and Otto configurations are efficient, label free, and facilitates the use of flow cells on top of the sensors, the use of a prism creates a bulky and complex instrumentation that makes them difficult to miniaturize and incorporate into a lab-on-a-chip systems. Nanostructures such as gratings or nanoparticles circumvent these challenges as they do not require optical couplers. Light scattering by the nanostructures provides the necessary momentum matching condition for SPR excitation.

Nanostructure/nanomaterial-based plasmonic biosensors: In the early 2000s LSPR biosensors based on metal nanostructures emerged as an alternative to biosensors based on propagating surface plasmons on thin continuous films.[21] LSPRs are excited when light interact with metal nanostructures that are smaller than the wavelength of the incident photons leading to a collective oscillation of surface electrons confined around the metal nanostructure.[21] The nanostructure (optical "nanoantennas") can amplify the intensity of incident light by more than 3-4 orders of magnitude.[40] The localized field has a decay length ~5-25 nm. LSPR wavelength position can be tuned by varying nanostructure size, shape and composition.[41] Several nanostructures have been engineered to excite plasmonic behaviour and enhance light signal for improved sensitivity and imaging resolution.

Nanoholes[42] and nanoslits[43,44,45,46] in thin metal films have recently become very attractive as they combine the characteristics of propagating SPR and LSPR, leading to enhanced light scattering or extraordinary optical transmission (EOT). The signal of sensors build on EOT phenomena are monitored based on shifts in wavelength position arising from changes in surface refractive index.[21],[47] Since biosensors based on EOT require light to pass through the sample, they can suffer optical loss especially if the analyte medium is absorptive or turbid like the human blood. Mitigation strategy will require the use and optimization of various plasmonic nanomaterials or structures to enhance optical signal and sensitivity.

Light-Metal Nanostructure Interactions

One of the most fundamental features of plasmonic nanostructures that popularized their practical application include (a) electric field confinement, (b) the generation of hot electrons (caused by the conversion of photon energy into hot electrons via plasmon decay) and (c) thermoplasmonic effects.[48] These effects are the three main important products of light-matter interaction at the nanoscale. Field enhancement occurs when light of designed wavelength propagates or is confined on a plasmonic nanostructure, for example, a metal film or nanoparticle resulting in the excitation and a collective resonant oscillation of surface electrons. Stronger light-metallic nanostructure interactions could result in the incident light absorption in the metallic nanostructure. This may lead to electron migration in the metallic film. The delocalized hot electron can lose its acquired energy via inelastic collection in the metal film. In this situation, energetic electrons can be harvested to generate current for photodetection if the plasmonic nanostructure is in contact with a semiconductor. The injection of these electrons into the conduction band of the semiconductor makes it possible for wide bandgap semiconductors to absorb light at longer wavelengths. Plasmonic structures improves the light absorption performance of 2D materials such as MoS_2,[49] and WS_2. [50] Metal nanostructures are effective optical antenna for enhancing the photo response of semiconductors, 2D materials and fluorescent molecules by increasing their absorption of light. In the situation where the hot electrons lose their energy (in form of heat) within the metal film, the temperature of the surrounding nanostructure spikes up. This effect is called thermosplasmonic effect of plasmonic nanostructures and has found application in energy harvesting, and photodetections.

Plasmon-Exciton Biosensors

Integrating fluorescence-based biosensors with plasmon-based biosensors represent the current state-of-the-art which has open up a new platform known as plasmon-exciton biosensor (PEB), applicable for drug discovery,[51] protein detection[52] and disease testing and monitoring.[53] Plasmon-exciton based optical sensors are integrated analytical devices that combine typical characteristics of plasmon fields with molecular fluorescence of an emitter to transduce biomolecular interactions into readable signals.[18] Such hybrid devices allow for the detection of small physiological changes from baseline values. In PEBs, the emitter (fluorescent molecule) is coupled with excited SPR field. The plasmon field act as the optical signal enhancer while the emitter serves as the transducer. The fluorescence of the emitter is amplified by the excited plasmon fields to improve optical signal transduction while benefiting from SPR field sensitivity. This process of optical enhancement is due to what is referred to as plasmon-exciton coupling.[54]

PEBs have existed for decades;[5556] for example, the Zepto reader, a medical sensor used for measuring human cytokines, dates back to the early 2000s.[57] Although the type and arrangement of material component might differ depending on the specific application, the characteristic building blocks of PEB are the substrate, plasmon materials, emitting materials, and light sources.[54] The efficiency of PEBs depends on the physical (e.g strength, elasticity, transparency, size geometry), electronic (e.g conductivity), optical and chemical influences on the substrate, plasmonic and emitting components of the PEBs.

This Review features the recent developments in plasmon-exciton based optical sensors with a specific focus on the components and sensing mechanisms to establish a framework for the design and implementation of optical devices for disease diagnostics. We examine the building blocks of PEBs, including substrate materials, signal amplification approaches, sensing mechanisms, by reflecting on the recent developments in the materials and engineering of these components. Finally, we use current trends to make predictions for the future trajectory of PEBs.

Components of a Plasmon-Exciton Biosensor

There are 3 major components comprised of the: substrate materials, plasmonic material and emitting exciton materials.

Substrate materials: The choice of substrate materials requires careful considerations to certain key properties. Not only is it desirable to have a transparent substrate, but also one with a range of mechanical properties befitting any optical sensor: toughness, and flexibility. This review focus on the two most widely used classes in optical sensor development: SiO_2 glass and synthetic polymers.

Synthetic polymers are the most widely adopted substrate materials in creating optical sensors. They can be fabricated using several available and scalable methods like molding, extrusion, deposition 3D printing, photolithography, lamination and milling.[58] The increasing demand for flexible, wearable electronics has stimulated the development of techniques like hydrogels because they can be impregnated with functional nanomaterials, they can be made conductive.[56] The use of polymers like PDMS and polycarbonates for developing optical sensors have been reported.[59,60] They are cheap and can easily be functionalized using techniques like O_3/UV irradiation, O_2 plasma irradiation and direct chemical functionalization. The use of metals or semiconductors as substrate materials are rare mainly because they lack transparency, flexibility and are relatively expensive.[61]

Plasmon materials: the unique optical behavior arising from light-matter interaction at the nanoscale requires the careful selection of plasmonic materials with requisite properties. Metals need to have a negative real part to exhibit SPR.[62] The overall materials in a PEB must not only have the individual properties necessary for the functioning of the hybrid system but also the synergy to integrate well with other functional materials; emitters. We emphasis on the most widely used classes in PEB development: noble/non-noble metals, metal oxides/nitrides, semiconductors, and nanomaterials.

Noble metals like silver and gold remain as one of the most popular class of plasmonic materials owing to their high quality factor.[63] One benefit of using noble metals in PEC is that their optical, magnetic, and electrical property, such as conductivity for reducing conduction optical losses have been extensively explored. Furthermore, they have already been proven to possess high figure-of-merit,[6465] which quantifies the quality of SPR necessary for visible light excitation and optical signal confinement required of a PEB. However, noble metals inherently lack certain desirable physical and chemical properties. Although silver, being the most electrically conducting metal, with the best plasmonic property has been widely used as plasmon field source, it lacks chemical stability. In the presence of air and moisture, it undergoes oxidation and tarnishes.[66,67] This is a chemical attribute that is undesirable in PEB components where fluids are mostly employed. Owing to this limitation,[68,69] magnesium and indium have been extensively explored as cheap and more stable plasmonic materials but they are susceptible to plasmonic field loss by generating hot electrons that relaxes by thermal dissipation. This reduces their performance in terms of sensitivity and optical signal detection. However, they perform well when applied as actuators in thermos-responsive polymers and photothermal therapy. [70,71] Other metals like aluminium show promise for plasmonic applications but are limited by ohmic losses.[72,73]

Gold, owing to its excellent conductivity, chemical inertness, and low SPR field loss, has been used to realize PEC sensors.[74] Gold nanostructures and thin films allow SPRs that can be probed using visible wavelengths of light. There are also available procedures for the routine functionalization of gold via gold-thiol interaction to develop highly sensitive sensors for detecting viruses,[75] bacteria,[76] heavy metals,[4] and gases.[77] However, gold is one of the most expensive noble metal and susceptible to conduction electron loss.[78,79,80] Transition metal nitrides (e.g titanium nitride, zircon nitride) and transparent oxides (e.g Al:ZnO, Ga:ZnO) are considered a substitute for gold owing to their low cost, high electron conductivity and mobility, high melting point, visible light frequencies and compatibility with complementary metal oxide semiconductor.[81] However, transition metal nitride films are sensitive to substrates including glass to exhibit textured growth or amorphous films with a different property than single-crystal films.

Figure 2.2. The Hype Cycle for the Plasmonic Field. Merging Plasmonics with Materials Science and Chemistry

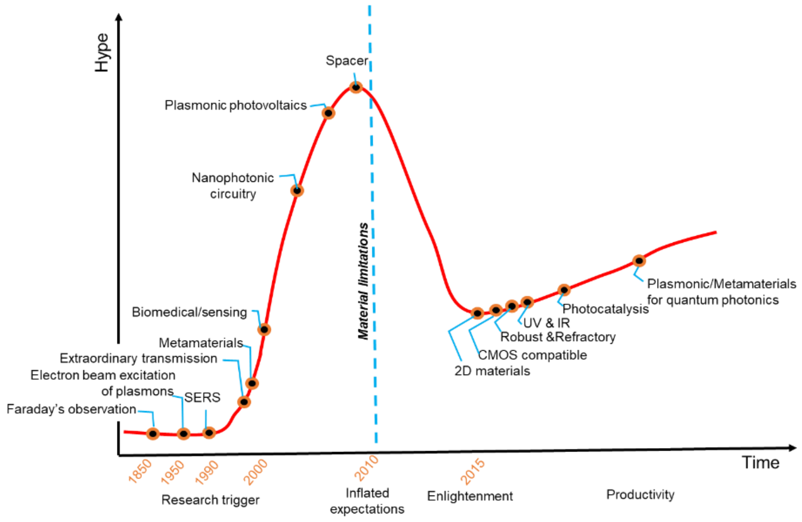

Noble metals are often used as optical field enhancers or transducers for PEC and continue to evolve to where other functional nanomaterials are incorporated as depicted in Figure 2.2.[82,83] The path of merging the materials can occur through modification of the noble metal before higher-order assembly, as demonstrated by incorporating of Au nanoparticles and magnetic nanoparticles with graphene,[84] depositing Ag onto Si substrate,[85] merging Au nanoparticles with QDs,[86] and replacing Au/Ag with graphene.[87] The hybridization of noble metal structures with nanomaterials further enhance the optical, electronic and mechanical features in terms of the SPR generation, conductivity, and flexibility required for developing miniaturized POC sensors.[88]

Although graphene can be considered a synthetic plasmonic nanomaterial, its unique properties, and vast applications in biosensing calls for its discussion as a separate class of material. Of key interest is the optical, electrical, magnetic and biocompatibility property of graphene, which since its development, increasing attention is given to its implementation in biosensing.[89] its high surface-to-volume ratio property allow for a high sensitivity that makes it especially biologically applicable. The biocompatibility of graphene makes it suitable for applications involving on skin, wound or body interfacing.[58] Graphene has been used in sensor devices for electrical, chemical and optical sensing,[90,91] and as a carrier for drug delivery.[92] The electronic property of graphene makes it the ideal material for use as electron transfer medium to prevent ohmic loss which occur from interaction between light and most plasmonic metals.

Recent questions in this area challenges the use of expensive noble metals and complex fabrication route to vary the geometry of nanostructures as a means of controlling and tuning plasmonic fields. New interest is shifting toward exploring nanostructure materials with plasmonic characteristic that are responsive to external stimuli to provide controlled tunability of optical characteristics without compromising cost, chemical, thermal, and optical stabilities. Noble metals lack this desirable behavior. Table 2.1 gives a summary of non-noble metals that have been explored and applied for biosensing.

Table 2.1 Summary of Plasmonic Materials, Their Optical Property and Application

Plasmon Material	Plasmon freq.	Availability	Advantage	Disadvantage	Application	Ref.
Cu	Vis-NIR	Earth abundant	Low-cost	Corrodes, oxidizes at room temp.	DNA detection	[105,106,107]
Al	UV-vis-NIR	Naturally abundant, easy to process	Low-cost, high performance	Corrodes	Protein detection	[108,109]
Doped SC (ITO)	IR	Synthetic	high performance	Complex doping, difficult to achieve visible frequency	Heavy metal detection in water	[110,111,112]
graphene	IR	Synthetic	Low ohmic loss than Ag and Au	-	Protein detection	[113,114]

Exciton materials: Fluorescent exciton materials like carbon nanodots and dyes are widely used in creating PEBs owing to their desirable properties.[93,94] First, there is a wide range of approaches to synthesizing stable fluorescent materials, including green methods such as facile-green strategy that employs natural precursors.[95] Fluorescent organic materials like perylene diimide,[96] fumaronitrile,[97] carbazole,[98] and triphenylamine[99] are cheaply available. This versatility readily provides access to numerous routes for creating PEB components with the desired stable optical property such as bright emission. Second, the optical and electronic properties of fluorescent materials can be modulated through a wide range of physical and chemical functionalization's. For decades, fluorescence materials have been used to tune the optical properties of commercial biosensors to achieve signal amplification and foster visibility to allow imaging and monitoring of complex cellular activities.[100] There are industrial exciton materials like quantum dots with inherent resistance to photobleaching, broad absorption that can be tuned and high fluorescent emission intensity, among other properties.[96] With such a varied plethora of functional materials, complex devices composed of excitonic materials enable the development of an array of sensors,[101] imaging probes,[102] and solar energy harvesters.[103] Most PEC sensors have used synthetic exciton materials, in which the material serves as the transducer to achieve the best sensitivity. PEBs can thus consist of a layer of emitting material and other nanomaterials assembled directly on a substrate or through a linking agent in a low-cost manner. Most PEC sensors fabricated from noble metals and synthetic dyes, or quantum emitters are designed to have a short lifetime, which, combined with difficulty in recycling, makes PEBs poorly sustainable. In response, researchers are pushing the boundaries of chemistry and engineering to create a new generation of functional nanomaterials and molecular emitters.[104]

Principle of Optical Signal Transduction

The transduction principle in optical sensors operate by causing a change in the absorption, transmission, reflection, refraction or frequency of light in response to the physical, chemical or biological change created by the biorecognition specie. PEBs are optical detection technique for quantifying biochemical and biophysical signals.[105] One of the advantages of PEBs is that the signal transduction can be realized with low-cost materials and electronics, and require low power. Plasmonic materials are employed for signal transduction due to their sensitivity to small changes in refractive index arising from either adsorption or desorption of biological species.[106] Depending on the scheme of the PEB, nanostructures on thin metal films, and nanomaterials like nanoparticles, nanowires, nanotubes, graphene are used as transducer or signal enhancer materials because of their higher electrical conductivity, small size, compatibility with biomolecules, high surface-to-volume ratio, chemical activity, mechanical strength, electrocatalytic properties and ability to amplify signals.[16]

Mechanism of Plasmon-Exciton Coupling

The interplay of energy between a metal and an emitter is profound in dictating optical signatures within the plasmon-exciton system. There are several competing processes that impact plasmon-exciton energy exchanges. The coupling of plasmon field with an exciton occur via dipole-dipole interactions.[107] This could lead to plasmon-induced resonance energy transfer (PIRET); where energy flows from plasmonic field to the emitter or Forster resonance energy transfer; where energy flows from the emitter to the metal. These two processes determine the emitter's fluorescence enhancement or quenching. Of interest, is the understanding of the parameters that can be varied to manipulate PIRET and FRET processes. The fluorescence of an emitter in proximity to a metal surface could be quenched due to transfer of photoinduced electronic charges back to the metal.[108] Consequently, the emitter dissociates non-radiatively. However, the electronic transfer could be minimized or hindered by an insulator, separating the emitter from the metal surface.

Strong plasmon field can also modify the radiative emission rate of an emitter. This is more pronounced if the emitter has a low quantum yield.[109] in addition, it will be beneficial if the emitter is located in precise hot-spot with the dipole moment of the two in alignment. This is difficult to achieve in experiment.[34]. For nanoparticles of size less than 20 nm, fluorescence quenching is always reported and it's unclear whether this is occurring via FRET or PIRET.[110,108,111]. Most strategies for modulating emission signal focus on the architecture of the plasmonic material. This is because the electromagnetic field plays a role in the absorption and emission rate of an emitter.

Optical Signal Amplification Strategies

At the core of every biosensor lies not only the need for sensitivity to small changes in analyte concentration interacting with the biorecognition element but also the ability of the transducing and amplification unit to convert and amplify those changes into a detectable output signal. Signal amplification strategies are classified into two: Amplification of fluorescence quenching and amplification of fluorescence emission. For both classes, we focus on considerations for exciton material, plasmonic nanostructure engineering and plasmon-exciton integration.

Quenching signal amplification: In this section, we review different approaches targeted at enhancing the quenching of optical signal as a means of recognizing bio-interactions. In these biosensors, an emitter is tethered onto one of the reacting biomolecules like the target element, such that binding events withing a plasmonic field region quenches the fluorescence of the attached emitter. This produces a turn-on or turn-off signals depending on how whether the target is bound or unbound to the recognition element within the plasmonic environment.[112] In this system, the emitter must have fluorescence emission, intense enough to be detected before getting to the plasmonic field region. That way, the fluorescence turn-off can easily be detected.[105]

Furthermore, the plasmon material must be engineered to excite near-surface fields such as the evanescence wave or localized fields with decay lengths of about tens of nanometers. This will mean that only emitters near the surface are quenched. This way, unwanted background signal from the bulk sample is limited allowing only the fluorescence quenching of emitters captured on the surface. However, careful consideration must be given to the nanomaterial type, shape and architecture to prevent having the reverse effect.[113] Emitters that are captured on the surface of a single or widely separated metal nanoparticles and planar metal surfaces produces the best quenching effects.[114] Biosensors build on this principle have been implemented in detecting DNA hybridization,[115] Pesticide biomarker,[116], Malaria aptamer (0.48 nM LOD), HIV,[117] Cancer, [118] and Covid-19.[53] However, complex tagging of the reactant molecules with emitters, low emission of emitters under direct illumination and poor signal to noise ratio have limited widescale use of this mode in developing optical sensors for other physiological monitoring.[119,120]

Emission signal amplification: One of the key reasons for coupling plasmons with excitons is to enhance the analytical performances of optical sensors via metal-enhanced fluorescence. However, if plasmon-exciton coupling is not done the right way, the opposite effect will occur. [88] There are two basic implications of plasmon-exciton coupling. (1) optical loss that occur when there is a spectral mismatch between the plasmon component and the fluorophore leading to energy reabsorption of the coupled state and dissipation of such energy as heat (2) fluorescence enhancement, which requires a given fluorophore to spectrally overlap with plasmonic component leading to optimal metal-enhanced fluorescence. Fluorescence enhancement improves the analytical performance of optical sensors. This is critical for the design of a sensitive and rapid disease detection device.

Alterations of morphology such as size and geometry of plasmonic nanostructure modulates plasmonic modes and hotspots.[120] This is of benefit to concentrating light in nanoscale volume which allows for efficient light-matter interaction and energy conversion efficiency, improvement in sensitivity, detection limit, simplification and miniaturization of analytical platforms and disease diagnostic devices for point-of-care applications.

Fluorescence enhancement in nanoparticle structure occur via dipole-dipole coupling interaction of fluorophores with the plasmonic nanoparticle to enhance both excitation and emission pathways.[88] The couple states impact emissive rates of fluorophores by decreasing the excited state lifetime. LSPR enhanced fluorescence depends on the distance between the fluorophore and the metal. The distance is often optimized to between 5-10 nm to minimize nonradiative energy transfer.[121] To avoid the use of spacers and still obtain emission enhancement, nanogap architecture has proved effective.

SPR in Nanogaps for Emission Enhancement

Fluorescence intensity depends on the intrinsic properties of the emitter and its immediate environment. For example, when the condition of spectral overlap between the emitters absorption or emission spectrum with the SPR field is met, attaching a fluorophore directly to a flat metal surface or nanoparticle could lead to fluorescence quenching caused by the transfer of excited electrons from the emitter to the metal's empty orbital.[122,95,123,124]. This cause of quenching can be minimized in two ways; first, a dielectric spacer (e.g SiO_2), [125,126] molecular spacers (e.g poly ethylene glycol),[127] or DNA linkers,[128] are required to maintain a nanoscale distance between the metal surface and the emitter.

Secondly, a localized high-density electromagnetic field states is required to surround the emitter thereby increasing the number of radiative states. To achieve this requires the employment of nanostructures such as nanoparticle dimers,[123] nanorods,[129] nanoholes[130] nanoslits,[131] and bowtie dimers,[132] with capability for plasmon-plasmon coupling with adjacent metal structures/surfaces to bring strong local field confinement.[133] The magnitude of field confinement depends on the size, geometry, physical and material properties of the metallic structure. Hence, a careful design, fabrication and optimization of metal nanostructures is critical. Some of the benefits of modulating the electromagnetic field in nanostructures is the potential for enhanced sensitivity and efficiency of optical biosensors, and control of energy transfer mechanisms and relaxation pathways. Many studies have demonstrated optical enhancements in nanogaps but there are enormous nanostructure shapes and emitters for which these effects have not yet been fully investigated.[134,135] Thus, a thorough understanding of the mechanism of PEC may unlock several new strategies to achieve a significant advancement in different research fronts. To get there will require addressing key challenges such as electron tunnelling which increases with the reduction in the size of nanostructures and compete with electric field enhancement.

Plasmonic nanogaps have shown high EM enhancements especially if the gap distance is in the sub-10 nm regime. Gaps of such sizes are small to accommodate large molecules like proteins or oligonucleotides. This limits their biosensing applications. The plasmon-plasmon coupling between adjacent metal surfaces produces a localized strong electric field that could induce emission enhancement. The Electric field enhancement also depends on the number of nanogaps between the adjacent nanoslits or particles.[136] More number of nanogaps profoundly enhances the electric field. This property could be used to enhance the sensitivity of sensors and the efficiencies of photovoltaics. Plasmonic nanopillar arrays with a centre-to-centre periodicity of 105.8 nm, H=108 nm, d=77.5, edge-to-edge separation=30.6 nm produced by a self-assembly of block copolymer colloids on a 100 mm Si wafer coated with an Au film was used to generate a uniform EM hot-spot. The authors reported a geometrical correlation between the structure, optical properties, and sensitivity of the nanopillar arrays in plasmonic assays. Their assay showed an analytical sensitivity with a LOD down to 120pM.[137]

In summary, this article highlights the classification, description, mechanisms, and examples of applications of plasmon-exciton based optical sensors in disease diagnostics, environmental monitoring, food safety and pharmacy. The PEC-based optical sensors are sensitive and selective to a wide range of analytes including viruses, bacteria, antibodies, DNAs, and tumor biomarkers. The principle of detection in PEBs provides ways of constructing simple and cheap analytical platforms with potential applications in personalized medicine for point-of-care sensing.

Conclusion and Perspectives

This Review highlights the strategies, current application and challenges of plasmon-exciton based optical sensors in disease diagnostics. Attempt was made to fundamentally interpret the processes of signal amplification and quenching in a plasmon-exciton system.

In this context, I believe that future efforts within the plasmon-exciton coupling strategy for optical signal amplification field will focus on emitters extension and nanostructure engineering extension. The processes of optical enhancements and quenching described above are applicable to other types of light-matter interaction areas, for example the electromagnetic field generation due to plasmon-exciton coupling could be used to enhance the efficiency of photovoltaic cells by increasing the light harvesting efficiency and tunability of absorption spectra. The surface plasmon resonance could also interact with exciton species to enhance photon absorption and excite hot electrons to interact with phonons and generate heat that could be used in cancer therapy and steam generation. The thermal generation property is also applicable in photocatalysing nanoscale reactions such as water splitting and CO_2 reduction. The PEC system could be applicable to SERS and scanning tunneling microscopy to enhance optical signal.

In the nanogap configuration such as nanoslit, the PEC setup is simple since it does not require complex optics (prism) to boost the momentum of incident photon. The gratings simply do the job and excite SPR field for the PEC system. Notably, the coupling efficiency can be modulated by varying the size, shape and number of gratings to excite SPR modes that overlaps well with the excitation or emission energies of the exciton material. On this basis, the diffraction-nanogap-based strategy could the path to the development of a portable PEB platform.

REFERENCES

1. Purohit, B., Vernekar, P. R., Shetti, N. P. & Chandra, P. Biosensor nanoengineering : Design , operation , and implementation for biomolecular analysis. *Sensors Int.* **1**, 100040 (2020).
2. Svitel, J. & Katrl, J. Optical biosensors Pavel Damborsk y. 91–100 (2016) doi:10.1042/EBC20150010.
3. Vashist, S. K. *et al.* Nanotechnology-Based Biosensors and Diagnostics : Technology Push versus Industrial / Healthcare Requirements. 115–126 (2012) doi:10.1007/s12668-012-0047-4.
4. Hassani, S. Recent Advances in Nanotechnology-Based Biosensors Development for Detection of Arsenic , Lead , Mercury , and Cadmium. 803–832 (2021).
5. Bordbar, M. M., Sheini, A., Hashemi, P., Hajian, A. & Bagheri, H. Disposable paper-based biosensors for the point-of-care detection of hazardous contaminations—a review. *Biosensors* **11**, 1–51 (2021).
6. Olalekan, O. B., T., O. V. & A., O. S. Study on Biochips Technology. *SSRN Electron. J.* (2017) doi:10.2139/ssrn.2947324.
7. Kim, J., Campbell, A. S., de Ávila, B. E. F. & Wang, J. Wearable biosensors for healthcare monitoring. *Nat. Biotechnol.* **37**, 389–406 (2019).
8. Gray, M. *et al.* Implantable biosensors and their contribution to the future of precision medicine. *Vet. J.* **239**, 21–29 (2018).
9. Thomas, H. Ingestible biosensors for gastrointestinal diagnosis. *Nat. Rev. Gastroenterol. Hepatol.* **15**, 455 (2018).
10. Liu, G. Grand Challenges in Biosensors and Biomolecular Electronics. **9**, 1–5 (2021).
11. Werley, C. A., Boccardo, S., Rigamonti, A., Hansson, E. M. & Cohen, A. E. Multiplexed Optical Sensors in Arrayed Islands of Cells for multimodal recordings of cellular physiology. *Nat. Commun.* **11**, 1–17 (2020).
12. Zhang, Y. *et al.* Multiplexed optical fiber sensors for dynamic brain monitoring. *Matter* **5**, 3947–3976 (2022).
13. Rodriguez-Lorenzo, L., Fabris, L. & Alvarez-Puebla, R. A. Multiplex optical sensing with surface-enhanced Raman scattering: A critical review. *Anal. Chim. Acta* **745**, 10–23 (2012).
14. Shen, Z. *et al.* Redox probes tagged electrochemical aptasensing device for simultaneous detection of multiple cytokines in real time. *Sensors Actuators, B Chem.* **336**, 129747 (2021).
15. Pei, X. *et al.* Nanomaterial-based multiplex optical sensors. *Analyst* **145**, 4111–4123 (2020).
16. Ali, B. D. M. and A. *Nanomaterials in Biosensors: Fundamentals and Applications*. (Nanomaterials for Biosensors, 2018).
17. Okumoto, S., Jones, A. & Frommer, W. B. Quantitative imaging with fluorescent biosensors. *Annu. Rev. Plant Biol.* **63**, 663–706 (2012).
18. Semeniak, D., Cruz, D. F., Chilkoti, A. & Mikkelsen, M. H. Plasmonic Fluorescence Enhancement in Diagnostics for Clinical Tests at Point-of-Care: A Review of Recent Technologies. *Adv. Mater.* **2107986**, (2022).
19. Suarasan, S., Tira, C., Rusu, M. M., Craciun, A. M. & Focsan, M. Controlled fluorescence

manipulation by core-shell multilayer of spherical gold nanoparticles: Theoretical and experimental evaluation. *J. Mol. Struct.* **1244**, 130950 (2021).

20. Ambartsumyan, O., Gribanyov, D., Kukushkin, V., Kopylov, A. & Zavyalova, E. SERS-based biosensors for virus determination with oligonucleotides as recognition elements. *Int. J. Mol. Sci.* **21**, 1–15 (2020).
21. Altug, H., Oh, S., Maier, S. A. & Homola, J. Advances and applications of nanophotonic biosensors. **17**, (2022).
22. Alrasheed, S. & Di Fabrizio, E. Effect of Surface Plasmon Coupling to Optical Cavity Modes on the Field Enhancement and Spectral Response of Dimer-Based sensors. *Sci. Rep.* **7**, 1–11 (2017).
23. Chen, Y. *et al.* Review of Integrated Optical Biosensors for Point-of-Care Applications. 1–22.
24. Salama, A. M., Yasin, G., Zourob, M. & Lu, J. Fluorescent Biosensors for the Detection of Viruses Using Graphene and Two-Dimensional Carbon Nanomaterials. *Biosensors* **12**, (2022).
25. Stokes, D. L., Alarie, J. P., Ananthanarayanan, V. & Vo-Dinh, T. Fiber Optics Sers Sensors for Environmental Monitoring. *Proc. SPIE* **3534**, 647 (1999).
26. S, B. & S, B. Plasmonic Sensors for Disease Detection - A Review. *J. Nanomed. Nanotechnol.* **7**, (2016).
27. Ruiz-Vega, G., Soler, M. & Lechuga, L. M. Nanophotonic biosensors for point-of-care COVID-19 diagnostics and coronavirus surveillance. *JPhys Photonics* **3**, (2021).
28. Camarca, A. *et al.* Emergent biosensing technologies based on fluorescence spectroscopy and surface plasmon resonance. *Sensors (Switzerland)* **21**, 1–35 (2021).
29. Qu, H. *et al.* Recent advances of fluorescent biosensors based on cyclic signal amplification technology in biomedical detection. *J. Nanobiotechnology* **19**, 1–28 (2021).
30. Cuadra, J. *et al.* Observation of Tunable Charged Exciton Polaritons in Hybrid Monolayer WS2-Plasmonic Nanoantenna System. *Nano Lett.* **18**, 1777–1785 (2018).
31. Ropers, C. *et al.* Grating-coupling of surface plasmons onto metallic tips: A nanoconfined light source. *Nano Lett.* **7**, 2784–2788 (2007).
32. Mauriz, E. Recent progress in plasmonic biosensing schemes for virus detection. *Sensors (Switzerland)* **20**, 1–27 (2020).
33. Brongersma, M. L. & Shalaev, V. M. The Case for Plasmonics. **440**, 10–12 (2012).
34. Kholmicheva, N., Romero, L. R., Cassidy, J. & Zamkov, M. Prospects and applications of plasmon-exciton interactions in the near-field regime. *Nanophotonics* **8**, 613–628 (2019).
35. Yoo, E. & Lee, S. Glucose Biosensors: An Overview of Use in Clinical Practice. 4558–4576 (2010) doi:10.3390/s100504558.
36. Noah, N. M. & Ndangili, P. M. Current Trends of Nanobiosensors for Point-of-Care Diagnostics. **2019**, (2019).
37. Hill, R. T. NIH Public Access. 1–28 (2016) doi:10.1002/wnan.1314.Plasmonic.
38. E. KRETSCHMANN and H . RAETHER. Radiative Decay of Non Radiative Surface Plasmons Excited by Light. *Z. Für Nat.* **23**, 2135–2136 (1968).
39. Homola, J. Present and future of surface plasmon resonance biosensors. *Anal. Bioanal. Chem.* **377**, 528–539 (2003).
40. Li, G., Shen, Y., Xiao, G. & Jin, C. Double-layered metal grating for high-performance refractive index sensing. *Opt. Express* **23**, 8995 (2015).

41. Ahn, H. *et al.* Plasmonic sensing, imaging, and stimulation techniques for neuron studies. *Biosens. Bioelectron.* **182**, 113150 (2021).
42. Chen, J. *et al.* Tungsten Disulfide-Gold Nanohole Hybrid Metasurfaces for Nonlinear Metalenses in the Visible Region. *Nano Lett.* **18**, 1344–1350 (2018).
43. Jun, Y. C., Pala, R. & Brongersma, M. L. Strong modification of quantum dot spontaneous emission via gap plasmon coupling in metal nanoslits. *J. Phys. Chem. C* **114**, 7269–7273 (2010).
44. Yoon, J. W., Lee, J. H., Song, S. H. & Magnusson, R. Unified theory of surface-plasmonic enhancement and extinction of light transmission through metallic nanoslit arrays. *Sci. Rep.* **4**, 1–7 (2014).
45. Wei, J., Waldeck, D. H., Kofke, M. & Singhal, S. JSM Nanotechnology & Nanomedicine A Study of Localized Surface Plasmon Resonance Nanoslit Array and Applications for Chip-based Protein Detection. *JSM Nanotechnol Nanomed* **2**, 1–8 (2014).
46. Zeng, B., Gao, Y. & Bartoli, F. Ultrathin plasmonic nanogratings for rapid and highly-sensitive detection. 1–11.
47. Dutta, A. *et al.* Biosensors and Bioelectronics Controlling distance , size and concentration of nanoconjugates for optimized LSPR based biosensors. *Biosens. Bioelectron.* **170**, 112657 (2020).
48. Lin, K. Te, Lin, H. & Jia, B. Plasmonic nanostructures in photodetection, energy conversion and beyond. *Nanophotonics* **9**, 3135–3163 (2020).
49. Li, J. *et al.* Enhancement of the Photoresponse of Monolayer MoS2 Photodetectors Induced by a Nanoparticle Grating. *ACS Appl. Mater. Interfaces* **12**, 8429–8436 (2020).
50. Dubey, P. K. & Tripathi, L. N. Hybrid metal nanoantenna 2D-material photovoltaic device. *Sol. Energy Mater. Sol. Cells* **200**, 109918 (2019).
51. Bhalla, N. & Estrela, P. Exploiting the signatures of nanoplasmon-exciton coupling on proton sensitive insulator-semiconductor devices for drug discovery applications. *Nanoscale* **10**, 13320–13328 (2018).
52. Lee, J., Hernandez, P., Lee, J., Govorov, A. O. & Kotov, N. A. Exciton-plasmon interactions in molecular spring assemblies of nanowires and wavelength-based protein detection. *Nat. Mater.* **6**, 291–295 (2007).
53. Taubner, B., Gibbons, A. & Cady, N. C. Dual detection of COVID-19 antigens and antibodies using nanoscale fluorescent plasmonic substrates. *Exp. Biol. Med.* **247**, 2081–2089 (2022).
54. Bauch, M., Toma, K., Toma, M., Zhang, Q. & Dostalek, J. Plasmon-Enhanced Fluorescence Biosensors: A Review. *Plasmonics* **9**, 781–799 (2014).
55. Seidel, M. & Niessner, R. Automated analytical microarrays: A critical review. *Anal. Bioanal. Chem.* **391**, 1521–1544 (2008).
56. Toma, K., Dostalek, J. & Knoll, W. Fluorescence Emission for Biosensor Applications. *Opt. Express* **19**, 97–106 (2011).
57. Pawlak, M. *et al.* Zeptosens' protein microarrays: A novel high performance microarray platform for low abundance protein analysis. *Proteomics* **2**, 383–393 (2002).
58. Ates, H. C. *et al.* End-to-end design of wearable sensors. *Nat. Rev. Mater.* **7**, 887–907 (2022).
59. Tukur, F. *et al.* Plasmon–Exciton Coupling Effect in Nanostructured Arrays for Optical Signal Amplification and SARS-CoV-2 DNA Sensing. *ACS Appl. Nano Mater.* **6**, 2071–

2082 (2023).
60. Chang, C. *et al.* Flexible Localized Surface Plasmon Resonance Sensor with Metal–Insulator–Metal Nanodisks on PDMS Substrate. *Sci. Rep.* **8**, (2018).
61. Lee, K. L., Huang, J. Bin, Chang, J. W., Wu, S. H. & Wei, P. K. Ultrasensitive biosensors using enhanced fano resonances in capped gold nanoslit arrays. *Sci. Rep.* **5**, 1–9 (2015).
62. Zhou, J., Wang, Y., Zhang, L. & Li, X. Plasmonic biosensing based on non-noble-metal materials. *Chinese Chem. Lett.* **29**, 54–60 (2018).
63. Gutiérrez, Y., Brown, A. S., Moreno, F. & Losurdo, M. Plasmonics beyond noble metals: Exploiting phase and compositional changes for manipulating plasmonic performance. *J. Appl. Phys.* **128**, (2020).
64. Doiron, B. *et al.* Quantifying Figures of Merit for Localized Surface Plasmon Resonance Applications: A Materials Survey. *ACS Photonics* **6**, 240–259 (2019).
65. Shim, H., Kuang, Z. & Miller, O. D. Optical materials for maximal nanophotonic response [Invited]. *Opt. Mater. Express* **10**, 1561 (2020).
66. Cells, B. P. Addition to “ Plasmon − Exciton Coupling in Photosystem I Based Biohybrid Photoelectrochemical Cells ”. **9**, 2019 (2019).
67. Zeng, Z. *et al.* Protein Trapping in Plasmonic Nanoslit and Nanoledge Cavities: The Behavior and Sensing. *Anal. Chem.* **89**, 5221–5229 (2017).
68. Appusamy, K., Jiao, X., Blair, S., Nahata, A. & Guruswamy, S. Mg thin films with Al seed layers for UV plasmonics. *J. Phys. D. Appl. Phys.* **48**, (2015).
69. Kumamoto, Y. *et al.* Indium for Deep-Ultraviolet Surface-Enhanced Resonance Raman Scattering. *ACS Photonics* **1**, 598–603 (2014).
70. Baffou, G. & Quidant, R. Thermo-plasmonics: Using metallic nanostructures as nano-sources of heat. *Laser Photonics Rev.* **7**, 171–187 (2013).
71. Wang, W. *et al.* Hot Electron-Based Near-Infrared Photodetection Using Bilayer MoS2. *Nano Lett.* **15**, 7440–7444 (2015).
72. Gérard, D. & Gray, S. K. Aluminium plasmonics. *J. Appl. Phys.* **48**, (2015).
73. Tobing, L. Y. M. *et al.* Plasmon-exciton systems with high quantum yield using deterministic aluminium nanostructures with rotational symmetries. *Nanoscale* **11**, 20315–20323 (2019).
74. Zhang, X., Guo, Q. & Cui, D. Recent Advances in Nanotechnology Applied to Biosensors. 1033–1053 (2009) doi:10.3390/s90201033.
75. Moitra, P. *et al.* Selective Naked-Eye Detection of SARS-CoV-2 Mediated by N Gene Targeted Antisense Oligonucleotide Capped Plasmonic Nanoparticles. *ACS Nano* **14**, 7617–7627 (2020).
76. Soler, M., Belushkin, A., Cavallini, A., Kebbi-beghdadi, C. & Greub, G. Biosensors and Bioelectronics Multiplexed nanoplasmonic biosensor for one-step simultaneous detection of Chlamydia trachomatis and Neisseria gonorrhoeae in urine. *Biosens. Bioelectron.* **94**, 560–567 (2017).
77. Becerra, J., Gopalakrishnan, V. N., Quach, T. A. & Do, T. O. Plasmonic Materials: Opportunities and Challenges on Reticular Chemistry for Photocatalytic Applications. *ChemCatChem* **13**, 1059–1073 (2021).
78. Patsalas, P., Kalfagiannis, N. & Kassavetis, S. Optical properties and plasmonic performance of titanium nitride. *Materials (Basel).* **8**, 3128–3154 (2015).
79. Karaballi, R. A., Monfared, Y. E. & Dasog, M. Overview of Synthetic Methods to Prepare

Plasmonic Transition-Metal Nitride Nanoparticles. *Chem. - A Eur. J.* **26**, 8499–8505 (2020).

80. Gururaj V. Naik, Jeremy L. Schroeder, Xingjie Ni, Alexander V. Kildishev, Timothy D. Sands, and A. B. Titanium nitride as a plasmonic material for visible and near-infrared wavelengths. *Opt. Mater. Express* **4**, 534–537 (2012).
81. Gururaj V. Naik, Jongbum Kim, and A. B. Oxides and nitrides as alternative plasmonic materials in the optical range. *Phys. Rev. Lett.* **1**, (2011).
82. Guler, U., Kildishev, A. V., Boltasseva, A. & Shalaev, V. M. Plasmonics on the slope of enlightenment: The role of transition metal nitrides. *Faraday Discuss.* **178**, 71–86 (2015).
83. Jadidi, M. M. *et al.* Tunable Terahertz Hybrid Metal-Graphene Plasmons. *Nano Lett.* **15**, 7099–7104 (2015).
84. Lee, J., Takemura, K., Kato, C. N., Suzuki, T. & Park, E. Y. Binary Nanoparticle Graphene Hybrid Structure-Based Highly Sensitive Biosensing Platform for Norovirus-Like Particle Detection. *ACS Appl. Mater. Interfaces* **9**, 27298–27304 (2017).
85. Austin Suthanthiraraj, P. P. & Sen, A. K. Localized surface plasmon resonance (LSPR) biosensor based on thermally annealed silver nanostructures with on-chip blood-plasma separation for the detection of dengue non-structural protein NS1 antigen. *Biosens. Bioelectron.* **132**, 38–46 (2019).
86. Li, X. *et al.* A fast and sensitive immunoassay of avian influenza virus based on label-free quantum dot probe and lateral flow test strip. *Talanta* **100**, 1–6 (2012).
87. Chen, J. *et al.* Strong plasmon reflection at nanometer-size gaps in monolayer graphene on SiC. *Nano Lett.* **13**, 6210–6215 (2013).
88. Fontaine, N., Picard-Lafond, A., Asselin, J. & Boudreau, D. Thinking outside the shell: Novel sensors designed from plasmon-enhanced fluorescent concentric nanoparticles. *Analyst* **145**, 5965–5980 (2020).
89. Xu, S. *et al.* Real-time reliable determination of binding kinetics of DNA hybridization using a multi-channel graphene biosensor. 1–10 (2017) doi:10.1038/ncomms14902.
90. Jiang, S. *et al.* Real-time electrical detection of nitric oxide in biological systems with sub-nanomolar sensitivity. *Nat. Commun.* **4**, (2013).
91. Rakhilin, N. *et al.* Simultaneous optical and electrical in vivo analysis of the enteric nervous system. *Nat. Commun.* **7**, 1–7 (2016).
92. Yang, K., Feng, L. & Liu, Z. The advancing uses of nano-graphene in drug delivery. *Expert Opin. Drug Deliv.* **12**, 601–612 (2015).
93. Zhou, L. *et al.* Enhancement of immunoassay's fluorescence and detection sensitivity using three-dimensional plasmonic nano-antenna-dots array. *Anal. Chem.* **84**, 4489–4495 (2012).
94. Gayen, B., Palchoudhury, S. & Chowdhury, J. Carbon dots: A mystic star in the world of nanoscience. *J. Nanomater.* **2019**, (2019).
95. Miao, H., Wang, L., Zhuo, Y., Zhou, Z. & Yang, X. Label-free fluorimetric detection of CEA using carbon dots derived from tomato juice. *Biosens. Bioelectron.* (2016) doi:10.1016/j.bios.2016.06.043.
96. Würthner, F. Perylene bisimide dyes as versatile building blocks for functional supramolecular architectures. *Chem. Commun.* **4**, 1564–1579 (2004).
97. Panthi, K., Adhikari, R. M. & Kinstle, T. H. Visible and near IR emitting organic nanoparticles of aromatic fumaronitrile core-based donor-acceptor compounds. *J.*

Photochem. Photobiol. A Chem. **215**, 179–184 (2010).

98. Palayangoda, S. S., Cai, X., Adhikari, R. M. & Neckers, D. C. Carbazole-based donor-acceptor compounds: Highly fluorescent organic nanoparticles. *Org. Lett.* **10**, 281–284 (2008).
99. Ishi-i, T. *et al.* Amphiphilic benzothiadiazole-triphenylamine-based aggregates that emit red light in water. *Org. Biomol. Chem.* **13**, 1818–1828 (2015).
100. Denis Svechkarev, A. M. M. Organic Fluorescent Dye-based Nanomaterials: Advances in the Rational Design for Imaging and Sensing Applications. *Curr. Med. Chem.* **26**, 4042–4064 (2019).
101. Sultangaziyev, A. & Bukasov, R. Review: Applications of surface-enhanced fluorescence (SEF) spectroscopy in bio-detection and biosensing. *Sens. Bio-Sensing Res.* **30**, (2020).
102. Li, J. F., Li, C. Y. & Aroca, R. F. Plasmon-enhanced fluorescence spectroscopy. *Chem. Soc. Rev.* **46**, 3962–3979 (2017).
103. Lin, G., Dong, W. & Zhang, R. Plasmon enhanced fluorescence of photosynthetic complexes by conjugating with gold micro-plates and their single-particle sensing application. *Sensors Actuators B Chem.* **371**, 1–20 (2022).
104. Hertzog, M., Wang, M., Mony, J. & Börjesson, K. Strong light-matter interactions: A new direction within chemistry. *Chem. Soc. Rev.* **48**, 937–961 (2019).
105. He, M. Q., Yu, Y. L. & Wang, J. H. Biomolecule-tailored assembly and morphology of gold nanoparticles for LSPR applications. *Nano Today* **35**, 101005 (2020).
106. Monitoring, E. *et al.* Nanobiosensors : applications in biomedical technology. (2020) doi:10.1088/1757-899X/805/1/012028.
107. Sugawa, K. *et al.* Metal-enhanced fluorescence platforms based on plasmonic ordered copper arrays: Wavelength dependence of quenching and enhancement effects. *ACS Nano* **7**, 9997–10010 (2013).
108. Bian, Y. *et al.* Distance-Dependent Plasmon-Enhanced Fluorescence of Submonolayer Rhodamine 6G by Gold Nanoparticles. *Nanoscale Res. Lett.* **16**, (2021).
109. Breshike, C. J., Riskowski, R. A. & Strouse, G. F. Leaving Förster resonance energy transfer behind: Nanometal surface energy transfer predicts the size-enhanced energy coupling between a metal nanoparticle and an emitting dipole. *J. Phys. Chem. C* **117**, 23942–23949 (2013).
110. Dulkeith, E. *et al.* Fluorescence Quenching of Dye Molecules near Gold Nanoparticles: Radiative and Nonradiative Effects. *Phys. Rev. Lett.* **89**, 12–15 (2002).
111. Li, X., Qian, J., Jiang, L. & He, S. Fluorescence quenching of quantum dots by gold nanorods and its application to DNA detection. *Appl. Phys. Lett.* **94**, 1–4 (2009).
112. Mabrouk, M., Hammad, S. F., Abdella, A. A. & Mansour, F. R. A novel strategy for ketorolac detection based on turn-on plasmonic enhanced FRET synchronous fluorometric sensor employing micellized chitosan/ AgNPs nanocomposites: Preparation and mechanism investigation. *Colloids Surfaces A Physicochem. Eng. Asp.* **614**, 126182 (2021).
113. Shrivastav, A. M., Cvelbar, U. & Abdulhalim, I. A comprehensive review on plasmonic-based biosensors used in viral diagnostics. *Commun. Biol.* **4**, 1–12 (2021).
114. Liu, S. Y. *et al.* Simultaneous excitation and emission enhancement of fluorescence assisted by double plasmon modes of gold nanorods. *J. Phys. Chem. C* **117**, 10636–10642 (2013).

115. Zhu, Z. *et al.* Plasmon-Enhanced Fluorescence in Coupled Nanostructures and Applications in DNA Detection. *ACS Appl. Bio Mater.* **1**, 118–124 (2018).
116. Zou, Z. *et al.* Quantum Dot-Based Immunochromatographic Fluorescent Biosensor for Biomonitoring Trichloropyridinol , a Biomarker of Exposure to Chlorpyrifos. **82**, 5125–5133 (2010).
117. Inci, F. *et al.* Nanoplasmonic quantitative detection of intact viruses from unprocessed whole blood. *ACS Nano* **7**, 4733–4745 (2013).
118. Mohammadi, S., Salimi, A., Hamd-Ghadareh, S., Fathi, F. & Soleimani, F. A FRET immunosensor for sensitive detection of CA 15-3 tumor marker in human serum sample and breast cancer cells using antibody functionalized luminescent carbon-dots and AuNPs-dendrimer aptamer as donor-acceptor pair. *Anal. Biochem.* **557**, 18–26 (2018).
119. Baghramyan, H. M. & Ciracì, C. Fluorescence quenching in plasmonic dimers due to electron tunneling. *Nanophotonics* **11**, 2473–2482 (2022).
120. Su, Q., Jiang, C., Gou, D. & Long, Y. Surface Plasmon-Assisted Fluorescence Enhancing and Quenching: From Theory to Application. *ACS Appl. Bio Mater.* **4**, 4684–4705 (2021).
121. Bergveld, P. Development of an ion-sensitive solid-state device for neurophysiological measurements. *IEEE Trans. Biomed. Eng.* **7**, 13957–13962 (1970).
122. Glass, A. M., Liao, P. F., Bergman, J. G. & Olson, D. H. Interaction of metal particles with adsorbed dye molecules: absorption and luminescence. *Opt. Lett.* **5**, 368 (1980).
123. Toropov, N. A. *et al.* Direct enhancement of luminescence of CdxZn1−xSeyS1−y/ZnS nanocrystals with gradient chemical composition by plasmonic nanoantennas. *Opt. Laser Technol.* **121**, 105821 (2020).
124. Mourdikoudis, S. & Pallares, R. M. Characterization techniques for nanoparticles : comparison and complementarity upon studying. 12871–12934 (2018) doi:10.1039/c8nr02278j.
125. Naiki, H. *et al.* Highly controlled plasmonic emission enhancement from metal-semiconductor quantum dot complex nanostructures. *J. Phys. Chem. C* **117**, 2455–2459 (2013).
126. Liu, N., Prall, B. S. & Klimov, V. I. Hybrid Gold / Silica / Nanocrystal-Quantum-Dot Superstructures : Synthesis and Analysis of Semiconductor - Metal Interactions. 15362–15363 (2006).
127. Lee, J., Govorov, A. O. & Kotov, N. A. Nanoparticle assemblies with molecular springs: A nanoscale thermometer. *Angew. Chemie - Int. Ed.* **44**, 7439–7442 (2005).
128. Gueroui, Z. & Libchaber, A. Single-molecule measurements of gold-quenched quantum dots. *Phys. Rev. Lett.* **93**, 1–4 (2004).
129. Trotsiuk, L. *et al.* Plasmon-enhanced fluorescence in gold nanorod-quantum dot coupled systems. *Nanotechnology* **31**, 105–201 (2020).
130. Dovzhenko, D. S., Ryabchuk, S. V., Rakovich, Y. P. & Nabiev, I. R. Light-matter interaction in the strong coupling regime: Configurations, conditions, and applications. *Nanoscale* **10**, 3589–3605 (2018).
131. Li, X., Zhou, L., Hao, Z. & Wang, Q. Q. Plasmon–Exciton Coupling in Complex Systems. *Adv. Opt. Mater.* **6**, 1–21 (2018).
132. Pelton, M., Storm, S. D. & Leng, H. Strong coupling of emitters to single plasmonic nanoparticles: Exciton-induced transparency and Rabi splitting. *Nanoscale* **11**, 14540–14552 (2019).

133. Halas, N. J., Lal, S., Chang, W.-S., Link, S. & Nordlander, P. Plasmons in Strongly Coupled Metallic Nanostructures. *Chem. Rev.* **111**, 3913–3961 (2011).
134. Govorov, A. O. *et al.* Exciton-plasmon interaction and hybrid excitons in semiconductor-metal nanoparticle assemblies. *Nano Lett.* **6**, 984–994 (2006).
135. Liu, L. *et al.* Strong Plasmon–Exciton Interactions on Nanoantenna Array–Monolayer WS2 Hybrid System. *Adv. Opt. Mater.* **8**, 1–8 (2020).
136. Chou, S. Y. *et al.* Romantic Story or Raman Scattering? Rose Petals as Ecofriendly, Low-Cost Substrates for Ultrasensitive Surface-Enhanced Raman Scattering. *Anal. Chem.* **87**, 6017–6024 (2015).
137. Rastogi, R. *et al.* Analyte Co-localization at Electromagnetic Gap Hot-Spots for Highly Sensitive (Bio)molecular Detection by Plasmon Enhanced Spectroscopies. *ACS Appl. Mater. Interfaces* **13**, 9113–9121 (2021).

CHAPTER III: PLASMON-EXCITON COUPLING IN NANOSLIT ARRAYS FOR SIGNAL APMPLIFICATION AND BIOSENSING

This chapter has been published as: Frank Tukur, Bhawna Bagra, Anitha Jayapalan, Mengxin Liu, Panesun Tukur, Jianjun Wei. “Plasmon-Exciton Coupling Effect in Nanostructured Arrays for Optical Signal Amplification and SARS-CoV-2 DNA Sensing.” ACS Appl. Nano Mater. 2023, 6(3), 2071-2082.

Overview

A surface plasmon resonance (SPR)-enhanced optical signal using a nanoslit array and acridine orange (AO) dye system was reported on a flexible, gold coated polydimethylsiloxane (PDMS) substrate and was used to demonstrate a simple sensing scheme to directly detect SARS-CoV-2 Nucleic Acid via DNA hybridization. A simple nanoimprinting pattern transfer technique was introduced to form a uniform, reproducible nanoslit arrays where the dimensions of the slit array were controlled by the thickness of the gold film. The plasmon-exciton coupling effect on the optical enhancement of different dye molecules, i.e., AO, propidium iodide (PI), or dihydroethidium (DHE) attached to the nanoslit surfaces, was examined thoroughly by measuring the surface reflection and fluorescence imaging. The results indicate that the best overlap of plasmon resonance wavelength to the excitation spectrum of AO presented the largest optical enhancement (~57×) compared to the signal at flat gold surfaces. Based on this finding, a sensitive assay for detecting DNA hybridization was generated using the interaction of the selected SARS-CoV-2 ssDNA and dsDNA with AO to trigger the metachromatic behavior of the dye at the nanoarray surfaces. We found strong optical signal amplification on the formation of acridine-ssDNA complexes and quenched signal upon hybridization to the complementary target DNA (ct-DNA) along with blue-shift in the optical signal of AO-dsDNAs. A quantitative evaluation of the ct-DNA concentration in a concentration range of 100 nM to 0.08 nM using both the reflection and emission imaging signals demonstrated two linear regimes with the lowest detection limit of 0.21 nM. The sensing scheme showed high sensitivity and distinguished signals for 1-, 2- and 3-base mismatched DNA targets, as well as high stability and reusability. This approach towards enhancing optical signal for DNA sensing offers promise in a general, rapid, and direct vision detection method for nucleic acid analytes.

Introduction

While tremendous progresses have been made in the development of plasmon-enhanced fluorescence (PEF) of emitters placed in the vicinity of a metal-dielectric nanostructure (NS) interface, there still exist a growing need for NS designs that offer high optical signal for portable and wearable point-of-care analytical devices. Currently, PEF emission systems have demonstrated a practicable application for the detection of biological molecules.[1-2] Their efficiency in detecting low molecular concentrations depends greatly on the ability of the nanostructures to trap the electromagnetic field that couples well with the surrounding emitter species.[3-5] This presents an interesting challenge since small variations in the geometry, size, and type of metals used can cause a significant difference in the magnitude and wavelength position of electromagnetic fields concentrated in the NS area. Therefore, a rational design of the plasmonic nanostructure and cautious selection of an emitter whose optoelectronic property is a match for interaction with plasmonic fields is necessary.[6-8]

The interaction of light with an optically active species of nanoscale or less dimension is generally less efficient due to a size mismatch between the species and wavelength of light which leads to poor energy conversion. In order to maximize light absorption, emission, or scattering, plasmonic nanostructures have been utilized to confine electromagnetic field and to strongly couple it with optically active materials.[9-11] One of the resultant plasmon-exciton coupling systems serves to increase the local density of optical states and consequently improve the spontaneous emission rate commonly referred to as the Purcell effect.[12-13] This approach has been implemented especially for the significant enhancement of photoluminescence (PL) of quantum dots, carbon nanodots, and molecular dyes placed in the near-field vicinity of a plasmonic NS.[14-17] Such enhancement offers huge potential applications for increasing the optical absorption and the fluorescence intensity of metal-coupled fluorophores.[13, 18]

However, the PL emission can be a cumulative influence of the energy interplay between the metal and the fluorophore in a PEC system. This interaction can lead to either emission enhancement via plasmon-induced resonance energy transfer or quenching via Forster resonance energy transfer (FRET).[19-20] Such effects depend on whether an emitter is directly attached to a single nanoparticle, planar metallic surface or placed in a metallic cavity.[20] Although the absorption of an emitter is enhanced by the near field of a plasmonic nanostructure, attaching it directly to a metal surface may result in fluorescence quenching of the excited state rather than enhancement.[12, 21] This behaviour has been explained in terms of the transfer of excited electrons from the emitter (fluorophore) to the metal's empty orbital.[22] To mitigate quenching effects, localized high-density electromagnetic field states is required to surround the emitter thereby increasing the number of radiative states. To achieve this, various shapes and configurations that utilize nanoparticle dimers,[12] nanorods,[23] nanoholes,[24] nanoslits,[25] and bowtie dimers[8] have been explored. Notably, when an emitter is sandwiched between two or more metal structures, fluorescence emission is enhanced due to strong local field enhancement caused by plasmon-plasmon coupling between adjacent metal structures.[26-27] This gives nanodimers and nanoslits an edge in practical application over single nanoparticle, nanorods and flat metallic surfaces.

However, careful optimization of the proximity between dimers and nanocavity width is necessary to prevent electron tunnelling which can also result in quenching.[28]

Although the localized surface plasmon resonance (LSPR) excited in nanoparticle dimers offer enhanced field intensity by many orders of magnitude,[29] controlling their precise orientation and separation is a challenge.[30-31] On the other hand, surface plasmon polariton (SPP)-based nanostructures generate a relatively more uniform electric field but suffer from low intensity field generation. In order to compensate for each other's demerits, it is desirable to excite both LSP and SPP modes in a single system. Such an approach may produce a much higher field confinement and a better PL enhancement.

In this work, we investigate light-matter interaction between small molecular fluorescence dyes and an Au nanoslit array structure fabricated on a flexible substrate. The suitability of the Au nanoslit cavity on the substrate toward PL enhancement of three different dye species, namely acridine orange (AO), propidium iodide (PI) or dihydroethidium (DHE), was examined through coupling of the species to the plasmonic slit structure. The nanoslit offer one of the best ways of manipulating optical field generation and propagation that gives a promising enhancement of fluorescence intensity due to their ability to simultaneously shelter both LSP resonance (at the top and bottom edges) and SPP (at the two side walls of the slit) modes, providing a superior platform for light-matter interactions where both the emission and excitation of nearby optically active specie can be influenced.[5, 32-34] Another advantage of using the nanoslit array lies in its geometry which allows convenient placement and accommodation of optically active materials and creates avenues towards its widescale adoption in flow-through devices for biomolecular sensing application.[34] We also investigate the interrelationship of nanostructure-generated plasmon with emission and excitation components of the photoactive species. Our efforts are directed toward determining the excitation/emission wavelength requirement of an emitter necessary for optimum coupling with the plasmonic fields. To achieve this, we studied the optical response of fluorescence molecules (AO, PI and DHE) with different emission wavelength varying from ~422 and 625 nm placed in gold nanoslit of different widths.

Recently, the world was hit hard by a viral pandemic, COVID-19 which as of October 14, 2022, the WHO reported 620,878,405 confirmed cases including 6,543,138 deaths and still counting. To minimize the harm from this pandemic and better prepare for future repeat of COVID-19 and other pandemics, rapid and portable diagnostic tools are urgently needed. Currently, viral detection employs methods that require polymerase chain reaction, virus isolation and enzyme-linked immunosorbent assay (ELISA).[35] The need for newer methodologies for diagnosis of rapid turnaround time, simple operation and direct readout continues to rise. Plasmonic-based sensors have displayed high detection speed, sensitivity, portability and thus promising for disease diagnosis.[36-37] For instance, combining LSPR of different NPs to optical fibers has demonstrated advantages of miniaturization and portability in detection of both small and large biomolecules.[38-39] Viral biosensors can be categorized based on their viral targets into antigen-, cell-, immune-, and DNA-based sensors.[40-44] The predictable and specific hybridization of the complementary bases that are based on nucleic acid hybridization of DNA- viral targets have demonstrated preserved reactivity, stability, accessibility, and low cost.

Herein, we further potentiate the feasibility and high efficiency of the AO-based optical enhancement platform for the sensitive detection of COVID-19 nucleic acids. AO is a versatile molecule widely adopted for cell differentiation, staining and routine quantification of DNA[45] and bacteria[46] due to its fluorescence and cationic features. Owing to its optical and electronic properties, it is considered one of the most potent candidates for the development of DNA targeted drugs and chemotherapy.[47] Being cationic makes AO suitable for electrostatic interaction with ssDNA and also intercalates with dsDNA.[48-49] These interactions produce unique changes in the emission intensity and color of the dye molecule. Unlike most dyes that produce identical emission spectra for ssDNA and dsDNA, AO exhibits a metachromatic behavior by distinguishably producing red (650 nm) fluorescence when coupled with ssDNA and green (525 nm) with dsDNA.[50] This behavior is key in generating a new form of optical behavior that can be used to discriminate between ssDNA and dsDNA. To develop an AO-based surface optical sensor for DNA differentiation it is necessary to determine the ratio of AO to DNA since certain concentration levels of AO can lead to precipitation or DNA denaturization.[51-52] Complying with this prerequisite in our nanoslit array system, we adopted a well-tested concentration of AO that circumvents precipitation and denaturization concerns over a very wide range of DNA concentration.[50]

Figure 3.1 shows the schematic illustration for the designed optical DNA hybridization sensor and operation principle. The blank Au nanoslit is designed to have a plasmonic resonance peak at around 650 nm. A self-assembled monolayer (SAM) of 11-mercaptoundecanoic acid (11-MUA) and 8-mercaptooctanol (8-MO) at the nanoslit gold surface allows the covalent attachment of AO at the emission of 525 nm. The surface-bound AO could electrostatically interact with ssDNA probes causing AO to shift emission to 650 nm which matches the best to the plasmonic resonance wavelength, resulting in enhancement of the optical signal. Finally, the hybridization of the ssDNAs with the ct-DNA species results in a significant decrease of the optical signal at 650 nm because the AO-dsDNA complex emits at 525 nm. The optical response difference is used as a signal transduction for detecting the DNA hybridization.

Figure 3.1. A Schematic Illustration for Preparation of the Optical DNA Hybridization Sensor and the Operational Principle

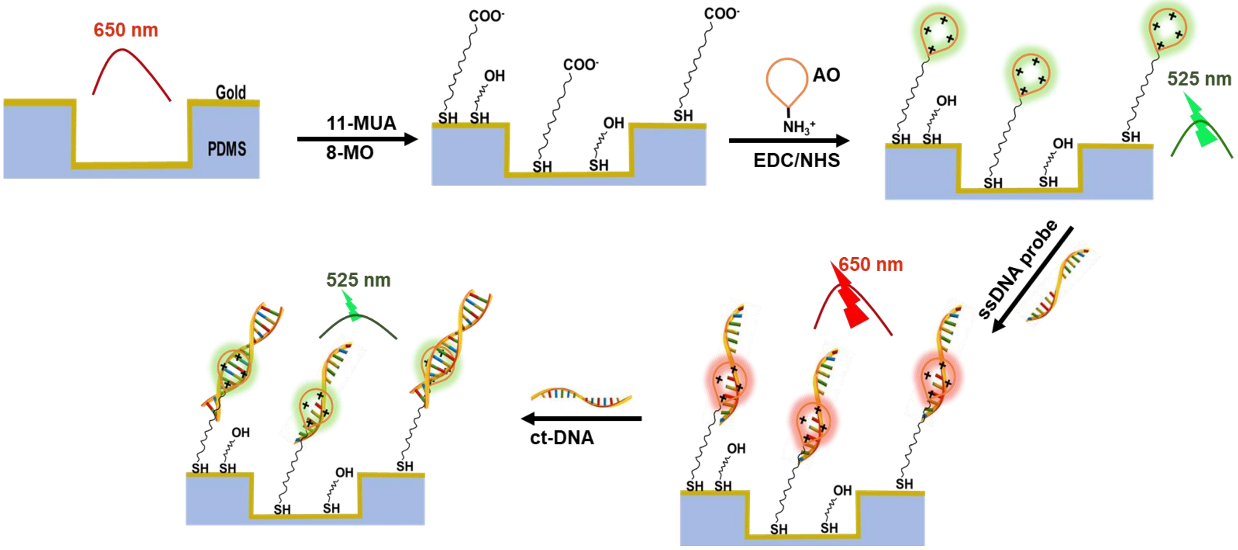

Results and Discussion

Reversal Nanoimprint to Produce Nanoslit Array Structures

Electron beam lithography (EBL) is one of the go-to techniques because it provides highly precise structure in nanoscale dimensions. However, being a direct-writing technique makes it a slow and time-consuming process which is not suitable for mass fabrication. The nanoimprinting technique using a PDMS replication process was proved to be a simple and easy control process for low-cost and volume generation of reproducible nanostructured arrays.[53] The reversal nanoimprint method in this report was optimized to obtain a uniform and reproducible nanoslit array structure (see Scheme S1a Appendix A). In the process, PDMS was cured on the surface of a Si substrate containing an array of nanoslit structures created by using a patterned Si template to produce a negative nanostructure on the PDMS. After pouring PDMS atop Si nanostructures, the curing temperature was maintained at the optimal temperature 75 ^{o}C for 1 h to provide a smooth and reproducible transfer of the nanoslit array to the PDMS. The limitations of this method include challenges associated with the high viscosity of PDMS which makes it difficult to diffuse into smaller nanoscale patterns fabricated on the template. The patterns may thus suffer from low aspect ratios and deformations at different temperatures (Scheme S1b Appendix A). The deformed nanostructure transfer could occur at a higher baking temperature of 100°C after 1 hour because the PDMS solution solidifies too quickly without giving sufficient time for the solution to flow into the nanoslit. Under 55 °C, peeling the PDMS off the Si wafer is difficult because the PDMS is not fully cured and easily breaks off. Figure 3.2 shows the design of the nanoslit array and an SEM image of a uniformly imprinted nanoslit array structure. The nanoslits are ~70 nm wide (w), with 300 nm pitch (p) and 150 nm deep (h), and a deposited gold film of 35 nm thick measured using a crystal quartz microbalance. By changing the deposited gold film thickness, we obtained a series of nanoslit arrays of a variety of slit width at 55.38, 73.6, 90.1, 115.2, and 135 nm. The slit width decreases with increasing gold film thickness (Figure S1 Appendix A).

Figure 3.2. (A) Schematic Illustration of the Nanoslit Array Design (Not in Real Geometric Ratio) and (B) A Representative SEM of a Gold Film Nanoslit Array Fabricated on a PDMS Slab

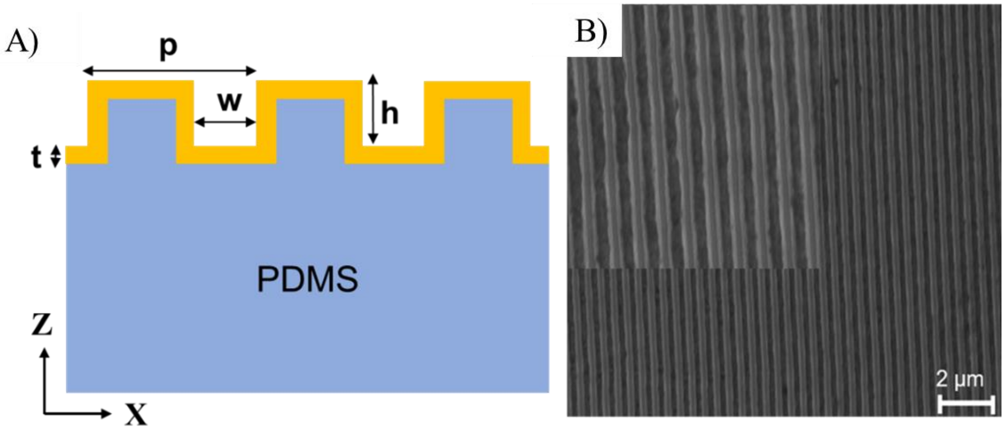

Optical Properties of the Nanoslit Arrays

We use both finite-difference time-domain algorithm (FDTD solutions, Lumerical) simulation and experimental measurements of the light reflection at the nanoslit arrays to investigate the SPR effect on the optical properties. Additionally, a validated method based on semi-analytical modeling was used to quantitatively account for the scattering, launching, and propagation of surface plasmon at the nanostructure interfaces. First, the optical responses of the nanoslit without or with Au-base at the slit bottom were simulated with a plain light excitation in reflection mode for a variety of nanoslit widths (w). Figure S2, Appendix A shows the representative cross-sectional renderings of electric field intensity ($|E|^2 = E_x^2 + E_z^2$) distribution in the xz-plane. The color bar indicates the magnitude of E-field intensity at various regions of the slit. For nanoslit of widths 70 nm, 90 nm, 110 nm, and 130 nm (corresponding to the Au layer thickness of 45, 35, 25, 15, and 5 nm) obtained by the FDTD simulations, the maximum field recorded at the hot spots is 8.08 eV, 6.97 eV, 6.96 eV, and 5.46 eV respectively. These ‘hot spots’ are located at the entrance edge and bottom corners of the nanoslit structures. They represent a cumulative effect of incident light coupling with localized surface plasmon modes[54] as well as from surface plasmons polaritons propagating on the top, bottom, and side walls of the nanoslit which terminates at the edges of the nanoslit causing the formation of a localized electric field.[55] The magnitude of these localized fields decreases with an increase in slit width. The |E|-field with a decay length of tens of nanometers located at the top and bottom edges of the nanoslit at the Au/air interface indicates the excitation of LSPR. On the other hand, a SPP mode with a longer decay length at the Au/PDMS interface is also visible. The field distribution evidently reveals the co-existence of both SPP and LSPR modes at these “hot spots” regions.[34]

Figure 3.3. (A) FDTD Reflectance Spectra at Different Nanoslit Widths (B) Extracted Reflection Spectra from Cytoviva Hyperspectral Imaging Measurements

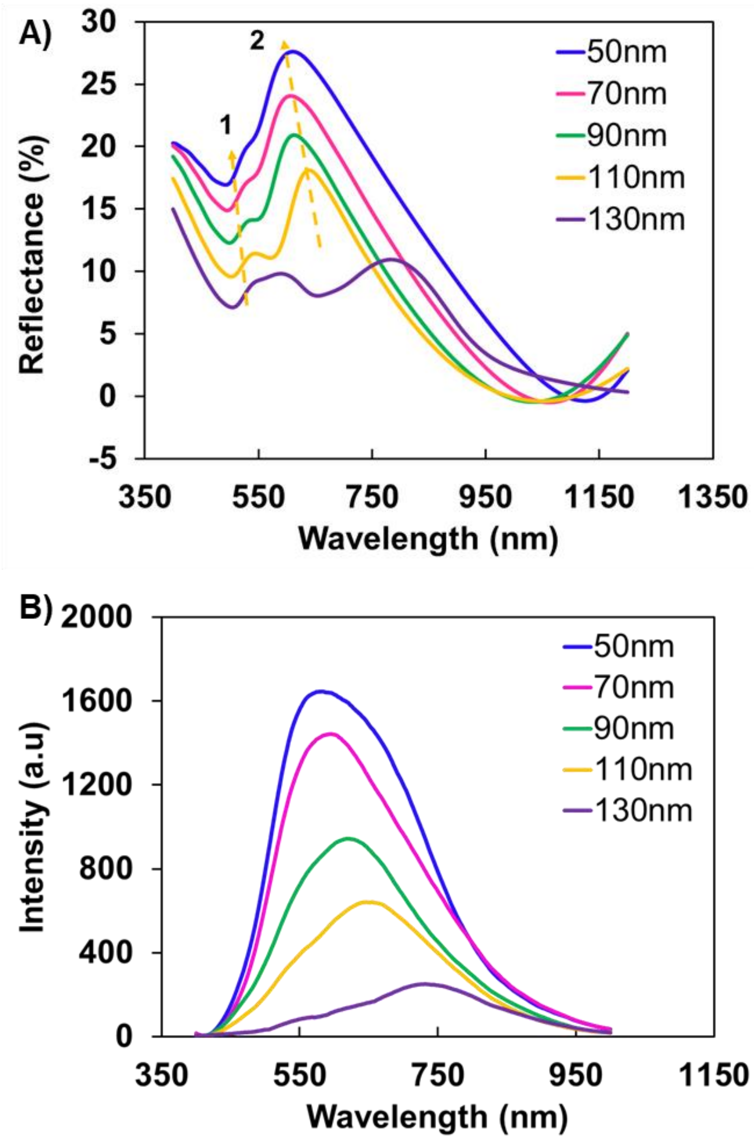

In experimental measurement, unpolarized plain light (broadband) from a halogen lamp was used as incident light to illuminate the nanoslit samples from the top. The reflecting light signal captured by a 10x objective lens (NA=0.3) is then collected using the darkfield Cytoviva hyperspectral imaging system. Figure 3.3 presents the reflection spectra of the nanoslit arrays at different slit widths from both the FDTD simulation and experimental measurements. Figure 3.3A shows the relative reflectance of the calculated results and Figure 3.3B is the extracted reflection spectra from the hyperspectral images. The relative intensity change, and peak position provide corroborative information of the nanoslit array optical property and the dependence on the nanoslit width. Specifically, at nanoslit widths of 50 nm, 70 nm, 90 nm, 110 nm, and 130 nm, the primary resonant peak position is changed from 609, 615, 621, 649, to 755 nm obtained from simulation while experimental peak positions obtained at 585, 590, 620, 655 and 738 nm correspond to the nanoslit width of actual samples measured to be 55.38, 73.6, 90.1, 115.2, and 135 nm. The results indicate a good agreement of the simulation and experimental results. The slight difference between the simulated and experimental peak positions may be due to the imperfection of nanoslits during pattern fabrication and the small deviation of the actual nanoslit widths from the simulation. This is expected because the slit width determines the composition of polariton states.[30] The simulation shows two reflectance peaks (1 and 2) which may be assigned two different plasmonic modes SPP and LSPR.[34] The experimental reflection spectra represent the combined modes but are dominated by the primary plasmonic peak 2. One can see that the resonance peak redshifts with respect to an increase in slit width with the decrease of the field intensity. The ability to tune resonant wavelength position is particularly important in investigating light-matter interaction where the absorbing material can be excited at a specific wavelength. In brief, the simulation and experimental results validate the geometry dependence for the plasmonic resonance of the nanoimprinted gold nanoslit arrays at the PDMS substrates.

To further understand the relationship of surface plasmon to the optical enhancement, we applied a previously reported semi-analytical mode to calculate the surface plasmon generation efficiency (SPGE) for different nanoslit widths (see details in SI).[56] Figure S3 Appendix A shows a correlation between the SPGE and EM-field obtained in FDTD and experiments from the Cytoviva hyperspectral imaging. In the nanoslit array, its SPGE approximately has the same dependence as the EM field at the NS surface on the nanoslit width. The correlation of the SPGE and optical field intensities with respect to the geometric parameters provides us a guide for the development of advanced optical devices.

Optical Enhancements of Dye Molecules on the Gold Nanoslit Arrays at PDMS Substrate

In this study, the optical enhancement of dye molecules at the nanoslit array substrates was examined. In contrast to previous work where the bottom of the nanoslit is a non-metallic component,[32-33] here, the in-slit bottom is designed to contain a thin film of Au (Figure 3.2). This configuration creates an extra metal-dielectric interface which provides an additional interface for SPP excitation for improved interaction with excitons and offers an avenue for plasmonic manipulation.[20] Additionally, the in-slit Au bottom system was chosen because it supports broadband resonance reflection, which is expected to provide efficient excitation and emission of PL (Figure 3.3B). The emission quenching that typically occurs when emitters are in close or direct contact with metals is prevented here since the dyes are sandwiched between the high electric fields generated by the adjacent walls and the bottom of the nanoslit.[33] There are other approaches that attempt to provide optical enhancement due to plasmon-exciton coupling in nanostructures, such as core-shell nanoparticles or nano-cone cavities.[57-59] Nevertheless, there is a need to have a better understanding of the underlying reaction mechanism of different nanostructure designs thus improving the optical signal enhancement. To address the need, we investigated the impact of excitation and emission wavelength of fluorophores with excited plasmons in the nanoslit array.

To determine the excitation/emission wavelength requirement necessary for optimum coupling of a fluorescence molecule within the plasmonic fields, a dye-Au nanoslit hybrid system was constructed (see method section) and the resulting optical field enhancement responses were quantified. The intensity and position of SPP resonances from the reflection spectra of the patterned samples and references containing AO, PI, and DHE were measured using the Cytoviva hyperspectral imaging system. Figure S4 Appendix A show representative net intensity spectra measured for AO, PI, and DHE in the absence of nanoslit (black dotted line) and in nanoslit of different widths. The net reflection spectra were obtained by subtracting the background without dye. It is assumed here that the plain light source at normal incidence to the nanopattern excites plasmons $\lambda_{\boldsymbol{p}}$ which then interact with the excitation and/or emission of the dye molecules. The measured reflectance thus represents a joint contribution of the processes of plasmon evanescence, light scattering, and the fluorescence emission of the dye. To investigate how the net reflectance intensity is controlled by these processes in the nanohybrid structure, we investigate the relationship of reflectance to the plasmon-absorbance match ($\Delta\lambda_{\mathbf{1}} = \left|\lambda_{\boldsymbol{p}} - \lambda_{\boldsymbol{abs}}\right|$) referred to as excitation enhancement and the plasmon-emission match ($\Delta\lambda_{\mathbf{2}} = \left|\lambda_{\boldsymbol{p}} - \lambda_{\boldsymbol{em}}\right|$) referred to as the emission enhancement. The smaller $\Delta\lambda$ represents the more spectral overlap of plasmon resonances with molecular absorption or emission resonances. Figure S5 Appendix A shows the normalized optical reflectivity of the device together with the absorption and emission features of AO, PI, and DHE. For AO, the $\Delta\lambda_{\mathbf{1}}$ increases from 103 nm to 243 nm and $\Delta\lambda_{\mathbf{2}}$ from 62 nm to 202 nm as the slit width increases from 50 nm to 130 nm respectively. A similar trend is observed for DHE showing $\Delta\lambda_{\mathbf{1}}$ and $\Delta\lambda_{\mathbf{2}}$ increase from 238 nm to 378nm and from 170 nm to 310 nm. PI displayed $\Delta\lambda_{\mathbf{1}}$ from 148 nm to 288 nm and a very strong plasmon-emission overlap with the $\Delta\lambda_{\mathbf{2}}$ ranging from 3 nm to 108 nm in the different nanoslit widths. Overall, AO shows a better excitation overlap (smallest $\Delta\lambda_{\mathbf{1}}$) in all nanoslit structures whereas PI exhibits the best plasmon-emission overlap (smallest $\Delta\lambda_{\mathbf{2}}$). It is therefore convenient to assume that any modification in the optical characteristic of AO and PI by the plasmon band occurs via plasmon-absorption or plasmon-emission interaction or both. DHE shows very wide $\Delta\lambda_1$ values and the plasmon-absorbance spectra do not overlap at all.

The impact of these overlaps on the reflectance intensity enhancement factor (INF) $\boldsymbol{I_E}$ in different slit width nanostructures was obtained by normalizing the overall measured reflectance with that of the un-patterned area as a reference using Eq. 1.[60]

$$I_E = \frac{I_{pd} - I_p}{I_{cd} - I_c} \qquad (1)$$

where $I_{pd}, I_p, I_{cd}, and\ I_c$ are the measured peak intensities of nanoslit arrays with dye and without dye, and an unpatterned area with dye and without dye, respectively. As summarized in Table 3.1**,** the magnitude of I_E show dependence on the position of the plasmon band relative to molecular resonances. Typically, the I_E for AO, PI, and DHE in the different nanoslit width systems is diminished as the mismatch ($\Delta\boldsymbol{\lambda_1}$ or $\Delta\boldsymbol{\lambda_2}$) between the plasmon band and the molecular resonances of the fluorophores becomes larger. For example, AO in the 50 nm slit showed the highest I_E (56.92-fold) which decrease sharply to 4.72-fold in a W=130 nm structure. The decrease in I_E could be caused by either the decrease in the electromagnetic field intensity in the different nanoslit structures **(**Figure 3.3**)** or a plasmon-molecular resonance mismatch. To verify which effect is at play, we quantified and compared the percentage change in intensity of the different width's nanostructures relative to the 50 nm structure without and with molecular dyes. The percentage change in intensity, ΔI is calculated using the equation.[61]

$$\Delta I = \frac{I_{50} - I_x}{(I_{50} + I_x)/2}\ X\ 100 \qquad (2)$$

where I_{50} is the maximum peak intensity in the 50 nm structure and I_x, the maximum peak intensity in the other nanostructures. The ΔI shows the value in percentage by which the intensity is changing as the slit width is increased from 50 nm to 130 nm. Relative to the 50 nm slit width structure without a molecular dye, the 70, 90, 110, and 130 nm width structures show a decrease in intensity by 13%, 53%, 87%, and 147% respectively **(**Table S1 Appendix A**)**.

With AO coupled to the nanostructures, the intensity decreased by 16%, 102%, 137%, and 165% respectively. By comparing the percentage change in intensity without and with AO dye for each nanostructure, we see a positive increase in the presence of AO. For example, the ΔI in 70 nm structure without dye, minus the ΔI in 70 nm structure with dye is 2%. This kind of difference, which is observed in all the nanostructures, is ascribed to the spectral mismatch effect. Therefore, the corresponding increase in the intensity enhancement factor for AO (Table S1b) as slit width decreases shows the dependence of the $\boldsymbol{I_E}$ on the interplay between the excitation/excited state of the dye and the SPR.[62]

The low optical enhancement in the DHE system relative to AO and PI (see Table 3.1) is due to a large mismatch of the plasmon resonant peaks from DHE's absorption and emission wavelengths. Since the spectral overlap of the fluorophore with plasmon resonance is responsible for the coupled system emitting a photon, a highly mismatched system probably leads to reabsorption of energy and dissipating it as heat.[63]

For PI in the 90 nm slit width, the optical enhancement is 30-fold which is more than the enhancement in all PI-hybrid systems including 50 nm and 70 nm width nanostructures. The observation can be traced back to the strong plasmon-molecular emission spectral overlap ($\Delta\lambda_{\mathbf{2}}$ =3 nm) in W=90 nm which compensated for the relatively lower field in 90 nm slit width compared to 50 nm and 70 nm slit width structures. It can be inferred that the $\boldsymbol{I_E}$ in the PI hybrid system is mainly controlled by plasmon resonance with emission. The higher $\boldsymbol{I_E}$ (56.92-fold) in the AO system relative to the PI system (24.42-fold) may be attributed to the close absorption and emission spectral overlap between plasmon and molecular resonances. In brief, these findings demonstrate that plasmon-exciton spectral overlap is highly critical for optical signal enhancement in this type of plasmon-exciton hybrid system.[20, 30, 64] The observed behavior indicates an interplay of both excitation and emission enhancements induced by the plasmon mode in Au nanoslit.

Table 3.1. Optical Intensity Enhancement and Spectral Mismatch Between Plasmon and Molecular Resonances in Different Width Structure Containing AO, DHE and PI

	Abs/em-plasmon mismatch (AO)		Abs/em-plasmon mismatch (PI)		Abs/em-plasmon mismatch (DHE)		Intensity enhancement $I_E = \frac{I_{pd} - I_p}{I_{cd} - I_c}$		
W (nm)	$\Delta\lambda_1$(nm)	$\Delta\lambda_2$(nm)	$\Delta\lambda_1$(nm)	$\Delta\lambda_2$(nm)	$\Delta\lambda_1$(nm)	$\Delta\lambda_2$(nm)	**AO**	**PI**	**DHE**
50	103	62	148	32	238	170	56.92	24.42	1.94
70	103	62	148	32	238	170	48.25	24.12	1.32
90	132	91	177	3	267	199	15.43	30.01	0.06
110	167	126	212	32	302	234	7.97	22.28	0.02
130	243	202	288	108	378	310	4.72	2.29	0.01

DNA Assay

Acridine orange was chosen for this assay because of its above observed superior optical enhancement in the nanoslit. The cationic property of amino modified acridine offers a suitable basis for DNA probe assembly. Negatively charged ssDNA was introduced to 9-aminoacridine which was cross-linked via EDC/NHS to the gold nanoslit array at a PDMS substrate to generate signals corresponding to targets. The assembly was induced by electrostatic interaction between ssDNA and AO (see method section). In order to obtain signals that will discriminate between ssDNA and dsDNA, it is necessary to select a plasmon resonance whose wavelength position overlaps well with the emission of AO-ssDNA or AO-dsDNA (Figure S5 Appendix A). We chose emission overlap because of its overwhelming effect at increasing the rate of radiative recombination of the exciton state. Excitation overlap on the other hand could increase the population of excited states but a portion of it could undergo non-radiative loss to generate heat that might affect biological analyte. Hence, we selected a 110 nm structure whose resonance wavelength position at peak λ=655 nm is close to the emission resonance of the AO-ssDNA complex (λ=650) and more mismatched with the AO-dsDNA complex.

Figure S6A Appendix A shows that the introduction of ssDNA to acridine in the nanostructure resulted in the further enhancement of the optical field previously recorded for acridine alone in the nanoslit structure (black vs. blue curve). In the presence of a complementary target DNA (ct-DNA), the intensity drops back down (red curve) due to the hybridized dsDNA. This behavior offers a discriminatory approach to the detection of ssDNA and a hybridized dsDNA.

In order to ensure that the optical signal changes are not due to direct interaction of free or unreacted DNA probe or target with plasmons in the nanoslit or via nonspecific binding, we carried out a separate experiment where ssDNA (without AO) is incubated with the Au nanoslit that has been previously modified with SAM of 11-mercaptoundecanoic acid and 8-mercaptooctanol. As expected, Figure S6B shows that the plasmon field intensity does not show any significant change proving that there is no interaction between DNA and the nanolist surface, confirming the important interplay role of the AO dye with the DNA and nanoslit plasmon for optical signal differentiation.

Acridine orange is not specific or selective to the ssDNA. This means that the capture ssDNA probe can bind to AO, and the target DNA can also bind to AO to cause an unspecific binding signal, respectively. To prevent this, it is necessary to determine the minimum equilibrium ssDNA concentration where AO active surface is no longer receptive to binding DNAs. Figure 3.4 shows the spectral peak variation and calibration curves obtained for the interaction of AO with different concentrations of the capture ssDNA and the target ct-DNA molecule. Figure 3.4A exhibits a gradual increase in the intensity of AO-plasmon spectra as the concentration of ssDNA is increased from 1 nM to 22 μM. Little intensity fluctuation is noticed above 22 μM, suggesting saturation of the ssDNA binding at the AO surfaces. For this reason, a concentration of 22 μM or larger ssDNA probes was used for the preparation of sensor substrates in subsequent experiments. The consequent effect of using below-equilibrium point concentration (less than 22 μM) of ssDNA probe on AO is shown in Figure S7 Appendix A. The addition of 4 nM of ct-DNA to the AO-ssDNA substrate made from 4 μM ssDNA capture molecule resulted in optical signal intensity enhancement due to the direct interaction of ct-DNA with only partially ss-DNA saturated AO.

Further, it was found that the optical signal depends on the concentration of ssDNA in two different regimes. Figure 3.4B show linear relationships between optical changes and the concentration of ssDNA. At a high concentration regime, AO and ssDNA interact much more rapidly via dye-base stacking to form the AO-ssDNA complex.[50]

Figure 3.4. Interaction of DNAs with AO in the 100 nm Nanoslit Arrays. (A) Field Intensity Spectra with Different Concentrations of ssDNA. (B) Plot of I/Io Versus the Log Concentrations of ssDNA. Note that I and Io are Intensities of AO in Nanostructure Before or After Adding ssDNA (C) Field Intensity Spectra of AO-ssDNA with Different Concentrations of Complementary Target DNA (ct-DNA). (D) Plot of I/Io Versus the Logarithm Concentrations of ct-DNA

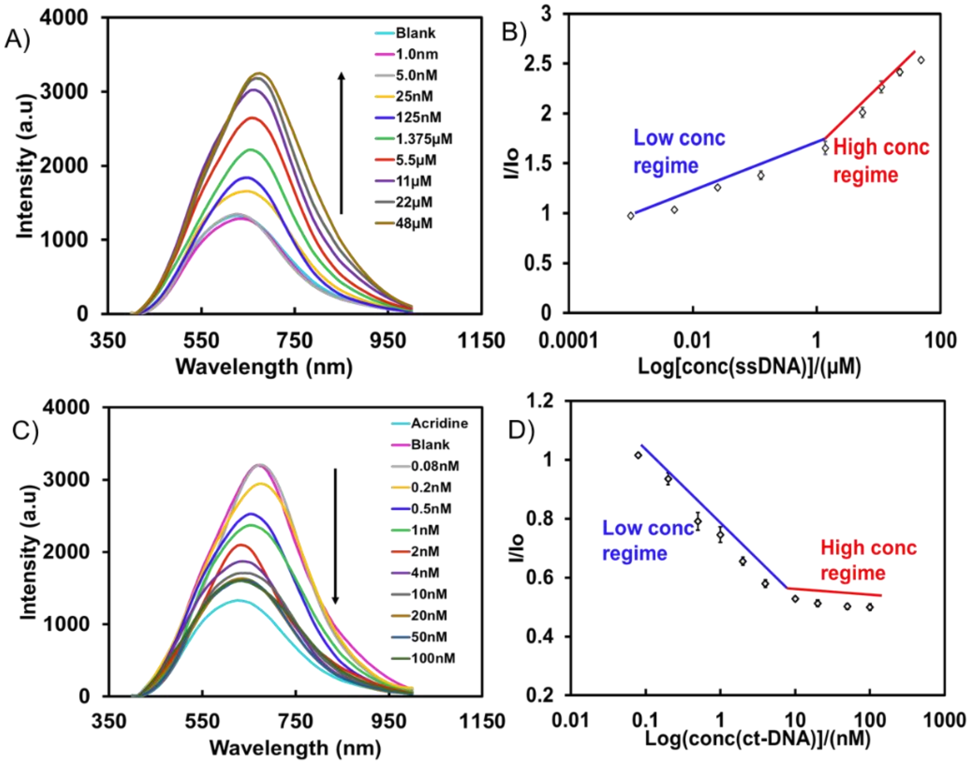

Next, considering the specific interactions between ssDNA and its complementary counterpart, we tested the optical signal transduction mechanism due to the optical signal differences of AO-ssDNA interaction and DNA hybridization. We took advantage of the phenomenon of field enhancement and introduced the ct-DNA to the AO-ssDNA complex. Figure 3.4C shows the optical signal quenching with the addition of ct-DNA up to 100 nM until no further diminish in the signal intensity is observed. The calibration curve for ct-DNA detection was determined based on serial concentrations of the ct-DNA at 0.08, 0.1, 0.2, 0.3, 0.5, 1.0, 2.0, 4.0, 10.0, 20.0, 50, and 100 nM. Figures 3.4D plots the relative signal intensity increase (I/I_o) versus the logarithm value of the ct-DNA concentration which displays two linear ranges consisting of 0.08 nM to 10 nM (R^2=0.994) and 20 nM to 100 nM, respectively. The limit of detection (LOD) was evaluated based on the relation, $LOD = 3\sigma/S$, where σ is the standard deviation of the blank signal and S is the slope of the calibration plot. [21] The LOD was found to be 0.21 nM at a signal-to-noise ratio of 3 in the linear range of the low-concentration regime. The low concentration range relatively shows a rapid decline in intensity which slows down and reaches a steady state at higher concentrations. This is because, at low concentrations, free monomers ssDNA start hybridizing with ct-DNAs to form dimers nearly instantaneously with a faster reaction rate.[65] As free monomers become depleted due to hybridization with ct-DNA, further increases in ct-DNA concentration produce a smaller intensity response until there is no detectable signal change. At the concentration (100 nM), the ssDNA is in equilibrium with the ct-DNA. Thus the difference in linearity between the low-concentration regime (0.08 nM to 10 nM) and the high-concentration regime (20 nM to 100 nM) arises from a decrease in binding kinetics that occurs at a concentration above 10 nM.[66-67] The linear range and the low LOD shown here demonstrate that our proposed approach may meet the sensitivity requirement for DNA hybridization assay. A detailed comparison of this work with other SARS-CoV-2 biosensors using different methods is presented in Table S2 Appendix A. The LOD and detection time of this work is superior or competitive to recently reported results.

In addition to the hyperspectral signal study, we further examined fluorescence changes by using an Axio Z2M imaging microscope at 475 nm excitation. Figure 3.5A shows the fluorescence images of AO-ssDNA probe substrates in the presence of ct-DNA at different concentrations. It can be visualized that at higher concentrations of ct-DNA, fluorescence intensity decreased. Note that the emission from the AO-ssDNA probe (at a peak around 650 nm) is blocked by a 546 nm cut-off filter. From the greyscale images in Figure 3.5A, the fluorescence intensities corresponding to the concentrations of the ct-DNA were obtained. Figure 3.5B displays a linear dependence of fluorescence intensity on the logarithm value of the ct-DNA concentration in a range of 0.08 to 200 nM, a good agreement with net reflectance intensity as a function of the ct-DNA concentration (Figure 3.4D). The error bars convey the average fluorescence signal over a 25 min period after reaction equilibrium is reached.

Figure 3.5. Fluorescence Images at Different Concentration of ct-DNA in Nanoslit Arrays. (A) Shows the Images Taken Using a 475 nm Excitation Light Source and a 546 nm Cut Off Filter. Note that on the Right Side are the Images When Converted to Gray-Scale; (B) A Graphic Plot Showing the Fluorescence Intensity as a Function to the ct-DNA Concentration Ranging from 0.08-200 nM

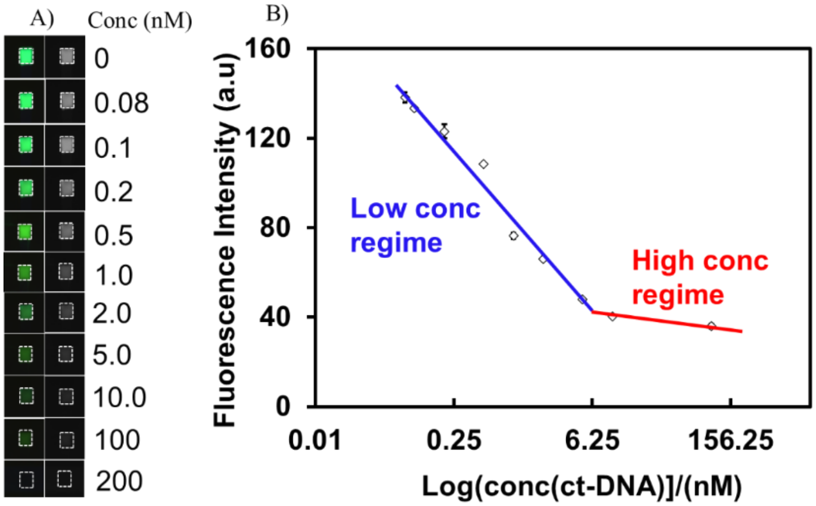

By using non-complementary target DNAs as control experiments, the specificity of the assay was investigated using 1-, 2-, 3-mismatched, and all mismatched DNA samples, respectively. Figure 3.6 shows the relative fluorescence intensity changes of perfectly matched ct-DNA as a comparison to the mismatches for both 1 nM and 20 nM concentrations. The results indicate a satisfactory selectivity by providing significant signal change to differentiate even one base mismatch. Figure S8 shows the fluorescence images of AO and AO-ssDNA in the absence and presence of ct-DNA on PDMS substrate without nanostructure and their red, green, and blue (R, G, B) intensity profile. The color of the fluorescence images changes from green for AO to red (for AO-ssDNA) and finally back to green after hybridization with ct-DNA. This means that the decline in resonance intensity peak due to the ct-DNA hybridization with the probe DNAs occurs because the emissive capability of the acridine-dsDNA complex in the nanoslit structure is shifted significantly to the green region which is away from plasmon resonance. This tends to weaken the coupling effect of the dye with resonating plasmons generated in the nanoslit arrays.

Figure 3.6. Normalized Fluorescence Upon Addition of 1 nM and 20 nM Perfectly Matched DNA with Different Mismatched Bases

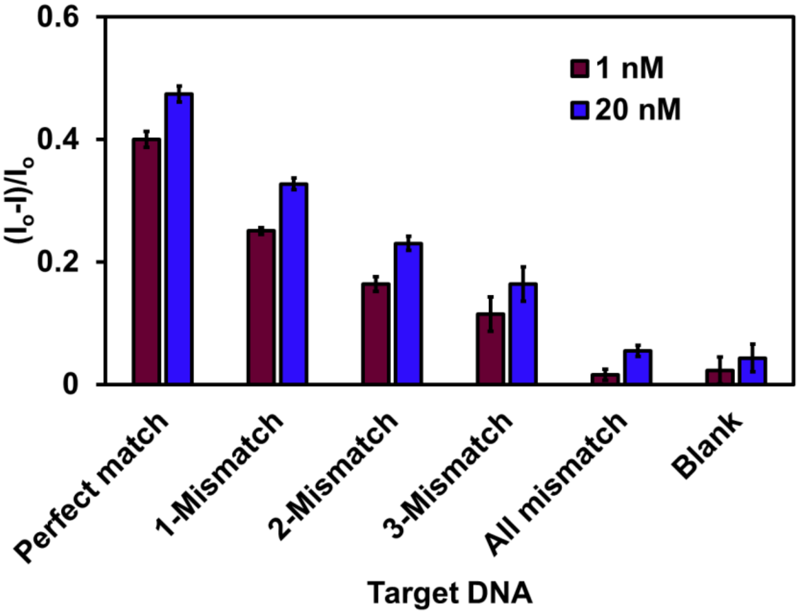

Stability and Reusability of the Sensor

In addition to sensitivity requirements, high stability is crucial to enable easy storage and deployment of the biosensor without necessarily compromising its integrity for precise sample detection. To evaluate the stability, the sensor device was kept at room temperature for up to 10 days and the optical response of the sensing system was monitored before and after hybridization with 0.5 nM ct-DNA. Figure S9A indicates that the hybridization signal intensity on the first day is consistent with the one observed after 10 days. In addition, we performed the regeneration of the sensor surface after hybridization, Figure S9B demonstrates the reusability of the sensor after hybridization. Notably, the active probe surface sustains 2 successive assays after repeating the regeneration without any significant loss of performance as indicated by the recovered signal intensity of the probe. After the second regeneration cycle, there is a noticeable increase in the hybridization signal intensity which suggests an incomplete DNA interaction. This occurrence may be due to the weakening of the DNA binding affinity, resulting from the multiple heating and cooling which presumably affects the stability of the probe monolayer, thus a slight change of the density of AO-ssDNA. However, the regeneration of the probe allows for the sensor to be reused 6 times with a mean recovery of 96.54% of the original signal. This proves that the fabricated nanoslit array sensor is not only stable but reusable without necessarily repeating the surface functionalization step.

Herein, the principle of this work for the detection of DNA hybridization at the flexible plasmonic nanoslit array substrates was validated and demonstrated. The metachromatic property of acridine dye was employed for the quantification of nucleic acid hybridization in a plasmonic environment. As shown in Figure 3.1, the overall strategy and mechanism lead to the discrimination of ssDNA and dsDNA at the nanoslit sensing area in optical responses. Initially, ssDNA is saturated onto the cationic acridine-modified surfaces via electrostatic interactions causing the emission wavelength of acridine to shift from 525nm to 650 nm which matches the plasmon resonance. Such a plasmon-exciton coupling effect causes significant optical field enhancement and signal amplification. The addition of ct-DNA to this substrate diminishes the optical signal in the nanoslit structure in the measured reflective hyperspectral and fluorescence images. This occurs because the hybridization of the capture DNA probes with the ct-DNAs forms a dsDNA and causes the emission wavelength shift of the AO-DNA complex from 650 nm to 525 nm which is away from plasmonic resonance energy, thereby reducing the plasmon-exciton coupling effect. The increase of optical signal in the presence of ssDNA and the signal decrease in the presence of ct-DNA upon hybridization provides the highly responsive sensing capability of the device. This work demonstrates a significant improvement in signal amplification using a well-designed plasmon-exciton coupling system for the development of a highly sensitive device for detecting DNA hybridization and binding studies.

Conclusion

In summary, we have used both computational modeling/simulation and a simple nanoimprinting technique for developing plasmonic nanoslit arrays at a flexible PDMS substrate and demonstrated plasmon-exciton coupling effect on surface-modified dye for optical enhancement and DNA hybridization detection and its capability to differentiate single base mismatch. The reported nanoimprinting fabrication process for hybrid nanostructured arrays based on gold-coated PDMS renders the generation of various geometries and nanoslit sizes by controlling the thickness of the Au layer without the need for expensive or sophisticated patterning instruments. The plasmonic resonance peak wavelength of the nanoslit arrays was tunable by varying the nanoslit width from 50 nm to 130 nm. The coupling of the plasmonic field with a molecular exciton was found to boost the optical signal of dye molecules attached to the nanoslit surfaces when the excitation and emission energy of the molecule matches well with plasmon resonance energy with different dye molecules. The 50 nm plasmon slit array with an AO exciton hybrid system showed maximum optical field enhancement of 57-fold and was used to monitor DNA-DNA hybridization based on the different emission wavelengths of the AO-ssDNA and AO-dsDNA systems upon hybridization. The device was evaluated using 1, 2, or 3 base mismatches in the detection of DNA hybridization which showed significant signal differentiation for high sensitivity and specificity and the LOD of 0.21 nM ct-DNA for perfect matched DNA hybridization. It also demonstrated high stability and can be reused 6 times with about 96% signal recovery. This contribution that provides a model of sensing applications by using metachromatic fluorescence dyes of plasmonic signal amplification for DNA detection will further stimulate broader applications of the sensing method in clinical determinations and biological analysis. It was found that the in-nanoslit Au film played a key role in localized field enhancement thus the amplification of the optical signal for sensing application. Owing to the simple fabrication and functionalization approach, such a plasmon-exciton coupling method will play a significant role in developing next-generation optical sensors.

Experimental Section

Chemicals and materials. Dihydroethidium (90% purity, Cat. No. D11347), propidium iodide (94% purity, Cat. No. BMS500PI), phosphate buffered saline buffer (PBS, 10mM PB, 150 mM NaCl, pH 7.4, Cat. No. 003002), Polydimethylsiloxane prepolymer (Dow Coning Sylgard 184), and absolute ethanol (Cat. No. T038181000) were purchased from Thermofisher scientific. Acridine orange dye (Cat No. 10127-02-03), 11-mercaptoundecanoic acid (11-MUA, 95% purity, Cat. No. 450561), 8-mercapto-octanol (8-MA, 95% purity, Cat. No. 075075), 1-ethyle-3-(3-dimethylaminopropyl) carbodiimide hydrochloride (EDC, 99% purity, Cat. No. 03449), N-hydroxysuccinimide (NHS, 98% purity, Cat. No. 130672), perfluorinated trichlorosilane (97% purity, Cat. No. 448931) were purchased from Sigma-Aldrich). Silicon mold from II-VI Aerospace & defense, gold (99.99% purity, Cat. No. EVMAUXX) and Titanium (99.99% purity, Cat. No. EVMTI45EXE-J) were obtained from Kurt J. Lesker. Table 2 the HPLC purified oligonucleotides probe and targets that were obtained from Integrated DNA technologies. All chemicals and materials were used as supplied without any modifications.

Instrument and equipment. The excitation and emission/fluorescence spectra of numerous solutions were obtained on a Varian Cary eclipse fluorescence spectrophotometer (Agilant, USA). SEM images were taken on a Field-emission scanning electron microscope (Carl Zeiss Auriga). Plasmonic field reflection spectral measurements were done on a Cytoviva hyperspectral microscope**.** Fluorescence images were captured with Axio Z2M (Zeiss) microscope equipped with excitation filters of 395-410nm and 490-505nm using 20X objective lens at 5.0 s exposure time. Other instruments used includes Plasma Cleaner (South Bay Technologies PC2000), e-beam evaporation (Kurt Lesker PVD75 e-beam evaporator), UV/ozone Pro cleaner, and LSE-WS Stokes WAFERSKAN ellipsometer.

Fabrication procedure. The fabrication process is schematically depicted in Scheme S1 Appendix A. Briefly, a moulding soft lithography is performed on a Si template consisting of a nanoslit array to produce a negative pattern of the Si template on PDMS. This is achieved by curing and careful peeling of PDMS off the Si template**.** Finally, a deposit of thin metal film of desired thickness was made on the top surface of the PDMS mould by electronic beam evaporation.

Pattern Transfer of Periodic Si Nanoslit Array. Patterned Si wafer was used as a master mold used to transfer a periodic nanoslit array onto a flexible PDMS (Figure S1 Appendix A). The Si wafer has a nanoslit array of periodicity and slit depth of 300 nm and 150 nm respectively. The surface of the silicon wafer was salinized to ensure easy peeling of cured PDMS. Briefly, 1 mL of perfluorinated trichlorosilane in an aluminum dish was put into a desiccator alongside the patterned wafer held by a scotch tape in a petri-dish. The desiccator was pumped down for 6 min and the pump was turned off. The wafer was allowed to stand in the desiccator for 6 hours. Meanwhile, the PDMS for pattern transfer was obtained by mixing a 10:1 weight ratio of the polymer base and cross-linking agent (curing) at room temperature. The mixture was degassed in a desiccator using a rotary pump. The bubble-free PDMS mixture was then poured onto the patterned Si wafer and baked in an oven for 1h at 75°C followed by cooling. Finally, the dried sample was peeled to obtain a patterned PDMS substrate.

Gold Deposition on the Patterned PDMS Substrate. The PDMS was first treated with oxygen plasma (power density, 20mW/cm^2; pressure, 100mTorr; O_2 flow, 10sccm; Ar flow 40 sccm; exposure time 5s) to enhance metallic adhesion onto the surface. The PDMS template, physically supported on the back of a watch glass (60 mm diameter, 2 mm thick, 6 mm depth) was coated first with 5 nm titanium, then with gold via e-beam evaporation at the rate of 1.6 Å/s to the desired thickness at a vacuum pressure of 8.2×10^{-6} Torr. The thickness was monitored and measured using quartz crystal microbalance (QCM). To improve the uniformity of the deposited Au material, the sample plate was rotated throughout the deposition process. The thickness of the deposited gold was further verified using an ellipsometer.

Preparation of Dye Modified Au Nanoslit. Three different dyes (Acridine orange, propidium iodide, dihydroethidium) having different optical properties were each prepared to a concentration of 0.5mM. Next, the nanoslit-cavity devices were cleaned by 15 min exposure to UV/ozone. Then, 50 µl of each dye was drop-coated onto gold nanoslit array. The dye was allowed to dry in a dark environment and was immediately used for optical studies. The fluorescence images before and after dye coating (Figure S2 Appendix A) expressed dye modification of the Au surface.

Preparation of Immobilized AO onto the Gold Nanoslit Array. First, gold coated PDMS chips with nanoslit arrays were cleaned with O_2 plasma for 10 min. Next, a self-assembled monolayer (SAM) was created on the surface of the PDMS arrayed chips by incubating it in a

1:2 mole ratio of 11-MUA, and 8-MA, in an absolute ethanol solution for 24 hours. The carboxylic functional groups of the SAM were then activated by incubating the chips in a 0.5 mM EDC/NHS for 2 h. The chips were then rinsed with DI water and immediately submerged in 5 mL solution of freshly prepared 20 µM amino modified AO in aqueous PBS for 2 h. The chips were rinsed with DI water, dried, and kept in a dark cupboard before the next experiment.

Preparation of AO-ssDNA probe in a Gold Nanoslit Array. The ssDNA solution was prepared by resuspending the lyophilized powder of DNA oligo (101.7 nmol) in a 1.017 mL of 0.1 mM PBS (pH 7.4) to obtain a 100 µM stock. From the stock, further dilutions were made to obtain the desired concentration. 100 µl aliquot of ssDNA of desired concentration (1.0 nM, 5 nM, 25 nM, 125 nM, 1.375 µM, 5.5 µM, 11 µM, 22µM, 48 µM) was transferred onto the chip sensing area and incubated at room temperature for 2 hours in a dark environment. The chip was rinsed with DI water, dried using a nitrogen gas and stored in a dark environment for further experiment.

Table 3.2. DNA Probe and Target

Name	Sequence (5'-3')
Oligo 1(probe)	ACA CAC GCA TGA CGA CGT TAT AACA
Complementary target	T GTT ATA ACG TCG TCA TGC GTG TGT
1-mismatched target	T GTT **T**TA ACG TCG TCA TGC GTG TGT
2-mismatched target	T GTT **T**TA ACG TCG TCA TGC **C**TG TGT
3-mismatched target	T GTT **T**TA ACG **G**CG TCA TGC **C**TG TGT
Non-complementary target	G TGC TAG CTA ATC AGC ACT AAA GTA

The DNA probe was designed to target a genome region (26300 to 26321) of severe acute respiratory syndrome coronavirus 2 isolate (SARS-CoV-2/human/USA/LA-BIE-092/2020) whose sequence is used here as the complementary target.

Detection of Target DNA in gold nanoslit. The dried and HPLC purified target DNA (90.2 nmol) was first resuspended in a 902 μL PBS (pH 7.4) to make a 100 μM stock solution. Further dilution was made to obtain the desired concentrations. Under optimal condition of Amino modified AO-ssDNA probe, desired concentrations (0.08, 0.2, 0.5, 1.0, 2, 4, 10, 20, 50, 100 nM) of 100 μl target DNA was incubated with the probe complex for 25 min. Next, the chip was rinsed with DI water before taking measurements. Note that as a check for the assay's specificity, we used mismatched DNA targets. The non-complementary target DNA was used as control and to further demonstrate the selectivity of the sensing method for perfectly matched DNA target. This method shows a distinguished signal for single-base mismatch at room temperature.

Regeneration and Reusability of Probe Films: To regenerate the active sensor surface (AO-ssDNA complex) after hybridization, denaturation of the surface dsDNA was achieved by placing the sensor in a boiling water bath for 5 minutes. This was followed by a rapid cooling in an ice bath for 1 minute and then allowed to reach room temperature before rinsing with DI water.[68] The regenerated biosensor is then incubated with a 0.5 nM ct-DNA for 25 minutes. The probe regeneration and reusability test were performed six times on the same DNA film.

Semi-analytical Modelling: The signature of SPP-mode excitations were quantitatively recognized based on completeness theorem which offers useful information on the efficiency of SPP generation.[69] For light propagating in a non-translational system, the transverse field pattern can be treated as a linear combination of forward- and backward-travelling bounded and radiative modes.[56] Therefore, the SPP generation efficiency e of the transverse electromagnetic fields for the slit geometry and for w/2 <x and x<-w/2 was estimated from equation 1-2. Note that $e_1=e_2$ since in both cases one encounters Au/air interfaces and the overall efficiency can be taken to be e_1+e_2. Here we take account of the normalized SPP excitation strength ($|\alpha^+(x)|^2$ and ($|\alpha^+(x)|^2$ for -w/2<x<w/2, since there is air-metal interface. Note that the field inside the slit consist of the downward and upward-reflected fundamental modes since we are dealing with light diffraction by slit arrays.[69]

$$e_1 = |\alpha_1^+(w/2)|^2 = |\alpha_1^-(w/2)|^2$$

$$= \frac{4\,w' n_1^3}{\pi n_2^2} \left|\frac{\varepsilon^{1/2}}{\varepsilon + n_1^2}\right| \left|\frac{I_o}{1 + (n_1/n_2) w' I_o}\right|^2 \qquad (1)$$

$$e_2 = |\alpha_2^+(w/2)|^2 = |\alpha_2^-(w/2)|^2$$

$$= \frac{4\,w' n_1^3}{\pi n_1^2} \left|\frac{\varepsilon^{1/2}}{\varepsilon + n_2^2}\right| \left|\frac{I_o}{1 + (n_2/n_1) w' I_o}\right|^2 \qquad (2)$$

where n_1, n_2, n_3 and n_4 are the refractive indices of the top Au-air, in-slit Au-air and bottom Au-PDMS interfaces respectively. The normalized slit width, w'=nw/λ where w is the slit width. The integrals I_1 and I_o were calculated numerically for different w' (Table S3 Appendix A) and ε for Au at different wavelengths (Table S4, Figure S10 Appendix A).

Numerical Calculations by Finite-difference Time-Domain (FDTD) Simulation Method. FDTD provides a numerical solution of Maxwells equation which has proved useful for simulating the distribution of electromagnetic field in complex geometries. We used a commercial software package (Lumerical Solutions FDTD) to simulate the optical transmission/reflection and electric field strength of nanoslit array device on PDMS substrate. The simulation domain size is 400nm x 400nm x 1000nm in the cartesian cordinates x, y, and z and the time step was 5fs. The gold film was illuminated under plane wave transverse magnetic

(TM) pulse of wavelength 400-1200nm at normal incidence to the x, y plane (i.e in the positive z-direction) with an amplitude A=1. In order to accelerate the simulation, antisymmetric/symmetric boundary condition was used in x and y directions, and PML boundary condition was placed 1000 nm away from the structure in the z directions to absorb the back-reflected and transmitted radiation at the top and bottom of the mesh.[70] The mesh grid size was set to 0.3 nm in the region near the nanoslit. Gold (Johnson and Christy), with relative permittivity ε =-41.849 at a vacuum wavelength λ_o = 1µm was employed.[71] The optical field distribution and the profile of the optical field in the nanoslits was recorded by a frequency domain monitor and the 3D frequency domain profile monitor respectively. The reflectance spectra were measured by a frequency domain power monitor placed 300nm above the slit structure.

REFERENCES

1. Zhou, L. *et al.* Enhancement of immunoassay's fluorescence and detection sensitivity using three-dimensional plasmonic nano-antenna-dots array. *Anal. Chem.* **84**, 4489–4495 (2012).
2. Zeng, S., Baillargeat, D., Ho, H. P. & Yong, K. T. Nanomaterials enhanced surface plasmon resonance for biological and chemical sensing applications. *Chem. Soc. Rev.* **43**, 3426–3452 (2014).
3. Okamoto, K., Funato, M., Kawakami, Y. & Tamada, K. High-efficiency light emission by means of exciton–surface-plasmon coupling. *J. Photochem. Photobiol. C Photochem. Rev.* **32**, 58–77 (2017).
4. Savasta, S. *et al.* Nanopolaritons: Vacuum rabi splitting with a single quantum dot in the center of a dimer nanoantenna. *ACS Nano* **4**, 6369–6376 (2010).
5. Lertvachirapaiboon, C., Baba, A., Ekgasit, S. & Shinbo, K. Biosensors and Bioelectronics Transmission surface plasmon resonance techniques and their potential biosensor applications. *Biosens. Bioelectron.* **99**, 399–415 (2018).
6. Liu, L. *et al.* Strong Plasmon–Exciton Interactions on Nanoantenna Array–Monolayer WS2 Hybrid System. *Adv. Opt. Mater.* **8**, 1–8 (2020).
7. Wei, H., Ratchford, D., Li, X., Xu, H. & Shih, C. K. Propagating surface plasmon induced photon emission from quantum dots. *Nano Lett.* **9**, 4168–4171 (2009).
8. Pelton, M., Storm, S. D. & Leng, H. Strong coupling of emitters to single plasmonic nanoparticles: Exciton-induced transparency and Rabi splitting. *Nanoscale* **11**, 14540–14552 (2019).
9. Jun, Y. C., Pala, R. & Brongersma, M. L. Strong modification of quantum dot spontaneous emission via gap plasmon coupling in metal nanoslits. *J. Phys. Chem. C* **114**, 7269–7273 (2010).
10. Chen, K. *et al.* High-Q, low-mode-volume and multiresonant plasmonic nanoslit cavities fabricated by helium ion milling. *Nanoscale* **10**, 17148–17155 (2018).
11. Vasa, P. & Lienau, C. Strong Light-Matter Interaction in Quantum Emitter/Metal Hybrid Nanostructures. *ACS Photonics* **5**, (2018).
12. Toropov, N. A. *et al.* Direct enhancement of luminescence of CdxZn1−xSeyS1−y/ZnS nanocrystals with gradient chemical composition by plasmonic nanoantennas. *Opt. Laser Technol.* **121**, 105821 (2020).
13. Tobing, L. Y. M. *et al.* Plasmon-exciton systems with high quantum yield using deterministic aluminium nanostructures with rotational symmetries. *Nanoscale* **11**, 20315–20323 (2019).
14. Pang, L., Ba, L., Pan, W. & Shen, W. Freestanding carbon nanodots/poly (vinyl alcohol) films with high photoluminescent quantum yield realized by inverted-pyramid structure. *Nanotechnology* **28**, 1–7 (2017).
15. Cao, E., Lin, W., Sun, M., Liang, W. & Song, Y. Exciton-plasmon coupling interactions: From principle to applications. *Nanophotonics* **7**, 145–167 (2018).
16. Krasnok, A. E. *et al.* An antenna model for the Purcell effect. *Sci. Rep.* **5**, 1–16 (2015).
17. Morozov, K. M. *et al.* Revising of the Purcell effect in periodic metal-dielectric structures: the role of absorption. *Sci. Rep.* **9**, 1–9 (2019).
18. Li, Y. *et al.* Au@MoS2 Core-Shell Heterostructures with Strong Light-Matter Interactions. *Nano Lett.* **16**, 7696–7702 (2016).

19. Wu, N. Plasmonic metal-semiconductor photocatalysts and photoelectrochemical cells: A review. *Nanoscale* **10**, 2679–2696 (2018).
20. Kholmicheva, N., Romero, L. R., Cassidy, J. & Zamkov, M. Prospects and applications of plasmon-exciton interactions in the near-field regime. *Nanophotonics* **8**, 613–628 (2019).
21. Miao, H., Wang, L., Zhuo, Y., Zhou, Z. & Yang, X. Label-free fluorimetric detection of CEA using carbon dots derived from tomato juice. *Biosens. Bioelectron.* (2016) doi:10.1016/j.bios.2016.06.043.
22. Mourdikoudis, S. & Pallares, R. M. Characterization techniques for nanoparticles : comparison and complementarity upon studying. 12871–12934 (2018) doi:10.1039/c8nr02278j.
23. Trotsiuk, L. *et al.* Plasmon-enhanced fluorescence in gold nanorod-quantum dot coupled systems. *Nanotechnology* **31**, (2020).
24. Dovzhenko, D. S., Ryabchuk, S. V., Rakovich, Y. P. & Nabiev, I. R. Light-matter interaction in the strong coupling regime: Configurations, conditions, and applications. *Nanoscale* **10**, 3589–3605 (2018).
25. Li, X., Zhou, L., Hao, Z. & Wang, Q. Q. Plasmon–Exciton Coupling in Complex Systems. *Adv. Opt. Mater.* **6**, 1–21 (2018).
26. Zhu, Z. *et al.* Plasmon-Enhanced Fluorescence in Coupled Nanostructures and Applications in DNA Detection. *ACS Appl. Bio Mater.* **1**, 118–124 (2018).
27. Halas, N. J., Lal, S., Chang, W.-S., Link, S. & Nordlander, P. Plasmons in Strongly Coupled Metallic Nanostructures. *Chem. Rev.* **111**, 3913–3961 (2011).
28. Baghramyan, H. M. & Ciracì, C. Fluorescence quenching in plasmonic dimers due to electron tunneling. *Nanophotonics* **11**, 2473–2482 (2022).
29. Wustholz, K. L. *et al.* Structure-activity relationships in gold nanoparticle dimers and trimers for surface-enhanced raman spectroscopy. *J. Am. Chem. Soc.* **132**, 10903–10910 (2010).
30. Kumar, S., Doi, Y., Namura, K. & Suzuki, M. Plasmonic Nanoslit Arrays Fabricated by Serial Bideposition: Optical and Surface-Enhanced Raman Scattering Study. *ACS Appl. Bio Mater.* **3**, 3226–3235 (2020).
31. Sanders, M., Lin, Y., Wei, J., Bono, T. & Lindquist, R. G. An enhanced LSPR fiber-optic nanoprobe for ultrasensitive detection of protein biomarkers. *Biosens. Bioelectron.* **61**, 95–101 (2014).
32. Zeng, Z. *et al.* Protein Trapping in Plasmonic Nanoslit and Nanoledge Cavities: The Behavior and Sensing. *Anal. Chem.* **89**, 5221–5229 (2017).
33. Bagra, B., Zhang, W., Zeng, Z., Mabe, T. & Wei, J. Plasmon enhanced fluorescence of carbon nanodots in Gold Nanoslit Cavities. *Langmuir* acs.langmuir.9b00448 (2019) doi:10.1021/acs.langmuir.9b00448.
34. Zeng, B., Gao, Y. & Bartoli, F. J. Rapid and highly sensitive detection using Fano resonances in ultrathin plasmonic nanogratings. *Appl. Phys. Lett.* **105**, (2014).
35. Kevadiya, B. D. *et al.* Diagnostics for SARS-CoV-2 infections. *Nat. Mater.* **20**, 593–605 (2021).
36. Savannah Kaye, Zheng Zeng, Mollye Sandersa, Krishnan Chittur, Paula M Koelle, Robert Lindquist, Upender Manne, Yongbin Lin, J. W. Label-Free Detection of DNA Hybridization with A Compact LSPR-based Fiber-Optic Sensor. *ACS Anal.* **142**, 1974–1981 (2017).
37. Shrivastav, A. M., Cvelbar, U. & Abdulhalim, I. A comprehensive review on plasmonic-

based biosensors used in viral diagnostics. *Commun. Biol.* **4**, 1–12 (2021).
38. Singh, L. *et al.* LSPR based uric acid sensor using graphene oxide and gold nanoparticles functionalized tapered fiber. *Opt. Fiber Technol.* **53**, 102043 (2019).
39. Wang, Z. *et al.* Novel Optical Fiber-Based Structures for Plasmonics Sensors. *Biosensors* **12**, 1–40 (2022).
40. Yano, T. aki *et al.* Ultrasensitive detection of SARS-CoV-2 nucleocapsid protein using large gold nanoparticle-enhanced surface plasmon resonance. *Sci. Rep.* **12**, 1–8 (2022).
41. Zhao, X. *et al.* Optical fiber sensor based on surface plasmon resonance for rapid detection of avian influenza virus subtype H6: Initial studies. *J. Virol. Methods* **233**, 15–22 (2016).
42. Omar, N. A. S. *et al.* Sensitive Detection of Dengue Virus Type 2 E-Proteins Signals Using Self-Assembled Monolayers/Reduced Graphene Oxide-PAMAM Dendrimer Thin Film-SPR Optical Sensor. *Sci. Rep.* **10**, 1–15 (2020).
43. Estmer Nilsson, C. *et al.* A novel assay for influenza virus quantification using surface plasmon resonance. *Vaccine* **28**, 759–766 (2010).
44. Qiu, G. *et al.* Dual-Functional Plasmonic Photothermal Biosensors for Highly Accurate Severe Acute Respiratory Syndrome Coronavirus 2 Detection. *ACS Nano* **14**, 5268–5277 (2020).
45. Du, Y., Huang, J., Weng, X. & Zhou, X. Specific Recognition of DNA by Small Molecules. *Curr. Med. Chem.* **17**, 173–189 (2009).
46. Guo, R., McGoverin, C., Swift, S. & Vanholsbeeck, F. A rapid and low-cost estimation of bacteria counts in solution using fluorescence spectroscopy. *Anal. Bioanal. Chem.* **409**, 3959–3967 (2017).
47. Demeunynck, M., Charmantray, F. & Martelli, A. Interest of Acridine Derivatives in the Anticancer Chemotherapy. *Curr. Pharm. Des.* **7**, 1703–1724 (2005).
48. Shoute, L. C. T. & Loppnow, G. R. Characterization of the binding interactions between EvaGreen dye and dsDNA. *Phys. Chem. Chem. Phys.* **20**, 4772–4780 (2018).
49. Biebricher, A. S. *et al.* The impact of DNA intercalators on DNA and DNA-processing enzymes elucidated through force-dependent binding kinetics. *Nat. Commun.* **6**, 1–12 (2015).
50. Hoory, E. *et al.* Discrimination of Adsorbed Double-Stranded and Single-Stranded DNA Molecules on Surfaces by Fluorescence Emission Spectroscopy Using Acridine Orange Dye. *J. Fluoresc.* **27**, 2153–2158 (2017).
51. Kapuscinski, J. & Darzynkiewicz, Z. Denaturation of nucleic acids induced by intercalating agents: Biochemical and biophysical properties of acridine orange-dna complexes. *J. Biomol. Struct. Dyn.* **1**, 1485–1500 (1984).
52. Armstrong, R. W., Kurucsev, T. & Strauss, U. P. The Interaction between Acridine Dyes and Deoxyribonucleic Acid. *J. Am. Chem. Soc.* **92**, 3174–3181 (1970).
53. Hassanin, H., Mohammadkhani, A. & Jiang, K. Fabrication of hybrid nanostructured arrays using a PDMS/PDMS replication process. *Lab Chip* **12**, 4160–4167 (2012).
54. Schmid, S., Wu, K., Rindzevicius, T. & Boisen, A. Photothermal probing of plasmonic hotspots with nanomechanical resonator. *Proc. IEEE Int. Conf. Micro Electro Mech. Syst.* 1205–1208 (2014) doi:10.1109/MEMSYS.2014.6765864.
55. Daniel, S. & Bawuah, P. Plasmonic Implanted Nanogrooves for Optical Beaming. *Sci. Rep.* 2–9 (2019) doi:10.1038/s41598-018-37202-5.
56. Zeng, Z., Mendis, M. N., Waldeck, D. H. & Wei, J. RSC Advances A semi-analytical

decomposition analysis of surface plasmon generation and the optimal nanoledge plasmonic device †. 17196–17203 (2016) doi:10.1039/c6ra01105e.

57. Suarasan, S., Tira, C., Rusu, M. M., Craciun, A. M. & Focsan, M. Controlled fluorescence manipulation by core-shell multilayer of spherical gold nanoparticles: Theoretical and experimental evaluation. *J. Mol. Struct.* **1244**, 130950 (2021).
58. Fossati, S., Hageneder, S., Menad, S., Maillart, E. & Dostalek, J. Multiresonant plasmonic nanostructure for ultrasensitive fluorescence biosensing. *Nanophotonics* **9**, 3673–3685 (2020).
59. Mabrouk, M., Hammad, S. F., Abdella, A. A. & Mansour, F. R. A novel strategy for ketorolac detection based on turn-on plasmonic enhanced FRET synchronous fluorometric sensor employing micellized chitosan/ AgNPs nanocomposites: Preparation and mechanism investigation. *Colloids Surfaces A Physicochem. Eng. Asp.* **614**, 126182 (2021).
60. Postma, M. *et al.* Uniform cAMP Stimulation of Dictyostelium Cells Induces Localized Patches of Signal Transduction and Pseudopodia. *Mol. Biol. Cell* **14**, 5069–5081 (2003).
61. Song, J. H., Atay, T., Shi, S., Urabe, H. & Nurmikko, A. V. Large enhancement of fluorescence efficiency from CdSe/ZnS quantum dots induced by resonant coupling to spatially controlled surface plasmons. *Nano Lett.* **5**, 1557–1561 (2005).
62. Tanaka, K., Plum, E., Ou, J. Y., Uchino, T. & Zheludev, N. I. Multifold enhancement of quantum dot luminescence in plasmonic metamaterials. *Phys. Rev. Lett.* **105**, 1–4 (2010).
63. Fontaine, N., Picard-Lafond, A., Asselin, J. & Boudreau, D. Thinking outside the shell: Novel sensors designed from plasmon-enhanced fluorescent concentric nanoparticles. *Analyst* **145**, 5965–5980 (2020).
64. Bauch, M., Toma, K., Toma, M., Zhang, Q. & Dostalek, J. Plasmon-Enhanced Fluorescence Biosensors: A Review. *Plasmonics* **9**, 781–799 (2014).
65. Markegard, C. B., Gallivan, C. P., Cheng, D. D. & Nguyen, H. D. Effects of Concentration and Temperature on DNA Hybridization by Two Closely Related Sequences via Large-Scale Coarse-Grained Simulations. (2016) doi:10.1021/acs.jpcb.6b03937.
66. Yazawa, K. & Furusawa, H. Probing Multiple Binding Modes of DNA Hybridization: A Comparison between Single-Molecule Observations and Ensemble Measurements. *ACS Omega* **3**, 2084–2092 (2018).
67. Xu, S. *et al.* Real-time reliable determination of binding kinetics of DNA hybridization using a multi-channel graphene biosensor. 1–10 (2017) doi:10.1038/ncomms14902.
68. Peterson, A. W., Wolf, L. K. & Georgiadis, R. M. Hybridization of mismatched or partially matched DNA at surfaces. *J. Am. Chem. Soc.* **124**, 14601–14607 (2002).
69. Lalanne, P., Hugonin, J. P. & Rodier, J. C. Approximate model for surface-plasmon generation at slit apertures. *J. Opt. Soc. Am. A* **23**, 1608 (2006).
70. Xie, Y., Zakharian, A. R., Moloney, J. V. & Mansuripur, M. Transmission of light through a periodic array of slits in a thick metallic film. *Opt. Express* **13**, 4485 (2005).
71. P. B. Johnson and R. Christy. Optical constants of transition metals: Ti, V, Cr, Mn, Fe, Co, Ni, and Pd. **9**, 5056–5070 (1974).

CHAPTER IV: A PLASMONIC NANOLEDGE ARRAY FOR SENSITIVE DETECTION OF CARDIOVASCULAR DISEASE BIOMARKER

Overview

In the present study, we report on a sensitive and label free cardiac troponin I (cTnI) optical biosensor based on a plasmonic nanoledge (NL) structured chip. The use of NL provides a compact system that detects elevated levels of cTnI with just a drop of blood sample. To construct the cTnI detection chip, the NL surface is tethered with DNA aptamers designed to specifically capture cTnI biomarker. The interaction between the NL-array with incident white light provides transmitted surface plasmon resonance (tSPR) signal, i.e., an extraordinary optical transmission (EOT) spectrum, which shifts due to changes in refractive index (RI) caused by the biological binding activity at the NL metal surface, thus enabling the quantitation of cTnI level. The NL array chip demonstrated high sensitivity of cTnI detection in buffer, human serum (HS) and human whole blood (HB) mediums at the lowest detection limit of 0.079 ng/mL, 0.084 ng/mL, and 0.097 ng/mL, respectively. Control measurements using blank target mediums and those containing up to 125 ng/mL of additional proteins, such as myoglobin, creatin kinase or heparin, reveal little interference and high specificity. In brief, the significant advance of the sensing device is the NL plasmonic structure capable of rendering optical signal transduction at the near-infrared (NIR) region and minimizing interferences from most biological species in human whole blood. The performance of this NL plasmonic biosensor offers promise in application for clinical analysis and promotes its development as a point-of-care device for earlier cardiovascular disease (CVD) diagnostics.

Introduction

Recently, advances in developing biosensors directed one of emerging areas based on nanostructure “antenna”-aptamer-analyte sandwich approach.[1-2] The operations related with this mode of signal transduction involves a three-layer steps whereby the first functionalized “antenna” layer captures the second recognition layer, e.g. aptamer, and the second layer selectively captures the third layer (target analyte) to produce measurable signals unique for each attachment step. The collection of incident light and the transduction of biomolecular interaction at the interface generates the final optical signal through the metallic antenna. The character of the antenna determines the classification of the responsive nanostructure either as light-scattering,[3-4] fluorescence,[5] colorimetric,[6,7,8] SERS,[9] or surface plasmon resonance (SPR) sensors.[10-11] Notably, these systems are mostly based on indirect signal transduction such as the conversion of chemical response into electrical or optical signals and vice versa. This presents opportunities to developing integrated circuits,[12-13] and biosensors[14] with innovative functions for improving the quality of life.

It is an agelong desire especially for humans to be healthy. But reality often acts on the contrary. The human life is constantly threatened by disease and plaques. Some diseases show early symptoms and are easily detectable, while others don’t, and by the time symptoms appear, it becomes difficult or too late to fight the disease.[15] This presents a more pressing challenge since most of the advanced testing tools in today’s hospitals are more effective when patients show symptoms. According to WHO,[16] cardiovascular (heart) disease (CVD) tops the list of all deadly diseases. It kills one person every 36 seconds in the US alone and an annual death estimate of 19 million worldwide.[17] Modern clinics rely on electrocardiogram (ECG), phonocardiography (PCG), and photoplethysmography (PPG) to track abnormalities based on the heart's rhythm, acoustics, and volumetric changes in blood circulation respectively.[18] Traditionally, the ECG is widely used to monitor heart malfunction in real-time. It measures abnormal heart rhythms as a sign of cardiac symptoms. The problem is that such abnormal rhythms are short-lived; they come and go.[19] For this reason, measurements using the ECG needs to be taken continuously for a period of 24-48 hours before treatment can commence. Such delays could result in complication and even death. About 43% of patience with cardiac malfunction have shown normal or non-diagnostic ECG on admission to the Emergency Room.[20] With 25% of acute myocardial infarction (AMI) happening without any symptoms like chest, back or jaw pains, there is need for an alternative platform that offer a rapid, sensitive, accurate, earlier and cost-effective AMI diagnosis.[21]

The secrete to modern disease prediction relies on the fact that the presence of certain unique biomolecules (biomarkers) in the bloodstream is indicative of a particular biological condition or ailment.[22] For many decades, CVD or heart attack has been diagnosed and managed after the muscle cell of the heart has been severely damaged, resulting in low survival rates.[22] Biomarkers have been found to be very effective instruments for CVD detection and monitoring because they serve as beacons for the physiological status of the heart cells at a giving time and change at the early stage of the disease process.[18]

In the early 1960s, creatin kinase (CK) has been utilized as a marker for acute myocardial infarction (AMI) because of its better specificity to coronary occlusion than prior markers like aspartate amino transferase (AST).[23] However, CK suffers a major drawback. It cannot be detected soon after the onset of cardiac symptoms due to its slow elevation in plasma after heart injury.[24] As a result, the search for a marker that could be used to confirm or refute the diagnosis of AMI turns attention to cardiac troponin I (cTnI).[23-25] It is one of the three subunits of the cardiac Troponin complex and remains the most specific biomarker for myocardial tissue damage.[26-27] Its early release into the bloodstream makes it a suitable substitute to existing risk assessment mechanisms.[24] The cTnI is a structural protein biomarker, whose presence in the bloodstream is indicative of heart damage. Most commercialized tools for cTnI detection are based on the enzyme-linked immunosorbent assay (ELISA),[28] chemiluminescence enzyme immunoassay (CLEIA),[29] or immunofluorescent labelling.[30] Since these assays employs antibodies as probes for capturing cTnI biomarker, their stability is low resulting in short shelve life.[31] The antibodies are susceptible to denaturation due to temperature changes,[32] they cannot be synthetically produced,[33] thus leading to high costs.[32] Other drawbacks include low sensitivity, long processing time and the requirement for large amount of blood sample for detection of troponin levels.[34,35] The use of selective aptamers as cTnI recognition agents circumvents most of these drawbacks.[36,37,38]

Notably, recent technologies that are based on the sandwich nanostructure has found relevance in analyzing biomarkers for disease diagnosis and prognosis.[39-40,41] While the pattern of detection procedure differs for these advanced biosensors, a common feature is the employment of thin metal films or nanoparticles coated or immobilized on glass, polycarbonate or other metal substrates.[42,43] These components present an ideal platform for the development of sensitive diagnostic devices with operational simplicity and capability for real-time investigation of molecular interaction.[44,45] The dominant limiting aspects with the use of thin-film metals is the requirement of a quartz prism by these traditional SPR sensor scheme to achieve resonance conditions.[46] The complex optical system limits their versatility, miniaturization and integration into a point-of-care (POC) platforms.[44] In the case of nanoparticle platforms, one encounters poor reproducibility due to difficulty in synthesizing reproducible and uniformly sized particles.

An alternative approach that eliminates the prism and offers high precision reproducibility is the use of gratings, in which the resonant condition is provided by diffraction of incident light. Although this approach requires more complex fabrication steps, it remains the most attractive due to its higher miniaturization and integration capabilities.[46,47] The key limitation shared by most optical sensors include the dependence of the signal intensity on the sensing samples and environment. For example, the use of human whole blood samples may cause partially quenched signal transduction due to light absorption compared to a clearer medium such as the saliva, sweat, urine or serum.[48]

Despite these general shortcomings, plasmonic sensors based on metal gratings continue to gain more attention in the development of smaller POC devices which offer medical diagnostic testing in proximity to the patient's location while eliminating the need to take specimen away from the patient to a centralized medical laboratory.[49] These developments are made possible by the exploitation of nanostructured SPR and/or localized surface plasmon resonance (LSPR) which involve the oscillation of electrons at a metal-dielectric interface in response to an incident light propagating in the visible and near infra-red frequencies.[50-51] The platforms integrate the advantages of high detection sensitivity, low detection limit and eliminates the complex optical instrumentation associated with conventional sensing platforms, thus, making POC possible.[52] The sensitivity of SPR to changes in near-surface refractive index (RI) makes them suitable probes for surface binding events and hence, their extensive utilization in numerous SPR-based sensors and biosensors. [47,52,53,54] The urgency to develop advanced SPR/LSPR-based biosensor is predicated upon the need to provide superior performing diagnostic tool with enhanced stability and high RI sensitivity, capable of overcoming unwanted binding or weak target binding.[55,56]

In this paper, we report on our recent progress of developing a miniaturized SPR nanoledge (NL)-array and demonstrated its application for a sensitive and label-free detection of a cardiovascular disease biomarker, cTnI. To fabricate the device, an approach based on a high precision electron-beam and deep UV lithography processes was utilized for patterning and etching of NLs, followed by a gold layer deposition on a chromium adhesion layer. The resulting gold coated NL arrays provide a much reproducible, uniform, and robust SPR chip surface. The method was chosen for its scalability, precision, and capability to produce high aspect-ratio patterns.

The principle of the sensing scheme is based on the extraordinary optical transmission (EOT) of light through the NL array. According to Bethe's theory, the diffraction limit of light restrict light to pass through an orifice smaller than its wavelength.[57] However, subwavelength apertures in metal films can transmit light due to surface plasmons excitation which mediates light tunnelling and transmission, and hence giving birth to the phenomenon of EOT.[58,59] The wavelength of optical transmission through the NL aperture can be approximated by the equation:[60]

$$\lambda_{SPR} = \frac{nP}{\sqrt{1 + n_{eff}^2 / \varepsilon_m}} \qquad (1)$$

From Eq. 1, the spectral characteristics of the EOT depends on the effective refractive index (n_{eff}) at the metal/dielectric interface, the hight (h), width (W) and periodicity (P) of the nanoaperture and the resonance wavelength (λ) at the phase matching condition. Since the size, shape and geometry of the metal aperture determines the efficiency of SPP excitation, the SPR mediated EOT is also dependent on the geometry of the nanoaperture. The wavelength sensitivity of EOT to changes in RI at the metal surface is what informed our decision to use the NL EOT-based system to interrogate biological binding interactions at the metals surface.

Figure 4.1. Schematic Illustration of the Sensing Principle and the Surface Preparation for Selectively Binding the Protein Biomarker cTnI at the NL Gold Surface

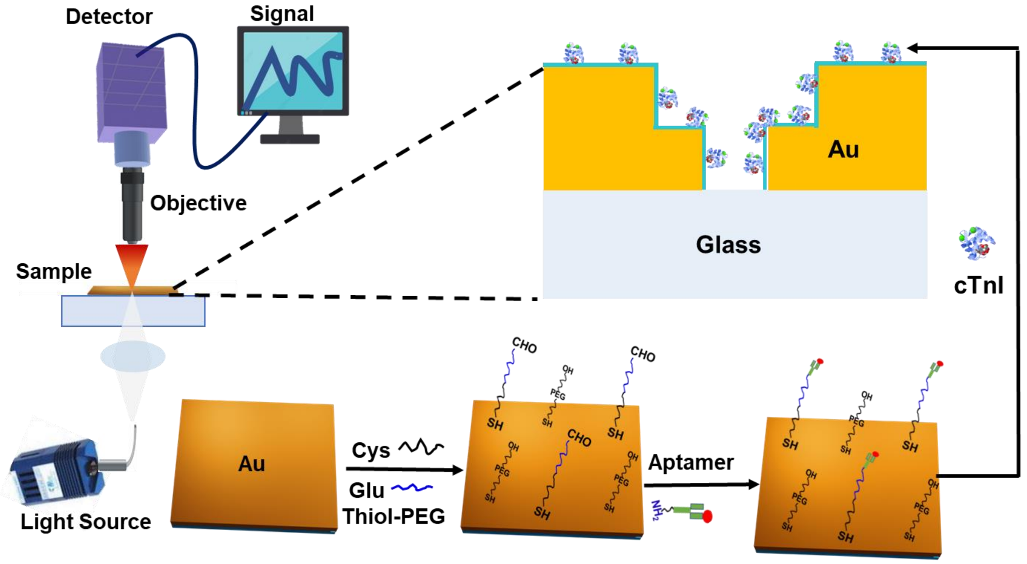

Figure 4.1 depicts the cTnI sensing approach. First, the NL probe was functionalized with a self-assembled monolayer (SAM) of cystamine/glutaraldehyde and further tethered with a desired amine modified DNA aptamer whose function is to specifically recognize and capture cTnI. The binding event between the aptamer and cTnI is then monitored by transmission spectroscopy. The reported device displayed a strong EOT at the near-infrared (NIR) regime, providing an advantage of minimizing interfering absorption and fluorescence from biological samples. The implementation of the uniformly fabricated NL array as SPP-based device avoids the use of bulky optics and complex mechanics while offering a superior sensitivity and selectivity, monitored by changes in resonant EOT wavelengths caused by the metal films-analyte interaction. This precisely fabricated NL array offers an advantage for direct differentiation of the CVD biomarkers and promises a new miniaturized POC device for early CVD diagnosis.

The ability of the human blood to solubilize numerous body substrates including nutrients, ions, vitamins and proteins pose a challenge towards developing a disease testing technology that targets only one component with high selectivity and specificity.[2] Also, the direct quantitation of analytes in blood samples is difficult especially for optical sensors since the red color of the blood can absorb light and diminish the output signal. In this work we demonstrate the ability of the NL array to provide the optical signal differentiation and specificity for quantitation of the cTnI biomarker in human whole blood, presenting a notable attainment in the field of biosensing.

Results and Discussion

Fabrication and Characterization

The finite difference time domain (FDTD) simulations show that the NL structure can lead to an intense concentration of electromagnetic field around the surfaces of cavities due to the strong excitation of both localized and propagating SPR.[11,61] The resulting optical signal enhancement and its sensitive response due to RI changes form the foundation and principle of the SPR-based biosensors.[62] In this report, the NL array was fabricated in a 250 nm thick gold film supported on a transparent glass substrate. Each device (25.4 x 12.2 mm) has four NL arrays and one reference burnt box (no gold coating). Notably, the four identical NL arrays on the chip were used for reproducible study. By design, the NL-arrays and reference burnt box are ~ 45 µm x 75 µm each in dimension and are 1 mm apart **(**Figure 4.2A**)**. Figure 4.2B shows the SEM image of the NL array. The close view of the NL structure shows precisely fabricated NL of the geometrical deviation within ± 0.5 nm.

Figure 4.2. (A) Top-Down and Cross-Section View of NL Array (B) SEM Image of the Fabricated NL Array with Iserted Photo of the Gold Slide at Close View of the NL Structure

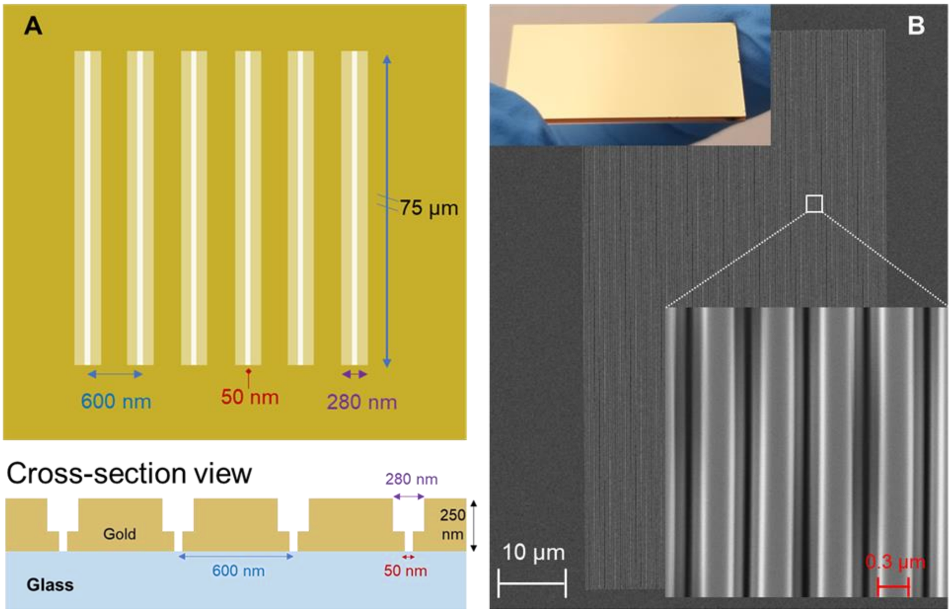

Sensitivity to Refractive Index Changes

Methanol, water, ethanol, and isopropanol solvents were used to determine the bulk RI sensitivity of the gold NL-SPR sensor. The solvents were selected due to their small differences in RI. This makes it possible to determine if the device would be responsive enough to accurately determine small wavelength shifts. Figure S1 in Appendix B shows the transmitted light spectra in the presence of the different solvents before any pre-treatment or functionalization of the gold surface. The EOT red-shifted according to increasing RI of the four solvents. From the slop of the linear relationship between RI and EOT wavelength position, the sensitivity of the device is found to be ~118 nm/RIU without hydrophilization. The low sensitivity value may be caused by the inability of the solvents to efficiently penetrate down the NL structure due to the high hydrophobicity at the bare metal surface. To overcome the hydrophobic effect and enhance the access of solvent or analyte to the sensing area, the chip was subjected to surface pretreatment. Traditionally, exposing gold surface to Ar/water plasma or Ar plasma increases wettability.[63] But this approach increases the metal surface roughness and dampens the evanescence field. For this reason, we carried out surface pretreatment by irradiating the chips with UV/ozone to form a gold oxide monolayer. This approach enhances wettability without compromising the integrity of the metal surface.[63] Hence, the evanescent field length remains unaffected.

Figure 4.3 shows the EOT spectra of the solvents after irradiating the NL with UV/ozone. The primary EOT peaks red-shifted in the presence of the solvents with a linear dependence on RI. From the linear plot, the sensitivity is found to be 384.1 nm/RIU. The increase in sensitivity from 118 nm/RIU to 384.1 nm/RIU may be attributed to the enhancement in surface wettability and accessibility of the NL. Since the solvents have minimal to no chemical tendency to bind or react with the treated Au surface, the observed wavelength responses are taken to come from changes in the RI of the bulk medium rather than surface binding.

Figure 4.3. (A) Measured Transmittance (EOT) Spectra for the NL-SPR Probe in Various Solvents. (B) Linear Fit of the tSPR Peak Wavelength

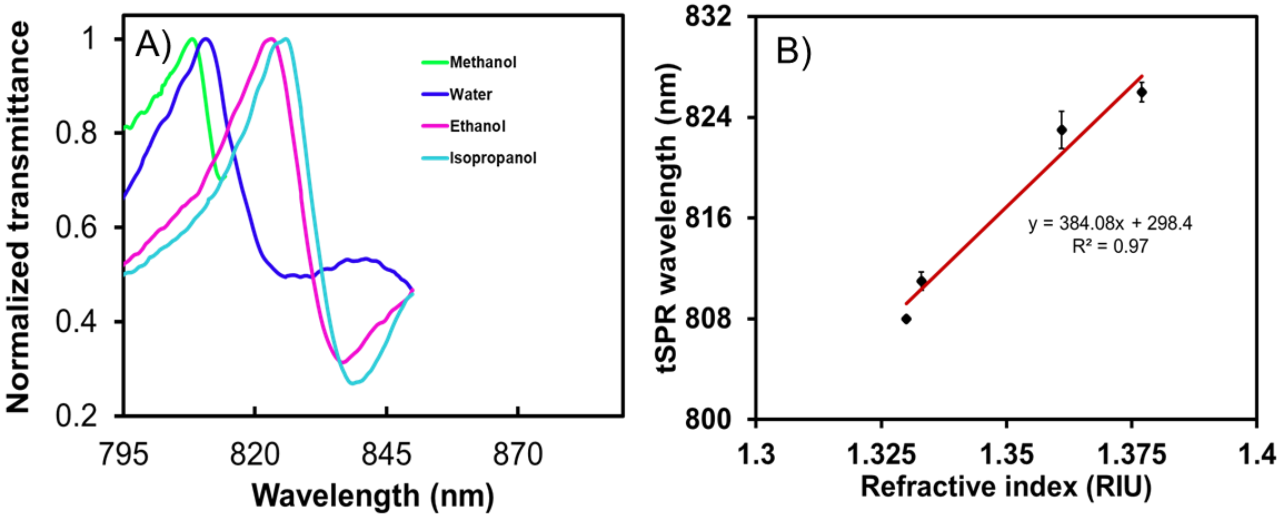

Cardiac Biomarker (cTnI) Detection

In a separate experiment, the surface self-assembly approach was used to further investigate the responsiveness of the device due to surface binding. This was achieved by chemical functionalization of the NL with cystamine/glutaraldehyde to form a monolayer as depicted in Figure 4.1. This step is necessary not only to increase the surface wettability but to serve as molecular linker for the DNA aptamer. Figure S2 in Appendix B show the EOT response for SAM formation due to cystamine/glutaraldehyde and aptamer immobilizations. The red shift in EOT peak indicates the binding events occurring at each step.

Optimization of TnI binding time

After aptamer immobilization onto the NL via the cystamine/glutaraldehyde link, the binding kinetics of cTnI target onto the aptamer was deduced by monitoring the time it takes for the aptamer-cTnI interaction to reach equilibrium. First, a blank measurement without cTnI was taken to account for any non-specific interactions due to solvent interference and to also account for any noise signals due to thermal or vibration of the analytical instrument to establish a baseline for the biosensor. Figure S3 in Appendix B show a red-shift in the EOT peak wavelength position as incubation time increases and reaches equilibrium after 20 min indicating the completion of the aptamer-cTnI interaction. Hence, an incubation time of 20 min was used in subsequent experiments in cTnI detection.

Detection performance of EOT aptasensor

The sensitive property of the EOT to changes in RI at the NL was employed for the quantification of cTnI protein in PBS, HS and HB. To quantify cTnI and determine the linear detection range of the sensor, various concentrations of cTnI (0.0001, 0.001, 0.01, 0.156, 0.625, 2.5, 10, 40, 70, 100 ng/mL) prepared in PBS buffer and spiked in biological mediums (i.e., human serum and human whole blood) were evaluated. Figure 4.4 show that as the concentration of cTnI is increased, the EOT peak wavelength position shows red shifts in all three mediums.

By plotting the shift in wavelength versus the natural logarithm of the concentration of cTnI, the calibration curves in three mediums were obtained, as displayed in Figure 4.4D.

The inner ledges are designed to enable SPR excitation for EOT and to capture the biomarkers and thus provide increased sensitivity to the device.[62] Initially, clean gold nanoledge is chemically modified to have a terminal carbonyl group that covalently bind with an amine modified cTnI aptamer.[64] Since the aptamer is designed to specifically target cTnI protein, incubating the aptamer modified sensor with cTnI results in another binding interaction. Each of the binding interactions that starts from the surface functionalization to cTnI detection causes a change in the refractive index at the metal surface. This is evidenced by the spectral shift from ~800 nm (NL before functionalization) to 840 nm (cTnI in PBS), 849 nm (cTnI in HS) and 859 nm (cTnI in HB). The shift in the resonant wavelength position during the binding stages provides the sensing capability of the device. The three linear calibration lines for TnI in the different mediums (Figure 4.4D) do not overlap but are rather off-set to a higher wavelength as the analyte medium changes from PBS to HS and HB respectively. The linear off-set may be due to the difference in the RI of the PBS, HS and HB.

Figure 4.4. A tSPR Recorded Upon TnI Incubation with Aptasensor at Different Concentrations in (A) PBS, (B) Human Serum, and (C) Human Whole Blood (D) Calibration Plot for cTnI in PBS (black), Human Serum (blue) and Human Whole Blood (red)

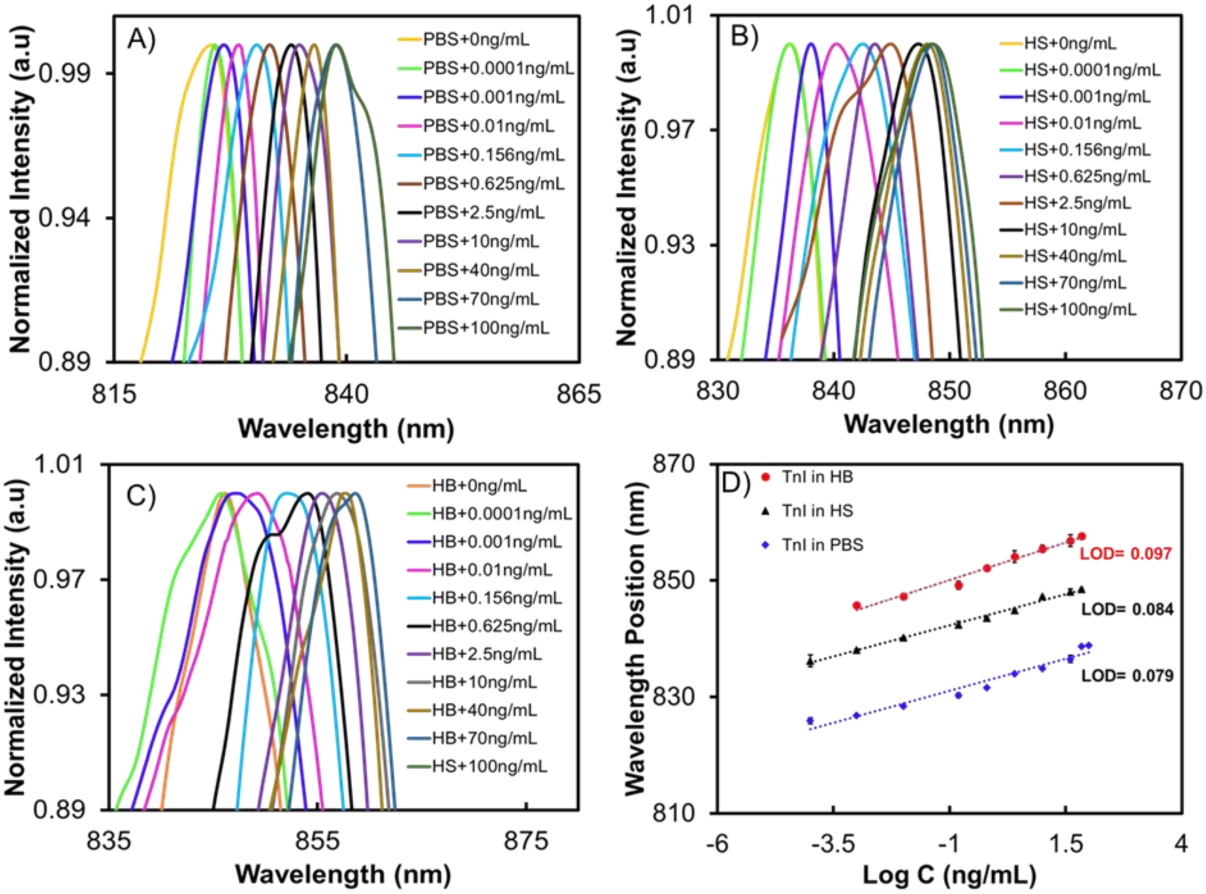

The calibration plot for cTnI in buffer (blue dotted line) represents a regression equation of $\lambda(\mathrm{nm}) = 2.2 \pm 0.16 \text{ x} \log \mathrm{C}\ (\mathrm{ng/mL}) + 833.3\ (\mathrm{nm}), R^2 = 0.98$. The limit of detection (LOD) of the biosensor was evaluated from the formular $LOD = 3\sigma/S$, where σ is the standard deviation of the blank signal and S is the slop of the calibration plot.[65] The LOD was found to be 0.079 ng/mL and the linear range of detection goes from 0.0001 ng/mL to 70 ng/mL. Similarly, we analyzed the LOD in HS samples. The linear regression equation $\lambda(\mathrm{nm}) = 2.14 \pm 0.09 \text{ x} \log \mathrm{C}\ (\mathrm{ng/mL}) + 844.47\ (\mathrm{nm}), R^2 = 0.993$ and LOD=0.084 ng/mL was obtained.

Notably, the human blood has often served as one of the most suitable samples collected for medical diagnosis because it serves as a carrier for most disease. Hence it is critical to determine the sensor's effectiveness in whole blood detection. Figure 3C shows the EOT spectra of cTnI spiked in human whole blood. For cTnI in the low concentration range between 0.0001 ng/mL and 0.001 ng/mL, there was no significant shift in EOT wavelength position relative to the background (blood without cTnI). At a higher concentration range of cTnI (0.001 ng/mL to 70 ng/mL), the shift in wavelength becomes significant and correlates with the increase in concentration, presenting an aptamer-cTnI interaction with a linear regression equation $\lambda(\text{nm}) = 2.64 \pm 0.085 \text{ x} \log \text{C} \text{ (ng/mL)} + 852.75 \text{ (nm)}, R^2 = 0.982$ and LOD=0.097 ng/mL. The linear detection range and the LOD values for cTnI in PBS, HB and HB indicate that the NL sensor could distinguish between a healthy person from afflicted patients since normal cTnI levels lies between 0-0.04 ng/mL while levels above 0.40 ng/mL indicates AMI.[2,4]

In order to verify the response of the device to non-target species, known amounts of interferents, namely myoglobin, creatin kinase and heparin were introduced in PBS buffer at 0.156 ng/mL to 125 ng/mL concentrations. This is our way of mimicking the multi-component nature of the human blood and determining the specificity of the sensor device. Myoglobin and creatin kinase were selected because like cTnI, they are also released into the blood stream during cardiac malfunction.[54] Heparin on the other hand is commonly used as treatment for heart disease which is why it is necessary to ensure that such treatment does not interfere with the integrity of the sensor to monitor cTnI levels during treatments.[26] Confirming the absence of non-specific binding of the foreign species to the detection area would present this device not just as sensitive but specifically selective to cTnI. This hypothesis is validated with the results in Figure 4.5. For the different concentrations of myoglobin, creatin kinase and heparin, a very small fluctuation in EOT wavelength position were observed at 125 ng/mL of interferents relative to the shift observed for cTnI at a lower concentration of 0.156 ng/mL. This indicates the poor binding of the interfering species unto the recognition element, demonstrating the specificity of the aptamer binding to cTnI.

Figure 4.5. tSPR Measurement for the Recognition of (A) Myoglobin, (B) Heparin and (C) Creatin Kinase. (D) tSPR Recorded Using 4 Different Fabricated Aptasensor Showing the Reproducibility of the Aptasensor with 2.5 ng/mL TnI in PBS

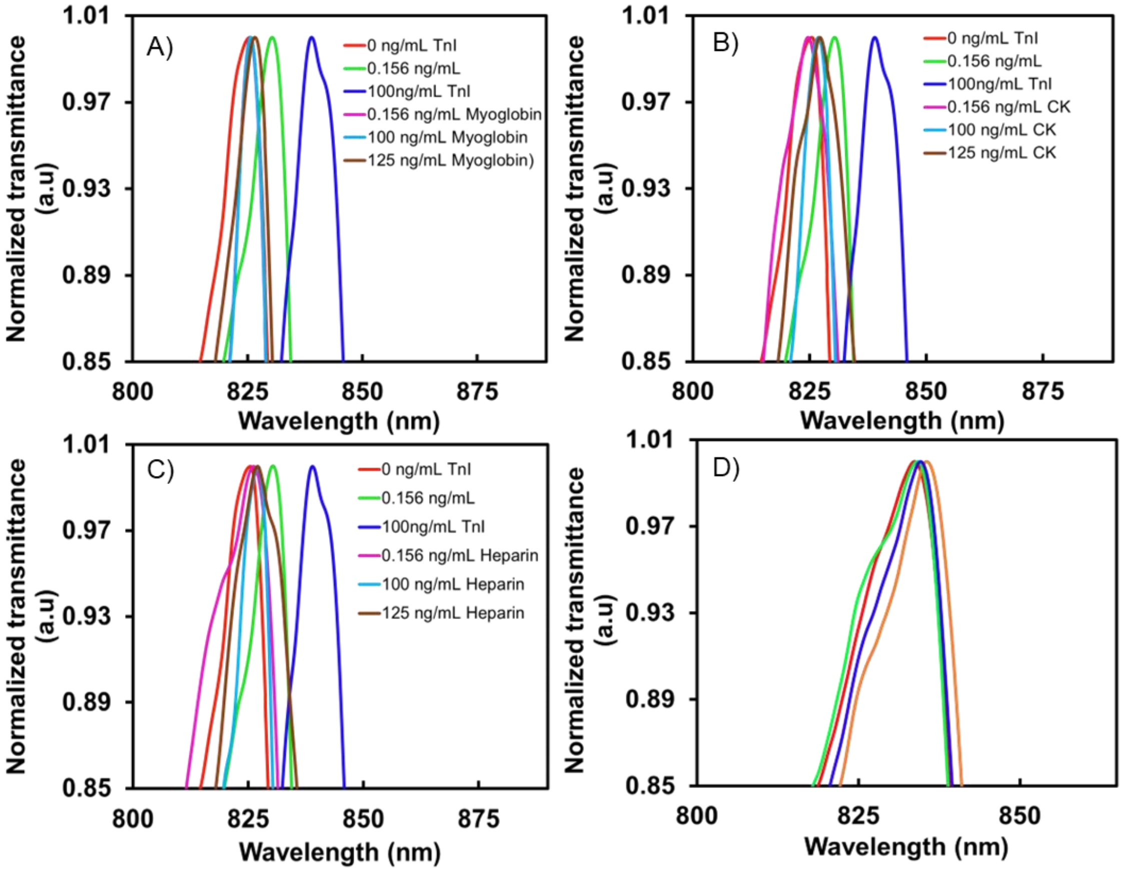

Reproducibility of the cTnI aptasensor

In order to investigate the reproducibility of the cTnI aptasensor, the sensor-to-sensor variation of four differently fabricated biosensors was determined using a 2.5 ng/mL cTnI in human serum. The EOT responses for each sensor device was recorded separately. As shown in

Figure 4.5D, the wavelength positions for all four devices differ by about 0.1% relative standard deviation. This confirms the reproducibility of the sensor device.

Stability and Reusability of the Aptasensor

It is desirable for an aptasensor to be stable; a property that will allow it to be stored and deployed easily to location of application without losing its ability for precise analyte detection.[66] To assess the stability, seven identical aptamer-immobilized NL sensors were stored in a refrigerator at 4°C and measured at three days interval before and after incubating with 10 ng/mL TnI in PBS at room temperature. Figure S4 in Appendix B indicates that the transmitted wavelength position on the first three days is consistent with the one observed after 21 days. The sensors maintained above 99% ± 0.8 of the original measurement signal after 21 days. With economic implication in mind, we further investigated the reusability of the aptasensor. Owing to the tight link between the -SH groups of the aptamers and the gold NL surface, the aptasensor is able to regenerate the aptamer layer after binding with the TnI protein. This was achieved by inserting the used sensor in a 95°C deionized water for 5 minutes.[67] Figure S5 in Appendix B shows the recovery of the aptamer layer after multiple regeneration cycles. A noticeable loss of aptamer regeneration peak signal was observed in the fourth regeneration cycle likely due to feeble affinity of TnI to the aptamer whose stability is impacted by the intermittent heating and cooling cycles.[66] However, 99.5% signal recovery was obtained after three regeneration cycles which demonstrate the acceptable reusability of the NL-aptasensor.

The Binding Event Analysis

The red shift in wavelength resulting from the increase in cTnI concentration (Figure 4.4) is taken to be due to the formation of a thin organic layer bound to the metal's surface. The thickness of the monolayer at different stages of the multi-layer formation is estimated based on equation (2).[68]

$$\Delta\lambda = m(n_{adlayer} - n_{air})[exp(-2d_1/\mathrm{l_d}][1 - exp(-2d_2/l_d)] \qquad (2)$$

The change in SPR response, $\Delta\lambda$, is defined as the shift in wavelength of the SPR maximum in transmitted light intensity associated with changes in RI of material due to adlayer formation at the metal surface, where m, is the sensitivity of the device measured in RIU (the slop of the calibration curve shown in Figure 4.3B), and $n_{adlayer}$ (cystamin=1.58,glutaraldehyde=1.433) are the RIs of the adsorbed molecular layer,[53] d_1 is the thickness of first or intermediate layer and d_2 represent the thickness of the second or subsequent adsorbed layer, l_d is the SPR decay length. When the intermediate layer (for example cystamine, sandwiched between Au surface and glutaraldehyde) is very thin relative to l_d of the sensor, the dependence of l_d on RI approaches zero.[68] This mean that the influence of the intermediate layer on the responsivity of the sensor to the next added layer is negligible. Under such conditions, the parameter $exp(-\frac{2d_2}{l_d})$ in equation (2) approaches one. Hence, by rearranging Eq. 2, the relationship between $\Delta\lambda$ and adsorbed thickness, d, becomes.[68]

$$d = (l_d/2)\{\frac{\Delta\lambda}{[(m(n_{SAM} - n_{air})]}\} \qquad (3)$$

To estimate the value of l_d, Eq. 3 was used to fit the experimental data as shown in Figure S6 in Appendix B. The best fit was obtained using l_d=122.9 nm. A more accurate estimate of l_d comes from Maxwell's equation,[69]

$$l_d = (\lambda/2\pi)/\mathrm{Re}\{-\frac{n_{sample}^4}{n_{sample}^2 + \varepsilon_{metal}}\}^{1/2} \qquad (4)$$

For the Au nanoledge sensor with dielectric constant ε_{metal}=1.526 at SPR maximum wavelength λ=803.56 in PBS of refractive index, $n_{sample} = 1.15$, the estimated l_d is 134.0 nm.

The two estimates closely agree with each other. By using the value of l_d =134.0 nm, the adlayer thickness due to surface functionalization and cTnI binding to the probe at different concentrations was obtained.

To determine the successful realization of thin-film layer formation arising from binding events happening at the metal's surface, the functionalization step, aptamer immobilization and cTnI binding was monitored by observing the wavelength (λ) peak shift during each step. The estimated thicknesses starting from the formation of SAM to the sensing of TnI at different concentrations is determined according to the measured average $\Delta\lambda$ as shown in Table S1 in Appendix B. The estimated average thickness due to cystamine/glutaraldehyde SAM is ~1.14 nm (l_d 134, m=384.08), while aptamer thickness is ~0.22 nm **(**RI of $_{\mathrm{DNA}}$=1.7).[70] The surface coverage of the sensing area ($3.75\mathrm{x}10^{-5}\mathrm{cm}^2$) due to aptamer immobilization is about 9.915×10^{15} molecules/cm^2. From Figure S7 in Appendix B the adlayer thickness responds linearly to the change in wavelength position, Δλ, and correlate with the change in concentration.

In comparison to other sensing assays (**Table 4.1**), our methodology demonstrates a competitive turnaround time and signal response to low cTnI concentration in different mediums including the human whole blood. This presents an improvement in developing a plasmonic device for the quantitation of cTnI to complement the EKG monitor used by health emergency workers and superior for early detection of the risk of heart attack. This capability further promotes the use of our technique to develop future POC devices for disease diagnostics.

Table 4.1. Detection Methods and Performance of Different cTnI Assays

Detection method	**Transducer**	**Target**	**Detection range**	**LOD**	**Real matrix**	**Analytic time (min)**
SPR/fluorescence[65]	Au chip	cTnI	84 aM-350 pM	35 aM	PBS	60
Electrochemical[1]	Au electrode	cTnT	0.05-5 mg/mL	0.017 mg/mL	Serum	30
Fluorescence[71]	Quantum dot	cTnI	0-1.745 μM	32 nM 55 nM	PBS Human plasma	<1
Electrochemical[4]	Carbon nanofiber	cTnI	0-1μg/mL	0.2 ng/mL	PBS	60
SPR/ Electrochemical[2]	electrode	cTnI	0.015 ng/mL 0.1 ng/mL	0.015 ng/mL 0.1 ng/mL	PBS Whole blood	30
SPR[72]	Si3N4 chip	cTnI	0.05-10 ng/mL	0.05 ng/mL	Human serum	30
SPR[73]	Au/polydopamine	cTnI		1.25 ng/mL	HS	40
SPR[74]	Au film	cTnI	0-160 ng/mL	0.068 ng/mL	PBS	5
SPR[75]	Au nanorod	cTnT	7.6-fg/mL-910 μg/mL	8.4 fg/mL	PBS	10s
This Study	Au chip	cTnI	0.0001-70 ng/mL 0.0001-100 ng/mL 0.001-100 ng/mL	0.079 ng/mL 0.084 ng/mL 0.097 ng/mL	PBS Serum Blood	20 min

Conclusion

In summary, a chip-based plasmonic biosensor was developed by etching plasmonic NL channels on a metallic gold for NIR EOT signal. The nanoledge device exhibits high sensitivity for the detection of cTnI over a wide range of concentrations (0.0001 to 100 ng/mL) with an excellent detection limit of 0.079, 0.084, 0.097 ng/mL in PBS, human serum, and human whole blood, respectively. A remarkable selectivity against interferents such as spiked myoglobin, creatin kinase, heparin, and additional species in whole blood was achieved by modifying the sensor with specific cTnI aptamers. The superior performance characteristic arises from the NIR EOT through the NL structure and the selectivity of the recognition element leading to an optical signal that is highly sensitive to small changes in RI due to the binding event at the NL surfaces. Considering the stability, reusability, and high sensitivity towards cTnI in different biological mediums, this chip-based plasmonic device could potentially leads to a breakthrough in the development of a POC analytical tool for future clinical use.

Materials and Methods

Materials and Reagents

Cystamine dihydrochloride (98%), glutaraldehyde solution, thiol PEG (SH-PEG), glycine, Human serum (male; blood type, AB, cat.# H4522) and heparin sodium salt, were all purchased from Sigma-Aldrich and used without further purification. Creatin kinase (Cat. # 9076-ck), myoglobin (Cat.# NBPI-50959), human heart troponin I (Cat.# 648480) and phosphate buffer saline (PBS) were obtained from fisher scientific. The TnI aptamer 5’-/5AmMC6/-CGT GCA GTA CGC CAA CCT TTC TCA TGC GCT GCC CCT CTT A-3’ (Cat.# 316487191) was purchased from integrated DNA technologies. Methanol, ethanol and isopropanol were purchased from Sigma-Aldrich and used without further purification.

Optical Characterization

The optical setup shown in Figure 4.1 was used to acquire the EOT characteristic of the device. The microscope used was connected to an external tungsten halogen white light source (LS-1, Ocean Optics Inc., USA) via an optical fiber. The white light is launched on to the Au nanoledge by passing through the microscope’s condenser. The characteristic transmitted light spectra are then measured by the spectrometer which is connected to a computer for data acquisition and processing.

To get the SPR spectrum response that is specific to Au nanoledge structures, a reference spectrum was obtained from a burnt box (with no nanoledge structure), and a dark spectrum was acquired from a region of the chip with no nanoledge or burnt box but a 250 nm thick Au film. The measured transmission spectra of the nanoslit sensor probe was thus obtained by the equation;[34]

$$Transmittace = \frac{(nanoledge\ intensity - dark\ intensity)}{(burnt\ box\ reference\ intensity - dark\ intensity)} x100\% \qquad (1)$$

Functionalization and Aptamer Immobilization

The immobilization of cTnI-aptamer at the plasmonic sensor surface is similar to a procedure previously reported.[40] First, the chip was subjected to thorough cleaning starting with ethanol rinse, followed by O_2 plasma cleaning (5min, 100W, 180mTorr O_2 pressure, -783 V DC bias; South Bay Technologies PC-2000 Plasma Cleaner), ethanol rinse, N_2 dry, and UV/ozone treatment using a bioforce UV/Ozone ProCleaner. Then, a SAM was formed by inserting the chip in a 25 mM solution of cystamine (containing 50% ethanol to enhance pact SAM on the Au chip) followed by a catalytic irradiation in a microwave synthesizer (50W, 50^{o}C) for 5 minutes. As a result, the two disulfide bonds within cystamine breaks to form two sulfur-Au bonds at the surface of the chip. After irradiation, the chip was rinsed with 90% ethanol then with DI water. Next, the chip was placed in a 2.5% glutaraldehyde solution and irradiated again (50W, 50^{o}C, 5 min) to facilitate the crosslink between amine functional groups of cystamine with the carbonyl functional groups in glutaraldehyde to form an imine bond. This leaves a terminal aldehyde group to which an amine modified TnI-aptamer can bind. The gold surface area that remains uncovered by the SAM was further capped by irradiating (50W, 50^{o}C) the chips in a solution containing 20 μM SH-PEG 500 for 5 minutes and washed thrice with DI water and N_2 dried. The sensors were then subjected to aptamer immobilization by drop casting 60 μL solution of the aptamer onto the sensing area and incubated at room temperature overnight. A wet Kimwipe in covered petri-dish was used to maintain chip humidity. After DI water rinse and N_2 dried, the chip was further incubated in a 0.2 M solution of glycine for 5 min to block unprotected carbonyl (C=O) groups on glutaraldehyde and washed with DI water, N_2 dried and stored at 4^{o}C until use.

Detection of cTnI Biomarker

After the immobilization of the aptamer, the NL-SPR sensor is ready for the detection of cTnI. A stock solution of 100 μg/mL of cTnI solution was spiked in a buffer, human serum and human whole blood to yield a working solution of different required concentrations. In order to probe the binding of cTnI to the aptamer modified surface, the tSPR method was carried out. First, the sensors were incubated in cTnI sample of concentration in the range between 0.0001 ng/mL-100 ng/mL for 20 min. Then, by analyzing the peak shift of tSPR at varying concentrations of cTnI in both biological and non-biological mediums, the local refractive index changes due to cTnI-aptamer interaction was obtained. Note that for each medium used, a reference tSPR was obtained without cTnI. To determine the specificity and selectivity of the aptasensor, similar approach to the one described above was used to develop a control experiment and obtained signals resulting from the presence of myoglobin, creatin kinase and heparin (0.156 ng/mL to 125 ng/mL) interferents in human serum. Myoglobin and creatin kinase were selected for this preliminary study because they are similar myocardial biomarkers to cTnI [21]. Heparin is a common treatment for blood cloth, and it was selected to determine if such treatment could interfere with the sensor's activity.

Estimation of Monolayer Thickness

The red shift in wavelength resulting from the increase in cTnI concentration (Figure 4.4) is taken to be due to the formation of a thin organic layer bound to the metal's surface. The thickness of the monolayer at different stages of the multi-layer formation is estimated based on the following general equation.[41]

$$\Delta\lambda = m(n_{adlayer} - n_{air})[exp(-2d_1/\mathrm{l_d}][1 - exp(-2d_2/l_d)] \qquad (1)$$

The SPR response, $\Delta\lambda,$ is defined as the shift in wavelength of the SPR maximum in transmitted light intensity associated with changes in refractive index of material due to adlayer formation at the metal surface, where m, is the sensitivity of the device measured in RIU (the slop of the calibration curve shown in Figure 4.3B), and $n_{adlayer}(cystamin = 1.58, glutaraldehyde = 1.433)$[34] are the RIs of the adsorbed molecular layer, d_1 is the thickness of first or intermediate layer and d_2 represent the thickness of the second or subsequent adsorbed layer, l_d is the SPR decay length. When the intermediate layer (for example cystamine, sandwiched between Au surface and glutaraldehyde) is very thin relative to l_d of the sensor, the dependence of l_d on RI approaches zero.[41] This mean that the influence of the intermediate layer on the responsivity of the sensor to the next added layer is negligible. Under such conditions, the parameter $exp(-\frac{2d_2}{l_d})$ in equation (1) approaches one. Hence, by rearranging equation (1), the relationship between $\Delta\lambda$ and adsorbed thickness, d, becomes;

$$d = (l_d/2)\{\frac{\Delta\lambda}{[(m(n_{SAM} - n_{air})]}\} \qquad (2)$$

To estimate the value of l_d, equation (2) was used to fit the experimental data as shown in Figure S4 Appendix B. The best fit was obtained using l_d=122.9 nm. A more accurate estimate of l_d comes from Maxwell's equation,[42] $l_d = (\lambda/2\pi)/\mathrm{Re}\{-\frac{n_{sample}^4}{n_{sample}^2+\varepsilon_{metal}}\}^{1/2}$. For the Au nanoledge sensor with dielectric constant ε_{metal}=1.526 at SPR maximum wavelength λ=803.56 in PBS of refractive index, $n_{sample} = 1.15$, the estimated l_d is 134.04 nm. The two estimates closely agree with each other. By using the value of l_d =134.04 nm, the adlayer thickness due to surface functionalization and cTnI binding to the probe at different concentrations was obtained.

REFERENCES

1. Negahdary, M., Behjati-Ardakani, M., Heli, H. & Sattarahmady, N. A cardiac troponin T biosensor based on aptamer selfassembling on gold. *Int. J. Mol. Cell. Med.* **8**, 271–282 (2019).
2. Han, X., Shokri Kojori, H., Leblanc, R. M. & Kim, S. J. Ultrasensitive Plasmonic Biosensors for Real-Time Parallel Detection of Alpha-L-Fucosidase and Cardiac-Troponin-I in Whole Human Blood. *Anal. Chem.* **90**, 7795–7799 (2018).
3. Madzharova, F., Heiner, Z., Simke, J., Selve, S. & Kneipp, J. Gold Nanostructures for Plasmonic Enhancement of Hyper-Raman Scattering. *J. Phys. Chem. C* **122**, 2931–2940 (2018).
4. Periyakaruppan, A., Gandhiraman, R. P., Meyyappan, M. & Koehne, J. E. Label-free detection of cardiac troponin-I using carbon nanofiber based nanoelectrode arrays. *Anal. Chem.* **85**, 3858–3863 (2013).
5. Santopolo, G. *et al.* Colorimetric Detection of Sepsis-Derived Hyperdegranulation with Plasmonic Nanosensors. *ACS Sensors* **6**, 4443–4450 (2021).
6. Ambartsumyan, O., Gribanyov, D., Kukushkin, V., Kopylov, A. & Zavyalova, E. SERS-based biosensors for virus determination with oligonucleotides as recognition elements. *Int. J. Mol. Sci.* **21**, 1–15 (2020).
7. Credi, C. *et al.* Fiber-cap biosensors for SERS analysis of liquid samples. *J. Mater. Chem. B* **8**, 1629–1639 (2020).
8. Zhang, J., Yan, Y., Miao, P. & Cai, J. Fabrication of gold-coated PDMS surfaces with arrayed triangular micro/nanopyramids for use as SERS substrates. *Beilstein J. Nanotechnol.* **8**, 2271–2282 (2017).
9. Lee, T. *et al.* Fabrication of troponin i biosensor composed of multi-functional dna structure/au nanocrystal using electrochemical and localized surface plasmon resonance dual-detection method. *Nanomaterials* **9**, (2019).
10. Liu, F. *et al.* Discrimination of Bulk and Surface Refractive Index Change in Plasmonic Sensors with Narrow Bandwidth Resonance Combs. *ACS Sensors* **6**, 3013–3023 (2021).
11. Lertvachirapaiboon, C., Baba, A., Ekgasit, S. & Shinbo, K. Biosensors and Bioelectronics Transmission surface plasmon resonance techniques and their potential biosensor applications. *Biosens. Bioelectron.* **99**, 399–415 (2018).
12. Ezendam, S. *et al.* Hybrid Plasmonic Nanomaterials for Hydrogen Generation and Carbon Dioxide Reduction. *ACS Energy Lett.* **7**, 778–815 (2022).
13. Yalavarthi, R. *et al.* Enhancing Photoelectrochemical Energy Storage by Large-Area CdS-Coated Nickel Nanoantenna Arrays. *ACS Appl. Energy Mater.* **4**, 11367–11376 (2021).
14. Zopf, D. *et al.* Plasmonic nanosensor array for multiplexed dna-based pathogen detection. *ACS Sensors* **4**, 335–343 (2019).
15. Udugama, B. *et al.* Diagnosing COVID-19: The Disease and Tools for Detection. *ACS Nano* **14**, 3822–3835 (2020).
16. Roth, G. A. *et al.* Global Burden of Cardiovascular Diseases and Risk Factors, 1990-2019: Update From the GBD 2019 Study. *J. Am. Coll. Cardiol.* **76**, 2982–3021 (2020).
17. Tsao, C. W. *et al. Heart Disease and Stroke Statistics-2022 Update: A Report from the American Heart Association*. *Circulation* vol. 145 (2022).
18. Tang, L., Yang, J., Wang, Y. & Deng, R. Recent Advances in Cardiovascular Disease Biosensors and Monitoring Technologies. *ACS Sensors* (2022)

doi:10.1021/acssensors.2c02311.

19. Moser, D. K. *et al.* Reducing delay in seeking treatment by patients with acute coronary syndrome and stroke: A scientific statement from the American Heart Association Council on Cardiovascular Nursing and Stroke Council. *Circulation* **114**, 168–182 (2006).
20. Mcdonnell, B., Hearty, S., Leonard, P. & Kennedy, R. O. Cardiac biomarkers and the case for point-of-care testing. *Clin. Biochem.* **42**, 549–561 (2009).
21. T, R. *et al.* On the Detection of cTnI - A Comparison of Surface-Plasmon Optical -, Electrochemical -, and Electronic Sensing Concepts. *Ann. Clin. Med. Case Reports* **06**, (2021).
22. Stepinska, J. *et al.* Diagnosis and risk stratification of chest pain patients in the emergency department: focus on acute coronary syndromes. A position paper of the Acute Cardiovascular Care Association. *Eur. Hear. J. Acute Cardiovasc. Care* **9**, 76–89 (2020).
23. Kott, K. A. *et al.* Biomarker Development in Cardiology: Reviewing the Past to Inform the Future. *Cells* **11**, 1–27 (2022).
24. Alaour, B., Liew, F. & Kaier, T. E. Cardiac Troponin - diagnostic problems and impact on cardiovascular disease. *Ann. Med.* **50**, 655–665 (2018).
25. Anand, A. *et al.* High-Sensitivity Cardiac Troponin on Presentation to Rule out Myocardial Infarction: A Stepped-Wedge Cluster Randomized Controlled Trial. *Circulation* 2214–2224 (2021) doi:10.1161/CIRCULATIONAHA.120.052380.
26. Lazar, D. R. *et al.* High-Sensitivity Troponin: A Review on Characteristics, Assessment, and Clinical Implications. *Dis. Markers* **2022**, 1–13 (2022).
27. Wu, Y. *et al.* Diagnostic and Prognostic Biomarkers for Myocardial Infarction. *Front. Cardiovasc. Med.* **7**, 1–13 (2021).
28. Immunoassay, E. & Cummins, B. Cardiac Specific Troponin-I Release in Canine Experimental Myocardial Infarction : Development of a Sensitive (Received 9 March 1987 , accepted in revised form 13 August 1987). **1010**, 999–1010 (1987).
29. PATHFAST. *PATHFAST TM hs-cTnI : early and immediate diagnosis of MI in the emergency department (ED) Clinical benefits of hs-cTn assays High Sensitive troponin I*. https://www.phchd.com/eu/-/media/biomedical/europe/Marketing_materials/Product_flyers/Pathfast/hs_Troponin_I_Brochure/PF_Folder_hs_Troponin_EN.pdf?rev=46b215193a0349aca592d85c58d60a4d.
30. Radiometer. Point-of-care biomarker testing made simple.
31. Palladino, P., Minunni, M. & Scarano, S. Cardiac Troponin T capture and detection in real-time via epitope-imprinted polymer and optical biosensing. *Biosens. Bioelectron.* **106**, 93–98 (2018).
32. Lopa, N. S. *et al.* Simple , low-cost , sensitive and label-free aptasensor for the detection of cardiac troponin I based on a gold nanoparticles modi fi ed titanium foil. *Biosens. Bioelectron.* **126**, 381–388 (2019).
33. Yang, X. *et al.* Chemical Electrogenerated chemiluminescence biosensor array for the detection of multiple AMI biomarkers. *Sensors Actuators B. Chem.* **257**, 60–67 (2018).
34. Maud Savonneta, Tristan Rolland, Myriam Cubizolles, Yoann Roupioz, A. B. Recent advances in cardiac biomarkers detection: From commercial devices to emerging technologies. *J. Pharm. Biomed. Anal.* 113777 (2020) doi:10.1016/j.jpba.2020.113777.
35. Sinha, A., Tai, T., Li, K., Gopinathan, P. & Chung, Y. An integrated microfluidic system with field-effect-transistor sensor arrays for detecting multiple cardiovascular biomarkers from clinical samples ☆. *Biosens. Bioelectron.* **129**, 155–163 (2019).

36. Jo, H. *et al*. Electrochemical Aptasensor of Cardiac Troponin I for the Early Diagnosis of Acute Myocardial Infarction. *Anal. Chem.* (2015) doi:10.1021/acs.analchem.5b02312.
37. Jo, H., Her, J., Lee, H., Shim, Y. & Ban, C. Highly sensitive amperometric detection of cardiac troponin I using sandwich aptamers and screen-printed carbon electrodes. *Talanta* **165**, 442–448 (2017).
38. Kumar, D., Kandpal, M. & Surya, S. G. Characterization and detection of cardiac Troponin-T protein by using ‘ aptamer ’ mediated biofunctionalization of ZnO thin- fi lm transistor. *Appl. Surf. Sci.* **466**, 874–881 (2019).
39. Kurt, H., Eyüpoğlu, A. E., Sütlü, T., Budak, H. & Yüce, M. Plasmonic Selection of ssDNA Aptamers against Fibroblast Growth Factor Receptor. *ACS Comb. Sci.* **21**, 578–587 (2019).
40. Zheng, F., Ke, W., Shi, L., Liu, H. & Zhao, Y. Plasmonic Au-Ag Janus Nanoparticle Engineered Ratiometric Surface-Enhanced Raman Scattering Aptasensor for Ochratoxin A Detection. *Anal. Chem.* **91**, 11812–11820 (2019).
41. Portela, A., Calvo-Lozano, O., Estevez, M., Medina Escuela, A. & Lechuga, L. M. Optical nanogap antennas as plasmonic biosensors for the detection of miRNA biomarkers. *J. Mater. Chem. B* **8**, 4310–4317 (2020).
42. Altug, H., Oh, S., Maier, S. A. & Homola, J. Advances and applications of nanophotonic biosensors. **17**, (2022).
43. Lee, K. L., Huang, J. Bin, Chang, J. W., Wu, S. H. & Wei, P. K. Ultrasensitive biosensors using enhanced fano resonances in capped gold nanoslit arrays. *Sci. Rep.* **5**, 1–9 (2015).
44. Andam, N., Refki, S., Hayashi, S. & Sekkat, Z. Plasmonic mode coupling and thin film sensing in metal – insulator – metal structures. *Sci. Rep.* 1–12 (2021) doi:10.1038/s41598-021-94143-2.
45. Ghayoor, R., Zangenehzadeh, S. & Keshavarz, A. Design of High - Sensitivity Surface Plasmon Resonance Sensor Based on Nanostructured Thin Films for Effective Detection of DNA Hybridization. *Plasmonics* 1831–1841 (2022) doi:10.1007/s11468-022-01669-w.
46. Rossi, S., Gazzola, E., Capaldo, P., Borile, G. & Romanato, F. Grating-Coupled Surface Plasmon Resonance (GC-SPR) Optimization for Phase-Interrogation Biosensing in a Microfluidic Chamber. *Sensors* **18**, (2018).
47. Yesudasu, V., Shekhar, H. & Jasvanthbhai, R. Recent progress in surface plasmon resonance based sensors : A comprehensive review. *Heliyon* **7**, e06321 (2021).
48. Austin Suthanthiraraj, P. P. & Sen, A. K. Localized surface plasmon resonance (LSPR) biosensor based on thermally annealed silver nanostructures with on-chip blood-plasma separation for the detection of dengue non-structural protein NS1 antigen. *Biosens. Bioelectron.* **132**, 38–46 (2019).
49. Das, C. M. *et al.* In-Depth Conceptual Study of an Enhanced Plasmonic Sensing System Using Antire fl ective Coatings and Perovskites for the Detection of Infectious Viral Antigens. (2022) doi:10.1021/acsaelm.2c00017.
50. Daniel, S. & Bawuah, P. Plasmonic Implanted Nanogrooves for Optical Beaming. *Sci. Rep.* 2–9 (2019) doi:10.1038/s41598-018-37202-5.
51. Koteswara Rao, V. Point of Care Diagnostic Devices for Rapid Detection of Novel Coronavirus (SARS-nCoV19) Pandemic: A Review. *Front. Nanotechnol.* **2**, 1–9 (2021).
52. Mauriz, E. Recent progress in plasmonic biosensing schemes for virus detection. *Sensors (Switzerland)* **20**, 1–27 (2020).
53. Sanders, M., Lin, Y., Wei, J., Bono, T. & Lindquist, R. G. An enhanced LSPR fiber-optic

nanoprobe for ultrasensitive detection of protein biomarkers. *Biosens. Bioelectron.* **61**, 95–101 (2014).

54. Lee, T. *et al.* Development of the troponin detection system based on the nanostructure. *Micromachines* **10**, (2019).
55. Liu, G. Grand Challenges in Biosensors and Biomolecular Electronics. **9**, 1–5 (2021).
56. Shrivastav, A. M., Cvelbar, U. & Abdulhalim, I. A comprehensive review on plasmonic-based biosensors used in viral diagnostics. *Commun. Biol.* **4**, 1–12 (2021).
57. Bethe, H. A. Theory of Diffraction by Small Holes. *Phys. Rev.* **66**, (1944).
58. Ebbesen, T. W., Lezec, H. J., Ghaemil, H. F., Thiol, T. & Wolff, P. A. Extraordinary optical transmission through sub-wavelength hole arrays. *Nature* **391**, 667–669 (1998).
59. Martín-Moreno, L. *et al.* Theory of extraordinary optical transmission through subwavelength hole arrays. *Phys. Rev. Lett.* **86**, 1114–1117 (2001).
60. Wei, J., Waldeck, D. H., Kofke, M. & Singhal, S. JSM Nanotechnology & Nanomedicine A Study of Localized Surface Plasmon Resonance Nanoslit Array and Applications for Chip-based Protein Detection. *JSM Nanotechnol Nanomed* **2**, 1–8 (2014).
61. Zeng, B., Gao, Y. & Bartoli, F. Ultrathin plasmonic nanogratings for rapid and highly-sensitive detection. 1–11.
62. Zeng, Z. *et al.* Protein Trapping in Plasmonic Nanoslit and Nanoledge Cavities: The Behavior and Sensing. *Anal. Chem.* **89**, 5221–5229 (2017).
63. Monolayer, T. S. coatings. 1–10 (2019).
64. Bagra, B., Mabe, T., Tukur, F. & Wei, J. A plasmonic nanoledge array sensor for detection of anti-insulin antibodies of type 1 diabetes biomarker. *Nanotechnology* **31**, (2020).
65. Lee, S. & Kang, S. H. Quenching effect on gold nano-patterned cardiac troponin i chip by total internal reflection fluorescence microscopy. *Talanta* **104**, 32–38 (2013).
66. Tukur, F. *et al.* Plasmon–Exciton Coupling Effect in Nanostructured Arrays for Optical Signal Amplification and SARS-CoV-2 DNA Sensing. *ACS Appl. Nano Mater.* **6**, 2071–2082 (2023).
67. Mei, C. *et al.* An ultrasensitive reusable aptasensor for noninvasive diabetic retinopathy diagnosis target on tear biomarker. *Sensors Actuators, B Chem.* **345**, 130398 (2021).
68. Jung, L. S., Campbell, C. T., Chinowsky, T. M., Mar, M. N. & Yee, S. S. Quantitative interpretation of the response of surface plasmon resonance sensors to adsorbed films. *Langmuir* **14**, 5636–5648 (1998).
69. Johnston, K. S., Karlsen, S. R., Jung, C. C. & Yee, S. S. New analytical technique for characterization of thin films using surface plasmon resonance ’. **42**, 242–246 (1995).
70. Lee, C.-Y., Gamble, L. J., Grainger, D. W. & Castner, D. G. Mixed DNA/oligo (ethylene glycol) functionalized gold surfaces improve DNA hybridization in complex media. *Biointerphases* **1**, 82–92 (2006).
71. Stringer, R. C., Hoehn, D. & Grant, S. A. Quantum Dot-Based Biosensor for Detection of Human Cardiac Troponin I Using a Liquid-Core Waveguide. *IEEE Sens. J.* **8**, 295–300 (2008).
72. Bhalla, N. & Estrela, P. Exploiting the signatures of nanoplasmon-exciton coupling on proton sensitive insulator-semiconductor devices for drug discovery applications. *Nanoscale* **10**, 13320–13328 (2018).
73. Wu, Q. *et al.* Ultrasensitive magnetic field-assisted surface plasmon resonance immunoassay for human cardiac troponin I. *Biosens. Bioelectron.* **96**, 288–293 (2017).

74. Kwon, Y. C. *et al.* Development of a surface plasmon resonance-based immunosensor for the rapid detection of cardiac troponin I. *Biotechnol. Lett.* **33**, 921–927 (2011).

75. Ashaduzzaman, M. *et al.* On/off-switchable LSPR nano-immunoassay for troponin-T. *Sci. Rep.* **7**, 1–10 (2017).

CHAPTER V: CONCLUSION AND FUTURE CONSIDERATION

This research study was undertaken to address key scientific challenges impacting the development of plasmonic point-of-care devices. The primary goal was to develop new scientific solutions and implement them to create portable biosensors for disease testing and monitoring. Within this dissertation, alternative architectures and procedures were developed and implemented to deal with the problems associated with repeatable synthesis of uniform nanomaterials, complex nanostructure fabrication, low SPR generation efficiency and limited understanding of the mechanism of plasmon-exciton coupling for signal amplification. The theme of the work centres around the design, fabrication, and optimization of metal nanostructures that could enhance diagnostic sensitivity via surface plasmon resonance (SPR) generation. Emphasis was placed on investigating the mechanism of optical signal enhancement arising from plasmon-exciton coupling (PEC) with particular focus on (a) exploring the role of geometry and size of the nanostructures (b) examining the influence of SPR spectral mode overlap with exciton’s absorption and/or emission energies on the overall optical signal in a metal nanostructures, and (c) investigating the analytical sensitivity and signal transduction of the PEC system to biomolecular interactions. Findings from these undertakings as reported in Chapters I and II are highlighted below.

In Chapter III, after designing and simulating a nanoslit array for its optical properties, a simple lithography technique was used for its fabrication on a flexible PDMS substrate. Undoubtedly, the soft nanoimprinting route provided an extraordinary path to achieving a uniform and scalable patterned substrate. A single patterned template created via the direct writing method (FIB or EB) lithography was all it took to make more than fifteen PDMS-based, high aspect-ratio patterned devices. This saved time and fabrication cost. Their geometry dependent SPR mode in reflection show tunability over the visible wavelength range. This played an important role in investigating the mechanism of optical enhancement via plasmon-exciton coupling. Since spectral overlap of SPR mode with an emitters absorption and emission energy is the mechanism found for optical enhancement in the nanoslit, the achieved modulation of the SPR mode will allow a plethora of emitting species to be employed for signal amplification via PEC. Acridine Orange dye was coupled with SPR in a 50 nm slit and achieved a 57x optical signal enhancement. The coupled system showed sensitivity not only to SARS-CoV-2 DNA hybridization at 0.21 nM, but also to a single DNA-base mismatch. The biosensor is stable and can be reused for up to six times.

In Chapter IV, I reported the implementation of a nanoledge structure for detecting a cardiovascular disease biomarker, Troponin I (TnI) spiked in PBS buffer, human serum (HS), and human blood (HB) mediums. The nanoledge device exhibits high sensitivity for the detection of cTnI over a wide range of concentrations (0.0001 to 100 ng/mL) with an excellent detection limit of 0.079, 0.084, 0.097 ng/mL in phosphate buffer saline, human serum, and human whole blood, respectively. A remarkable selectivity against interferents such as myoglobin, creatin kinase and heparin was achieved by modifying the sensor with specific cTnI aptamers. The superior performance characteristic arises from the extraordinary transmission through the nanoledge structure and the selectivity of the recognition element leading to an optical signal that is highly sensitive to small changes in refractive index. Considering the high sensitivity towards cTnI in different biological mediums, this plasmonic device can help lead to breakthroughs in the development a point-of-care-testing tool for future clinical use.

Thus, this work innovates (a) a tunable SPR to meet the requirement for plasmon-exciton spectral overlap for optical signal amplification, (b) the mechanism of optical enhancements due to PEC in NS arrays, and (c) a new application of PEC in NS and EOT in NL for the sensitive detection of SARS-CoV-2 DNA hybridization and cardiovascular biomarker TnI in human blood, respectively. The enhanced light-matter interactions have a broader impact beyond healthcare to light harvesting for solar cells, heat generation for cancer therapy, and photocatalysis for nanoscale reactions like water splitting. However, the detailed role of the orientation and intrinsic quantum yield of emitters on the mechanism of optical enhancement in PEC has not been fully clarified. Moreover, research efforts should be devoted to developing a method of extracting surface plasmon-coupled emission from a surface to the far field.

APPENDIX A: PLASMON-EXCITON COUPLING IN NANOSLIT ARRAYS FOR SIGNAL AMPLIFICATION AND BIOSENSING

Scheme. S1. a) Fabrication steps: Au coated nanoslit structure on PDMS via soft lithographic pattern transfer. b) show the SEM images for the optimization of the nanoslit array design at PDMS baking temperatures ranging between 35^{o}C and 100^{o}C for 1 hour

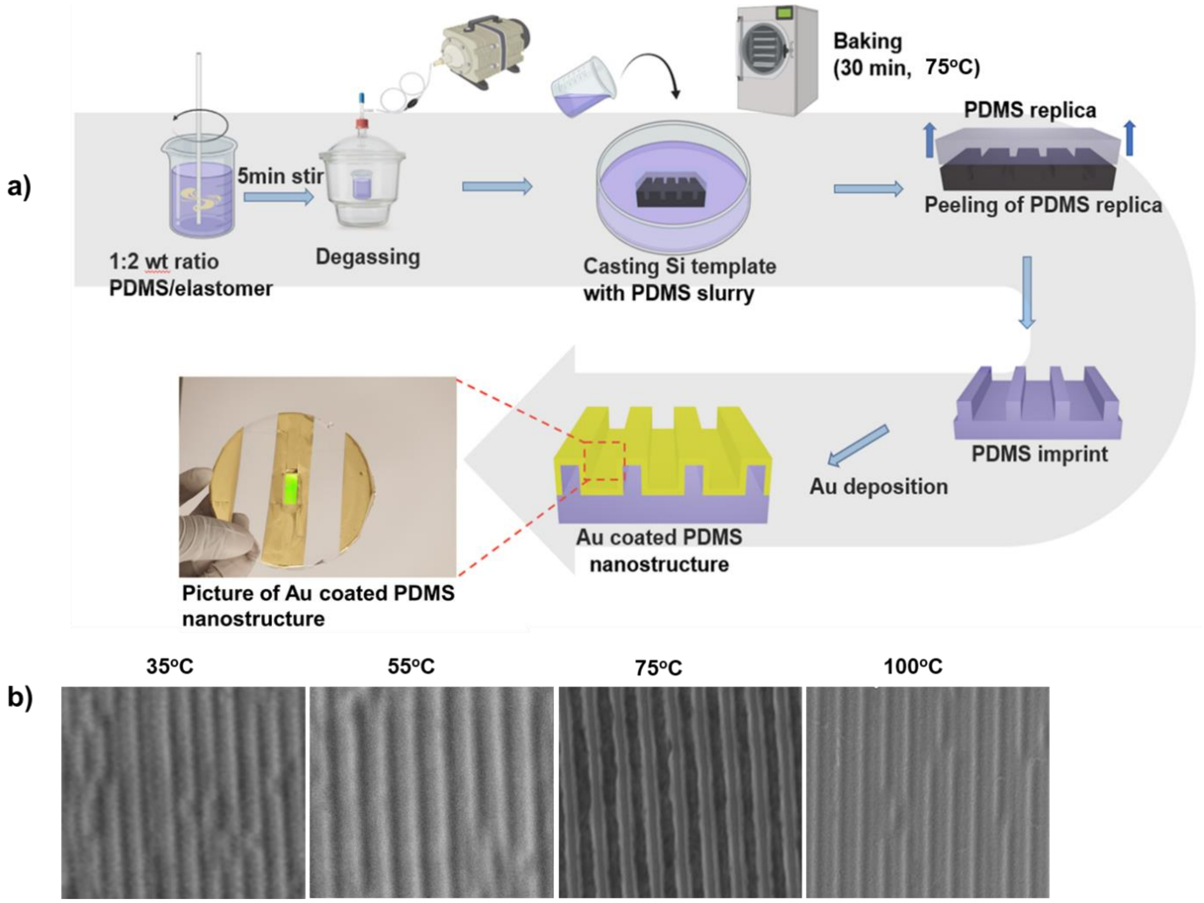

Fig. S1: SEM images of fabricated nanoslit array of width (a) 55.38 nm (b) 73.6 nm (c) 90.1 nm (d) 115.2 nm (e) 135 nm (f) show the linear relation between the measured gold film thickness (45.38 nm, 35.27 nm, 25.25 nm, 15.11 nm, 5.36 nm) with the nanoslit width

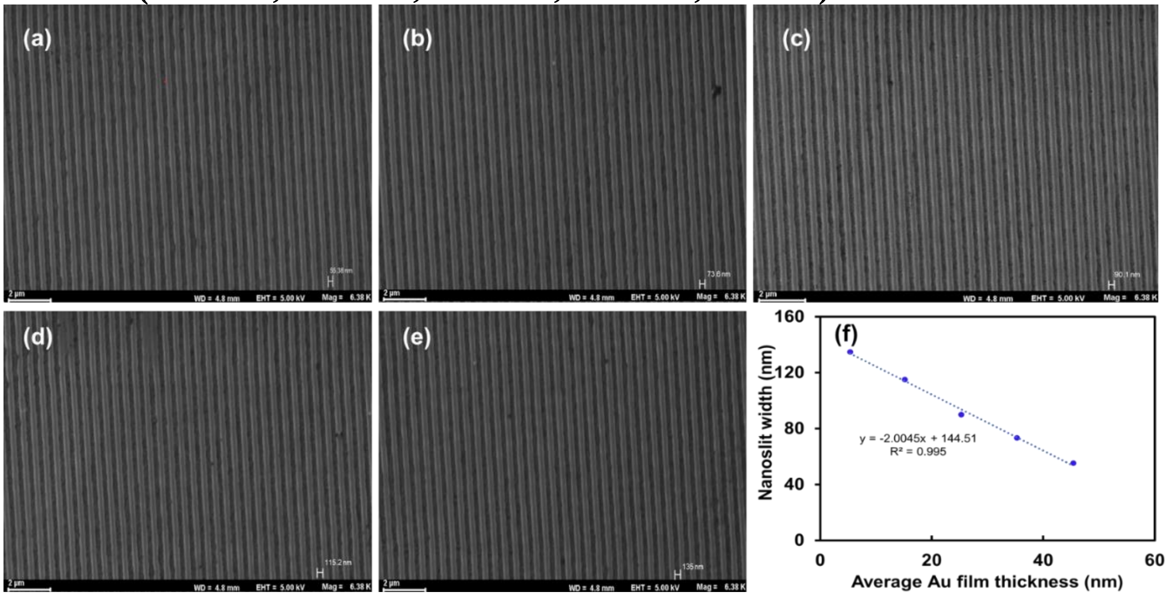

Fig. S2. Representative EM-field distribution images from FDTD simulations. We simulated a design without and with an Au film at the slit bottom. (a) shows the electric field, $|E|^2$ $(V/m)^2$ distribution in nanoslit without a gold base and (b-e) nanoslits with gold film base of different thicknesses

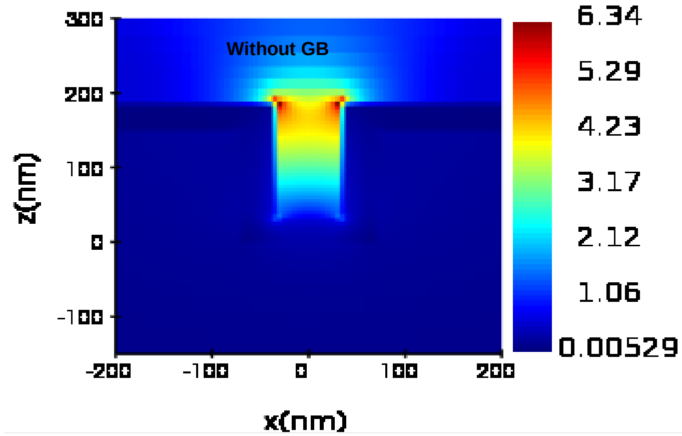

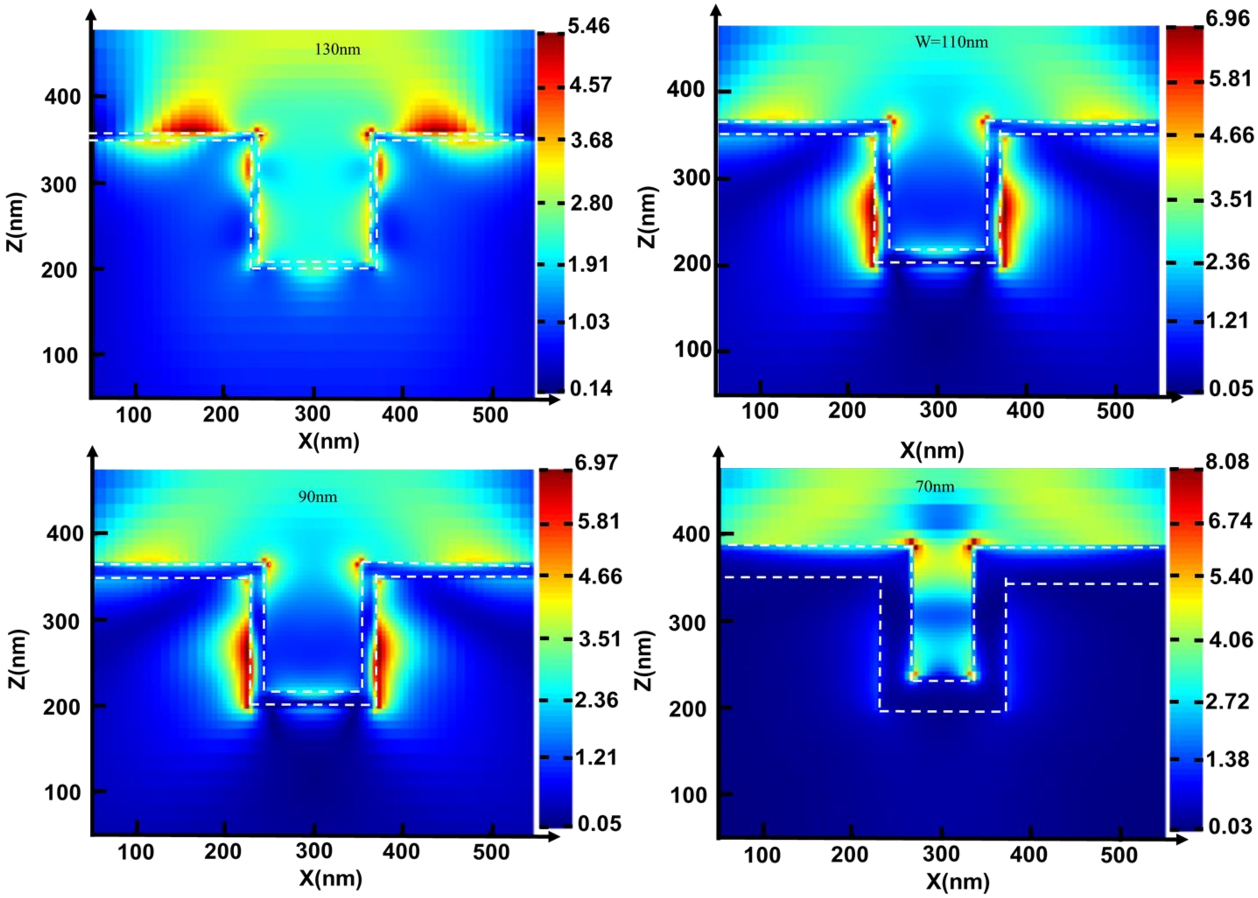

Fig. S3. The correlation between SPGE, simulated and measured EM-field as a function of slit width. Detailed description is provided in the section: semi-analytical modeling

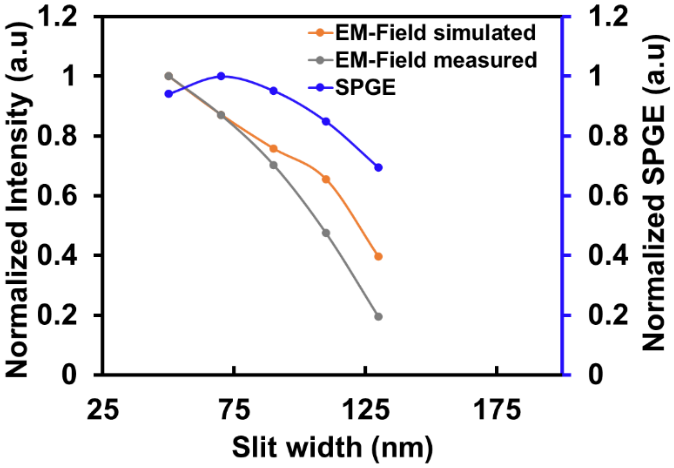

Fig. S4. Net reflectance intensity spectra of (a) AO (b) PI and (c) DHE in different nanoslit structures

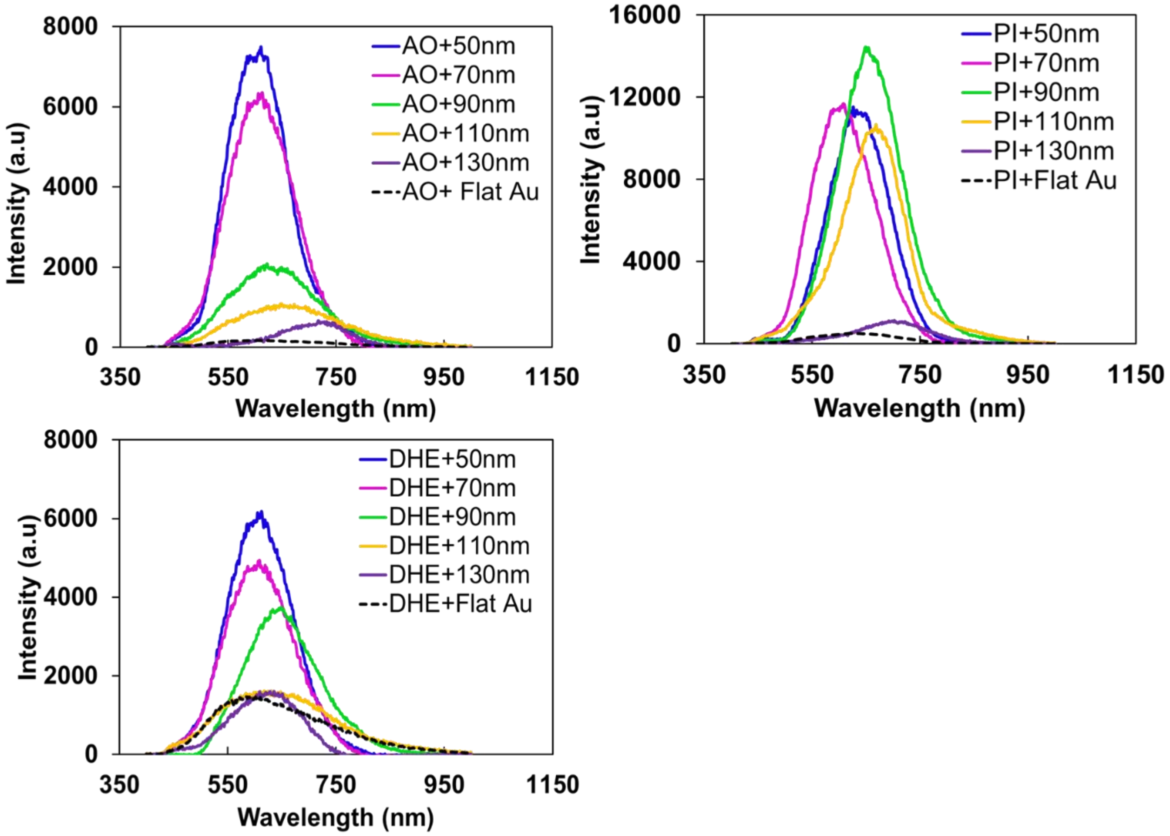

Fig S5. Normalized spectral overlap between the excitation and emission spectrum of AO, PI and DHE with reflection spectrum of nanoslits of widths 50 nm, 70 nm, 90 nm, 110 nm, and 130 nm respectively

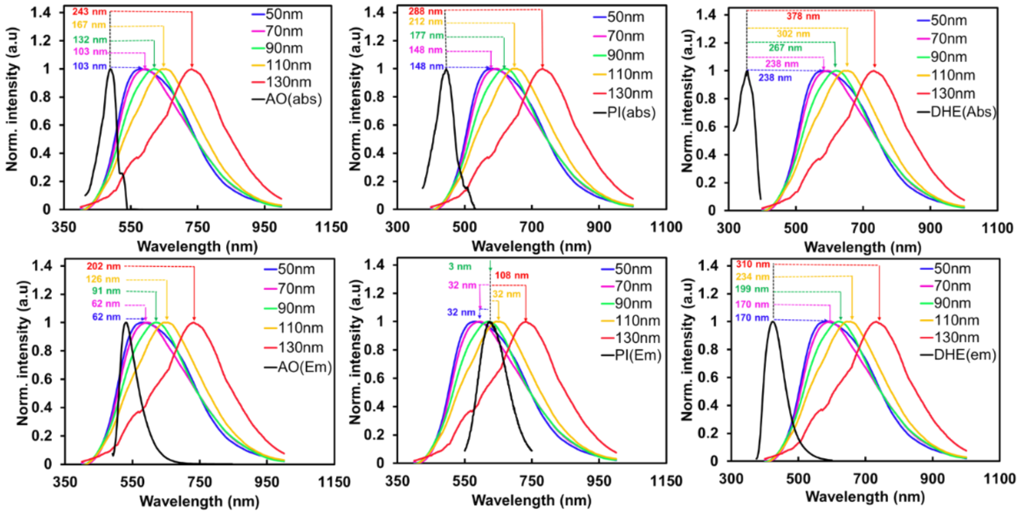

Fig. S6. (A) Cytoviva spectra of AO, AO and ssDNA probe in the presence and absence of ct-DNA at 110 nm nanoslit array; (B) The spectra of ssDNA directly in the nanoslits without a dye. The blank is a PBS buffer solution without ssDNA

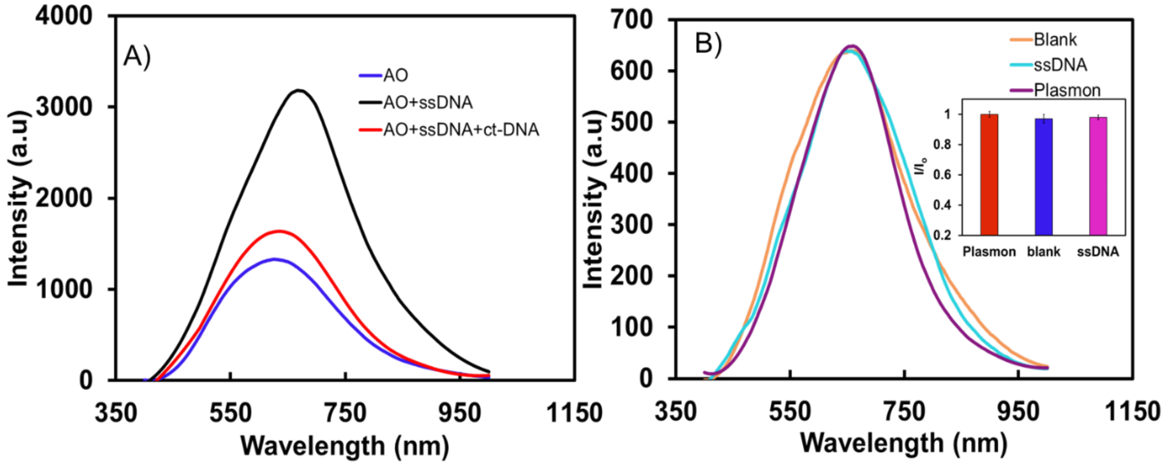

Fig S7. Effect of below-equilibrium concentration of acridine-ssDNA complex on intensity signal response. Ideally, the hybridization of ssDNA with its complementary strand in the presence of surface acridine is expected to cause signal intensity reduction (A) because acridine emits at a shorter wavelength (525 nm) in the presence of a double strand DNA. Since the emission spectrum of the dye is far away from plasmon resonance energy excited in the nanoslit, plasmon-exciton coupling efficiency is diminished and hence the quenching effect. However, figure (B) shows an enhancement in intensity by adding ctDNA to the surfaces where 4 µM of ssDNA probe was used in forming the ssDNA-AO substrate. This could be the result of a direct binding of ct-DNA to free acridine at the surface.

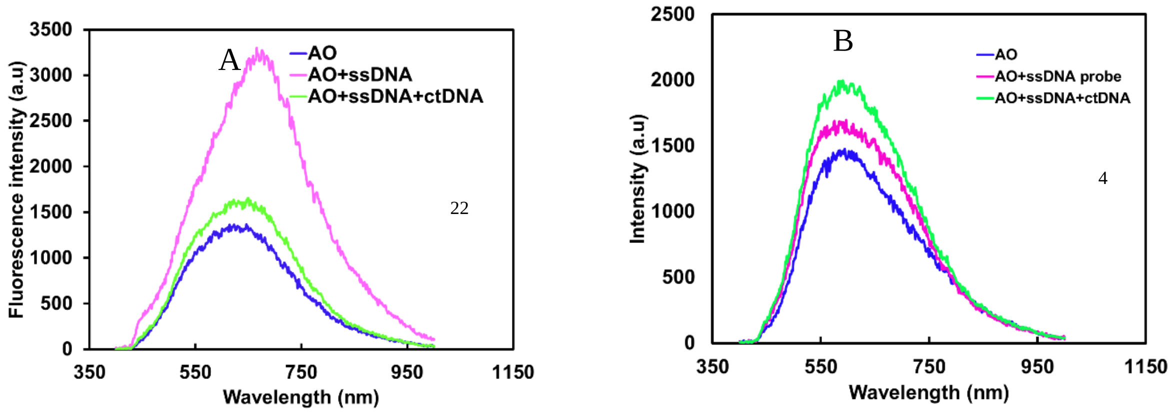

Fig. S8. Axio Z2M images and corresponding RGB intensity profile of (A). AO, (B) AO-ssDNA and (C) AO-dsDNA illuminated at 430nm

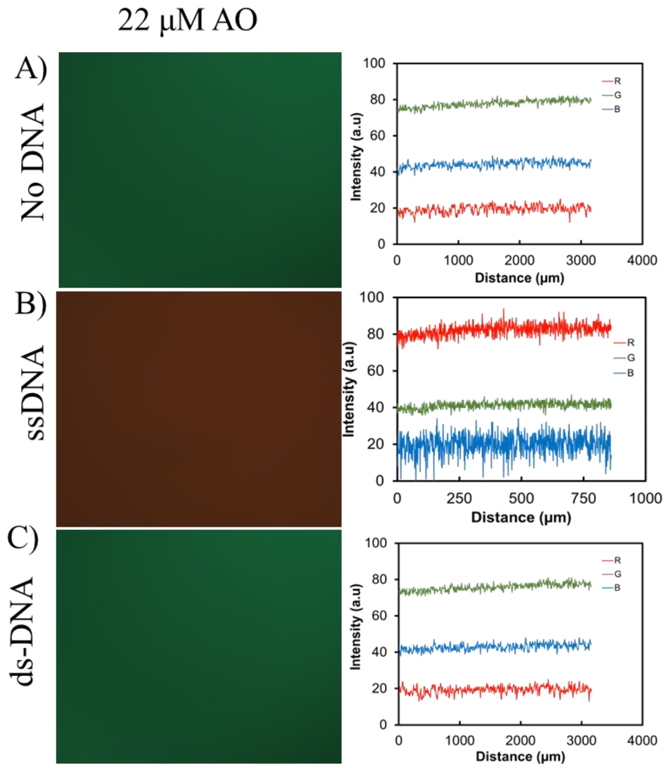

Fig. S9. A) The stability of sensor after 10 days storage. B) the reusability of the sensor after 6 regeneration cycles

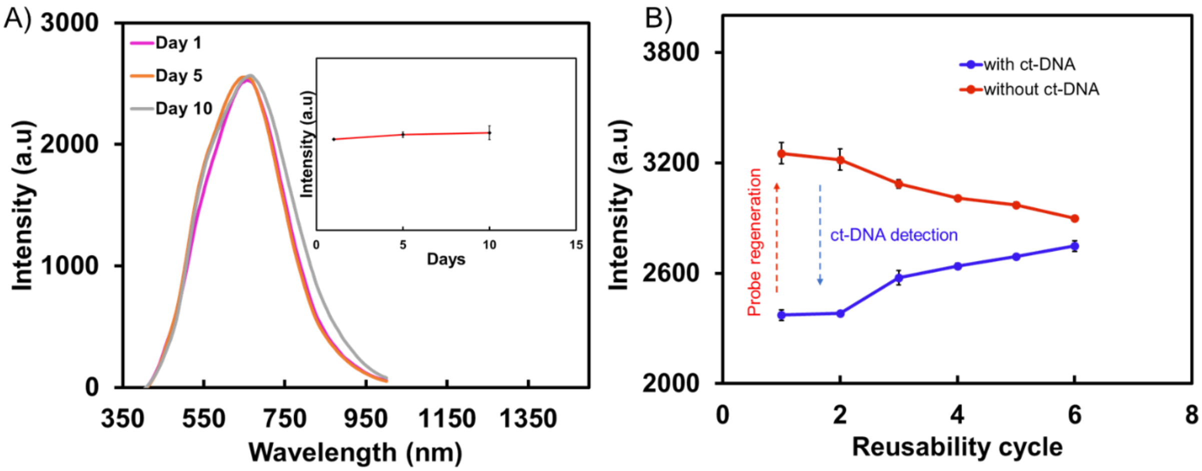

Fig. S10. Surface plasmon polariton generation efficiencies as a function of the slit width for different wavelength. Inset show the exponential decay of SPGE with increasing wavelength for different slit width

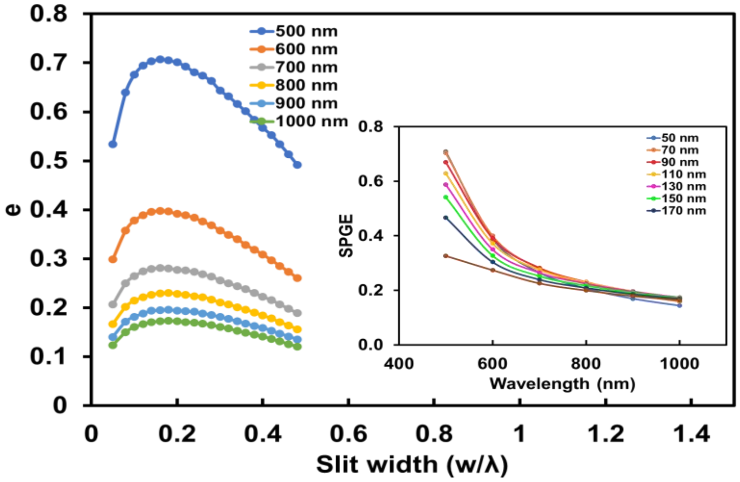

Semi-analytical Modelling: Here, surface plasmon polariton efficiency taken to be the result of geometric diffraction and launching of bounded SPP modes on the flat interfaces surrounding the nanoslit. The signature of SPP-mode excitations was quantitatively recognized based on completeness theorem which offers useful information on the efficiency of SPP generation. For light propagating in a non-translational system, the transverse field pattern can be treated as a linear combination of forward- and backward-travelling bounded and radiative modes (Scheme S2).[1-3] Therefore, the SPP generation efficiency *e* of the transverse electromagnetic fields for our slit geometry and for w/2 <x and x<-w/2 were estimated from equations 1-2. Note that $e_1=e_2$ since in both cases one encounters Au/air interfaces, and the overall efficiency can be taken to be e_1+e_2. Here we took account of the normalized SPP excitation strength $(|\alpha^{+}(x)|^2$ and $(|\alpha^{+}(x)|^2$ for -w/2<x<w/2, since there is air-metal interface. Note that the field inside the slit consist of the downward and upward-reflected fundamental modes since we are dealing with light diffraction by slit arrays.

$$e_1 = |\alpha_1^+(w/2)|^2 = |\alpha_1^-(w/2)|^2$$

$$= \frac{4\,w'n_1^3}{\pi n_2^2}\,|\frac{\varepsilon^{1/2}}{\varepsilon + n_1^2}|\,|\frac{I_o}{1 + (n_1/n_2)w'I_o}|^2 \qquad (1)$$

$$e_2 = |\alpha_2^+(w/2)|^2 = |\alpha_2^-(w/2)|^2$$

$$= \frac{4\,w'n_1^3}{\pi n_1^2}\,|\frac{\varepsilon^{1/2}}{\varepsilon + n_2^2}|\,|\frac{I_o}{1 + (n_2/n_1)w'I_o}|^2 \qquad (2)$$

Where n_1, n_2, and n_3 are the refractive indices of the top Au-air and in-slit Au-air interfaces. Note that $n_1 = n_2 = 1$. The normalized slit width is given by, $w' = nw/\lambda$ where w is the slit width. The integrals I_1 and I_o were calculated numerically for different w' and ε for Au at different wavelengths.

Scheme S2. The Schematic illustrating the parameters for the nanoslit structure and surface plasmon generation under plane wave illumination at normal incidence

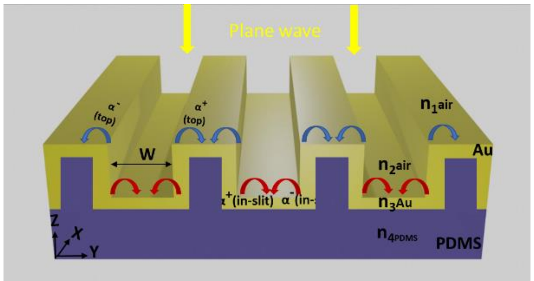

Equations (1 and 2) represent the semi-analytical expressions for SPP excitation efficiency when the slit channel is illuminated by fundamental slit mode. All plots were relative to the SPP excitation efficiency e_2 inside the slit. The efficiencies were obtained over a broad range of wavelength (500-1000nm).

Table S1a. Percentage decrease in intensity and intensity enhancement factor calculated for different nanoslit widths with respect to the 50 nm slit width. The intensity values used is shown in Table S1b. I_{50} and I_x are the intensities in W=50 nm and other slit width structures respectively

% Drop in intensity $\Delta \mathbf{I}(\%) = \frac{I_{50} - I_x}{(I_{50} + I_x)/2} * 100$	**No dye**	**AO**	**PI**	**DHE**
W (nm)	ΔI_p	ΔI_{pd}(a.u)	ΔI_{pd}(a.u)	ΔI_{pd}(a.u)
50				
70	13%	16%	3%	31%
90	53%	102%	14%	141%
110	87%	137%	16%	160%
130	147%	165%	163%	184%

Table S1b: Measured scattering intensities on nanostructure area and plain Au surface with and without dye and the corresponding intensity enhancement factor

Plasmon and Control peak intensity	**No dye**		**With AO**		**With PI**		**With DHE**		**Intensity enhancement, I_E** $I_E = \frac{I_{pd} - I_p}{I_{cd} - I_c}$		
W (nm)	I_p(a.u)	I_c(a.u)	I_{pd} (a.u)	I_{cd} (a.u)	I_{pd} (a.u)	I_{cd} (a.u)	I_{pd} (a.u)	I_{cd} (a.u)			
Control (plain Au)		43.02		171.62		512.79		2409.68	**AO**	**PI**	**DHE**
50	1645.25		8965.39		13098		6241.166		56.92	24.42	1.94
70	1445.19		7651.33		12777.00		4588.16		48.25	24.12	1.32
90	946.90		2930.92		15044.31		1081.05		15.43	30.01	0.06
110	644.49		1669.58		11113.39		692.71		7.97	22.28	0.02
130	253.05		861.09		1327.56		267.48		4.72	2.29	0.01

Note. Ip = intensity of nanostructure without dye; Ic= intensity of plain Au surface without dye
Ipd = intensity of nanostructure with dye; Icd=intensity of plain Au with dye

I_E=reflectance intensity enhancement factor

Table S2. Sensitivity of existing biosensors for SARS-CoV-2 testing

Methods	Transducer	Target	Detection limit	Detection time
ELISA[4-5]		SARS-CoV-2 IgG in serum	1.953 ng/mL	5h
Photoluminescence spectroscopy[6]	Semiconductor polymer	SARS-CoV-2 IgG in serum	0.0125 μg/mL	
SPR[7]	Gold film	S protein	0.08 pg/mL	<1 min
Fluorescence[8]	Fluorescent probe	SARS-CoV-2 E & N gene	10 copies/μL	30-40 min
colorimetric[9]	fluorescein dye	SARS-CoV-2	12 copies/ reaction	60 min
Colorimetric/SPR[10]	QD/Au Npcs	SARS-CoV-2 N-gene RNA	0.18 ng/ μL	10min
EFT[11]	Graphene	SARS-CoV-2 in PBS	1 fg/mL	<2 min
Electrochemical[12]	Electrode	SARS-CoV-2 N & S genes	1 copy/ μL	<2 hours
Electrochemical[13]	electrodes	SARS-CoV-2 antibody in saliva	2.3 RNA copies/ μL	50 min
SPR[14]	Au nanocup array	SARS-CoV-2 antigen in saliva	370 vp/mL	15 min
SPR[15]	Au nanoislands	SARS-CoV-2 specific sequence	0.22 pM	

Table S3. Numerical data of I_0 and I_1 for different values of w' for gold at different wavelengths. Note that I_0 is same for Au at varying wavelengths

		400 nm ε=-1.66 + 5.74j	500 nm ε=2.5676 +3.6391j	600 nm ε=-9.3875 +1.5292j	700 nm ε=-16.486 + 1.0643j	800 nm ε=-24.061 + 1.5068j	900 nm ε=-32.719 + 1.9955j	1000 nm ε=-41.849 + 2.9477j
'	I_o	I_1	I_1	I_1	I_1	I_1	I_1	I_1
.05	3.13-5.52j	-0.44-3.53j	-0.68-3.33j	-0.20-2.99j	-0.02-3.02j	0.07-3.05j	0.13-3.06j	0.17-3.07j
.08	3.11-4.54j	-0.17-3.50j	-0.41-3.30j	0.07-2.93j	0.25-2.96j	0.34-2.98j	0.40-3.00j	0.44-3.00j
.1	3.09-4.09j	0.01-3.46j	-0.24-3.27j	0.23-2.88j	0.42-2.90j	0.51-2.92j	0.57-2.93j	0.62-2.94j
.12	3.07-3.73j	0.19-3.41j	-0.07-3.23j	0.39-2.82j	0.58-2.84j	0.67-2.85j	0.74-2.86j	0.78-2.87j
.14	3.04-3.37j	0.36-3.35j	0.10-3.17j	0.55-2.75j	0.74-2.76j	0.83-2.77j	0.90-2.78j	0.95-2.78j
.16	3.01-3.07j	0.53-3.28j	0.26-3.11j	0.69-2.67j	0.88-2.67j	0.98-2.68j	1.05-2.68j	1.10-2.68j
.18	2.98-2.81j	0.69-3.21j	0.41-3.04j	0.83-2.58j	1.02-2.57j	1.12-2.58j	1.19-2.58j	1.24-2.58j
.2	2.94-2.61j	0.84-3.12j	0.55-2.97j	0.96-2.48j	1.15-2.46j	1.25-2.47j	1.32-2.46j	1.37-2.46j
.22	2.90-2.39j	0.99-3.02j	0.69-2.88j	1.08-2.38j	1.27-2.35j	1.37-2.35j	1.44-2.34j	1.49-2.33j
.24	2.86-2.18j	1.13-2.91j	0.82-2.78j	1.19-2.27j	1.38-2.23j	1.48-2.22j	1.55-2.21j	1.60-2.20j
.26	2.81-1.99j	1.26-2.80j	0.95-2.68j	1.28-2.15j	1.47-2.10j	1.58-2.09j	1.64-2.07j	1.69-2.06j
.28	2.77-1.82j	1.37-2.68j	1.06-2.58j	1.37-2.03j	1.56-1.97j	1.66-1.95j	1.73-1.93j	1.78-1.92j
.3	2.72-1.69j	1.48-2.55j	1.16-2.46j	1.45-1.90j	1.63-1.83j	1.73-1.80j	1.80-1.78j	1.84-1.77j
.32	2.66-1.55j	0.99-3.02j	1.26-2.34j	1.51-1.77j	1.69-1.69j	1.79-1.66j	1.86-1.63j	1.90-1.62j
.34	2.61-1.41j	1.67-2.28j	1.34-2.22j	1.57-1.64j	1.74-1.55j	1.84-1.51j	1.90-1.48j	1.94-1.46j
.36	2.55-1.29j	1.74-2.13j	1.42-2.09j	1.61-1.50j	1.78-1.41j	1.87-1.37j	1.93-1.33j	1.97-1.31j
.38	2.49-1.17j	1.80-1.99j	1.48-1.96j	1.64-1.37j	1.80-1.27j	1.89-1.22j	1.95-1.18j	1.99-1.16j
.4	2.43-1.05j	1.85-1.84j	1.53-1.83j	1.66-1.24j	1.81-1.13j	1.90-1.07j	1.96-1.04j	2.00-1.01j
.42	2.37-0.95j	1.90-1.69j	1.58-1.70j	1.67-1.11j	1.82-0.99j	1.90-0.93j	1.95-0.89j	1.99-0.86j
.44	2.31-0.86j	1.92-1.55j	1.61-1.57j	1.67-0.98j	1.81-0.85j	1.88-0.79j	1.93-0.75j	1.97-0.72j
.46	2.25-0.78j	1.94-1.40j	1.63-1.44j	1.66-0.86j	1.79-0.72j	1.86-0.66j	1.91-0.61j	1.94-0.58j
.48	2.19-0.71j	1.94-1.26j	1.64-1.31j	1.64-0.74j	1.76-0.60j	1.82-0.53j	1.87-0.48j	1.90-0.45j

Table S4. Surface plasmon generation efficiency calculation under different incident wavelengths for different nanoslit

w	500 nm	600 nm	700 nm	800 nm	900 nm	1000 nm
50	0.709	0.389	0.264	0.206	0.169	0.143
70	0.704	0.400	0.281	0.224	0.186	0.159
90	0.670	0.391	0.282	0.231	0.194	0.169
110	0.628	0.372	0.276	0.230	0.197	0.173
130	0.588	0.350	0.265	0.225	0.195	0.174
150	0.542	0.327	0.252	0.218	0.191	0.172
170	0.467	0.304	0.239	0.209	0.186	0.169
190	0.327	0.274	0.226	0.200	0.179	0.164
210	0.068	0.231	0.210	0.190	0.172	0.159

REFERENCES

(1) Bagra, B.; Zhang, W.; Zeng, Z.; Mabe, T.; Wei, J. Plasmon-Enhanced Fluorescence of Carbon Nanodots in Gold Nanoslit Cavities. *Langmuir* **2019,** *35* (27), 8903-8909, DOI: 10.1021/acs.langmuir.9b00448.

(2) Zeng, Z.; Mendis, M. N.; Waldeck, D. H.; Wei, J. A semi-analytical decomposition analysis of surface plasmon generation and the optimal nanoledge plasmonic device. *RSC Adv.* **2016,** *6* (21), 17196-17203, DOI: 10.1039/C6RA01105E.

(3) Lalanne, P.; Hugonin, J. P.; Rodier, J. C. Approximate model for surface-plasmon generation at slit apertures. *J. Opt. Soc. Am. A* **2006,** *23* (7), 1608-1615, DOI: 10.1364/JOSAA.23.001608.

(4) Vernet, R.; Charrier, E.; Grogg, J.; Mach, N. A Quantitative ELISA Protocol for Detection of Specific Human IgG against the SARS-CoV-2 Spike Protein. *Vaccines* **2021,** *9* (7), 770, DOI: 10.3390/vaccines9070770.

(5) Eftekhari, A.; Alipour, M.; Chodari, L.; Maleki Dizaj, S.; Ardalan, M.; Samiei, M.; Sharifi, S.; Zununi Vahed, S.; Huseynova, I.; Khalilov, R.; Ahmadian, E.; Cucchiarini, M. A Comprehensive Review of Detection Methods for SARS-CoV-2. *Microorganisms* **2021,** *9* (2), 232, DOI: 10.3390/microorganisms9020232.

(6) Bassi, M. D.; Araujo Todo Bom, M.; Terribile Budel, M. L.; Maltempi de Souza, E.; Müller dos Santos, M.; Roman, L. S. Optical Biosensor for the Detection of Infectious Diseases Using the Copolymer F8T2 with Application to COVID-19. *Sensors* **2022,** *22* (15), 5673, DOI: 10.3390/s22155673.

(7) Dai, Z.; Xu, X.; Wang, Y.; Li, M.; Zhou, K.; Zhang, L.; Tan, Y. Surface plasmon resonance biosensor with laser heterodyne feedback for highly-sensitive and rapid detection of COVID-19 spike antigen. *Biosens. Bioelectron.* **2022,** *206*, 114163, DOI: 10.1016/j.bios.2022.114163.

(8) Broughton, J. P.; Deng, X.; Yu, G.; Fasching, C. L.; Servellita, V.; Singh, J.; Miao, X.; Streithorst, J. A.; Granados, A.; Sotomayor-Gonzalez, A.; Zorn, K.; Gopez, A.; Hsu, E.; Gu, W.; Miller, S.; Pan, C.-Y.; Guevara, H.; Wadford, D. A.; Chen, J. S.; Chiu, C. Y. CRISPR–Cas12-based detection of SARS-CoV-2. *Nat. Biotechnol.* **2020,** *38* (7), 870-874, DOI: 10.1038/s41587-020-0513-4.

(9) Zhu, X.; Wang, X.; Han, L.; Chen, T.; Wang, L.; Li, H.; Li, S.; He, L.; Fu, X.; Chen, S.; Xing, M.; Chen, H.; Wang, Y. Multiplex reverse transcription loop-mediated isothermal amplification combined with nanoparticle-based lateral flow biosensor for the diagnosis of COVID-19. *Biosens. Bioelectron.* **2020,** *166*, 112437, DOI: 10.1016/j.bios.2020.112437.

(10) Moitra, P.; Alafeef, M.; Dighe, K.; Frieman, M. B.; Pan, D. Selective Naked-Eye Detection of SARS-CoV-2 Mediated by N Gene Targeted Antisense Oligonucleotide Capped Plasmonic Nanoparticles. *ACS Nano* **2020,** *14* (6), 7617-7627, DOI: 10.1021/acsnano.0c03822.

(11) Seo, G.; Lee, G.; Kim, M. J.; Baek, S.-H.; Choi, M.; Ku, K. B.; Lee, C.-S.; Jun, S.; Park, D.; Kim, H. G.; Kim, S.-J.; Lee, J.-O.; Kim, B. T.; Park, E. C.; Kim, S. I. Rapid Detection of COVID-19 Causative Virus (SARS-CoV-2) in Human Nasopharyngeal Swab Specimens Using Field-Effect Transistor-Based Biosensor. *ACS Nano* **2020,** *14* (4), 5135-5142, DOI: 10.1021/acsnano.0c02823.

(12) Chaibun, T.; Puenpa, J.; Ngamdee, T.; Boonapatcharoen, N.; Athamanolap, P.; O'Mullane, A. P.; Vongpunsawad, S.; Poovorawan, Y.; Lee, S. Y.; Lertanantawong, B. Rapid electrochemical detection of coronavirus SARS-CoV-2. *Nat. Commun.* **2021,** *12* (1), 802, DOI: 10.1038/s41467-021-21121-7.

(13) Najjar, D.; Rainbow, J.; Sharma Timilsina, S.; Jolly, P.; de Puig, H.; Yafia, M.; Durr, N.; Sallum, H.; Alter, G.; Li, J. Z.; Yu, X. G.; Walt, D. R.; Paradiso, J. A.; Estrela, P.; Collins, J. J.; Ingber, D. E. A lab-on-a-chip for the concurrent electrochemical detection of SARS-CoV-2 RNA and anti-SARS-CoV-2 antibodies in saliva and plasma. *Nature Biomedical Engineering* **2022,** *6* (8), 968-978, DOI: 10.1038/s41551-022-00919-w.
(14) Huang, L.; Ding, L.; Zhou, J.; Chen, S.; Chen, F.; Zhao, C.; Xu, J.; Hu, W.; Ji, J.; Xu, H.; Liu, G. L. One-step rapid quantification of SARS-CoV-2 virus particles via low-cost nanoplasmonic sensors in generic microplate reader and point-of-care device. *Biosens. Bioelectron.* **2021,** *171*, 112685, DOI: 10.1016/j.bios.2020.112685.
(15) Qiu, G.; Gai, Z.; Tao, Y.; Schmitt, J.; Kullak-Ublick, G. A.; Wang, J. Dual-Functional Plasmonic Photothermal Biosensors for Highly Accurate Severe Acute Respiratory Syndrome Coronavirus 2 Detection. *ACS Nano* **2020,** *14* (5), 5268-5277, DOI: 10.1021/acsnano.0c02439.

APPENDIX B: A PLASMONIC NANOLEDGE ARRAY FOR SENSITIVE DETECTION OF CARDIOVASCULAR DISEASE BIOMARKER

Figure S1. Measured transmittance spectra for the tSPR probe in various solvents before hydrophilization (A-B) and after hydrophilization (C-D). Note that Figures B) and C) represents the linear fit of the tSPR peak wavelengths with the index of refraction of the solvents in contact with the gold surface

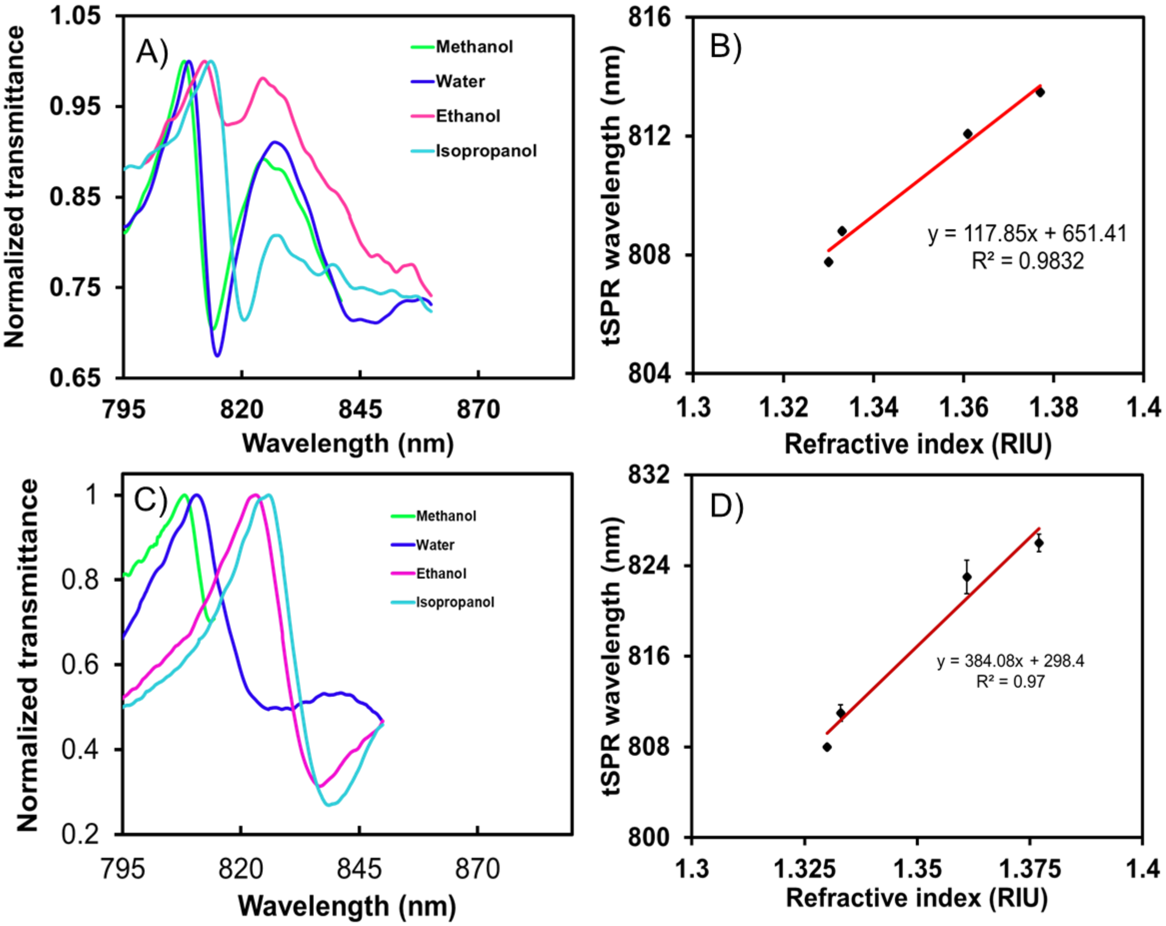

Figure S2. tSPR upon TnI incubation with aptasensor at different binding times. This was obtained by transferring 50 µL of 0.156 ng/mL cTnI sample in PBS on to a clean aptamer-modified sensor chip

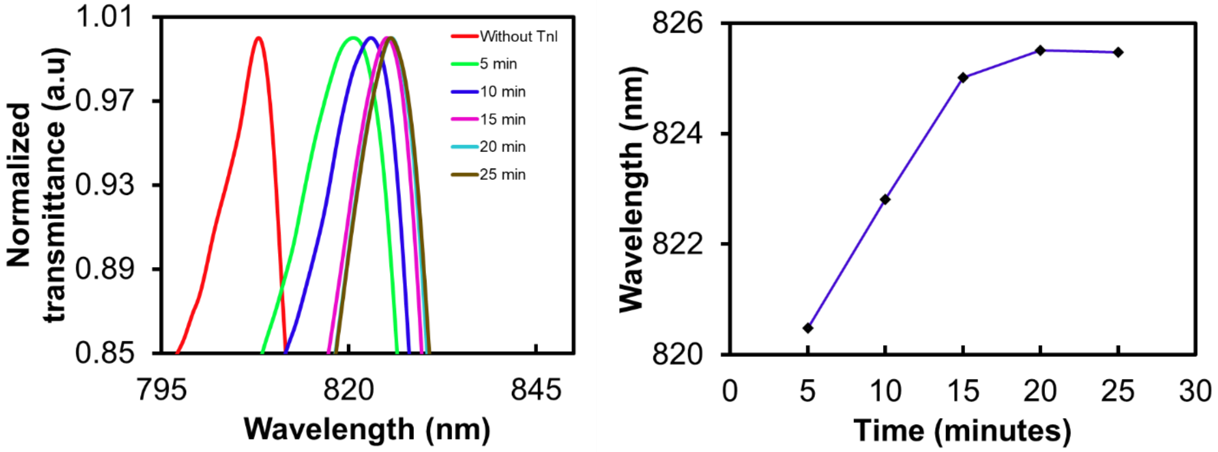

Figure S3: Dependence of adlayer film thickness on (A) change in wavelength position (B) cTnI concentration

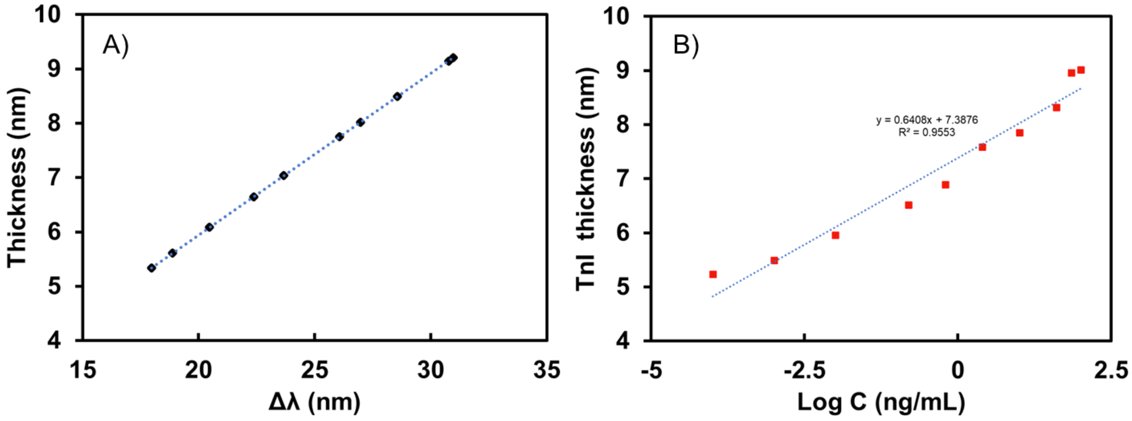

Figure S4. Graph of tSPR versus concentration (in PBS) showing experimental data points (black dots) fitted with the equation,

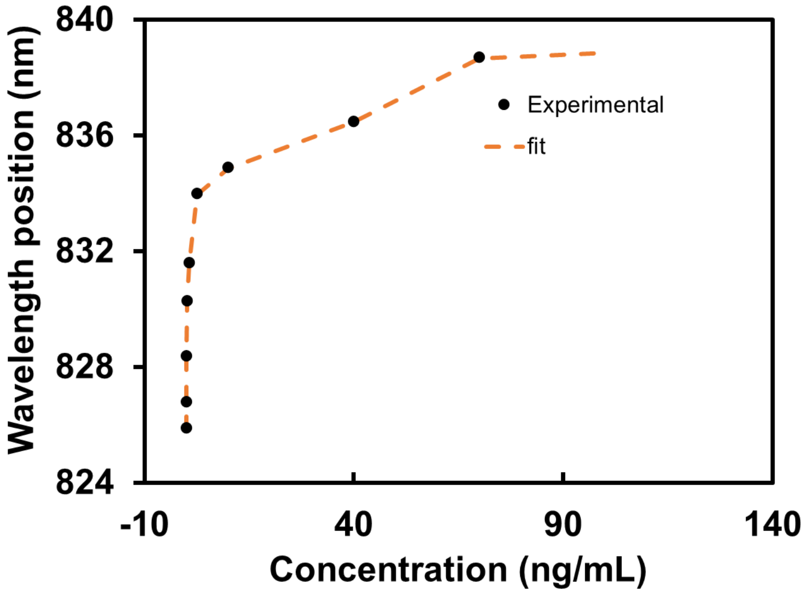

$$d = (l_d/2)\{\frac{\Delta\lambda}{[(m(n_{SAM} - n_{air})]}\}$$

The best fit was obtained using l_d=122.9 nm.

Table S1. **Addlayer thickness as a function of concentration and wavelength peak shift**

	Cys	Glu	Apt	TnI concentration (ng/mL)									
				0 .0001	0.001	0.01	0.156	0.625	2.5	10.0	40.0	70.0	100.0
Δλ (nm)	.58±0.64	.37±0.23	.69±0.08	7.97±0.50	8.87±0.03	0.47±0.10	2.37±0.38	3.67±0.05	6.07±0.11	6.97±0.02	8.57±0.63	0.77±0.03	0.97±0.04
d(nm)	.77	.40	.39	.34	.61	.09	.65	.04	.75	.02	.49	.15	.02
d(nm) (ld=134nm)	.75	.39	.22	.96	.23	.71	.28	.66	.38	.64	.12	.77	.78

Estimation of Aptamer surface coverage, θ from measured SPR response

Coverage, θ (Molecules/cm^2)= layer thickness,d (cm) X N (molecules/cm^3)

Where N=bulk number density of the aptamer given by

$$\mathrm{N} = \frac{\mathrm{p(g/cm3)}}{Molecular\ weight}\ x\ Avogadros\ number$$

$=8.341\text{x}10^{19}$ molecules/cm^3

Where p is the density of pure adsorbate (aptamer)=1.7 g/cm^3 [1], Aptamer molecular weight=12,274 g/mol, Avogadros number=$6.022\text{x}10^{23}$.

Hence, $\theta=2.644\text{x}10^{20}$ molecules/cm^2

Therefore, the chip's sensing area of 50 μm x 75 μm (3.75×10^{-5} cm^2) contain about 9.915×10^{15} molecules. Note that the refractive index of an aptamer or ssDNA is reported to be around 1.46 [2- 3].

REFERENCES

1. Lee C-Y, Gamble LJ, Grainger DW, Castner DG. Mixed DNA/oligo (ethylene glycol) functionalized gold surfaces improve DNA hybridization in complex media. *Biointerphases*. 2006;1(2):82-92. doi:10.1116/1.2219110
2. Morris et al. 2012. NIH Public Access. *Gerontology*. 2015;61(6):515-525. doi:10.1016/j.bios.2009.06.033.Quantification
3. Elhadj S, Singh G, Saraf RF. Optical properties of an immobilized DNA monolayer from 255 to 700 nm. *Langmuir*. 2004;20(13):5539-5543. doi:10.1021/la049653+